Molecular Friction and Dynamics in Aqueous Solutions

im Fachbereich Physik der Freien Universität Berlin eingereichte Dissertation

zur Erlangung des akademischen Grades eines Doktors der Naturwissenschaften (Dr. rer. nat.)

vorgelegt von
Jan Oliver Daldrop

Berlin, 2018

Erster Gutachter:	Prof. Dr. Roland R. Netz Freie Universität Berlin
Zweiter Gutachter:	Prof. Dr. Holger Stark Technische Universität Berlin
Tag der Disputation:	22. Juni 2018

Contents

If, in some cataclysm, all of scientific knowledge were to be destroyed, and only one sentence passed on to the next generation of creatures, what statement would contain the most information in the fewest words? I believe it is the atomic hypothesis that all things are made of atoms—little particles that move around in perpetual motion, attracting each other when they are a little distance apart, but repelling upon being squeezed into one another. In that one sentence, you will see, there is an enormous amount of information about the world, if just a little imagination and thinking are applied.

Richard P. Feynman

Chapter 1

Introduction

Almost all biochemically relevant processes occur in water. Over the last decades, the picture has emerged that the solvent itself plays a crucial and active role for key processes in living organisms [1]. Biomolecules like proteins are surrounded by hydration shells, spherical layers of temporary bound water molecules, which are fundamental to protein dynamics and function [2, 3]. Particularly, the hydration shell dynamics has a strong impact on a solvated molecule and vice versa [4, 5].

The most important dynamic effect of the solvent is the generation of molecular friction. It determines the fundamental timescale for all processes in solvent, ranging from chemical reactions [6] via molecular diffusion [7] to macromolecular conformational changes [8, 9] and protein folding [10, 11]. In the following, the importance of molecular friction is illustrated by three examples of such processes.

Molecular diffusion refers to the thermal motion of molecules at finite temperature. It plays an essential role for the transport of molecules in living cells, even metabolic pathways rely partly on molecular diffusion [12]. Despite the fact that the long-time behavior of diffusion in water can be described by relatively simple equations, the short-time processes, which include the solvent reorganization and thus the breaking and formation of hydrogen bonds [13–15], are very complex and subject to current research efforts.

A surprisingly fast molecular transport process is the diffusion of excess protons in water; a hydrated excess proton is transported as a H_3O^+ defect, in such a way that the excess proton continuously changes [16, 17]. In addition to the great importance of protons for cell function, the capability of water to efficiently conduct protons is used in various technological applications such as fuel cells and other electrochemical devices [18–20].

A more complex example of a crucial biophysical reaction is protein folding, where a protein changes its conformation from an unordered state to a particular, so-called folded state [21], which typically determines its function in biological systems. How long will such a process take? Clearly, the rate-limiting step of this reaction is given by the search of the energetically favored, folded state among an enormous amount of

other possible conformations. However, the folding time cannot be estimated based on these considerations alone, because the speed with which these configurations are sampled is a priori unknown. Molecular friction is exactly what determines this missing prefactor. The most straight-forward assumption is that the molecular friction is given by the diffusion constant, which is proportional to the solvent viscosity. Indeed, the fact that this timescale will dominate for sufficiently large polymers is known as the Kuhn theorem [22–24]. However, it was found experimentally that the folding times of many proteins are not proportional to the solvent viscosity, but they show a significant independent contribution commonly referred to as internal friction [8, 10, 25–29]. The molecular origin of this internal friction is not fully understood.

Clearly, these are just some among many examples, which exemplify the importance—but also the complexity—of molecular friction and dynamics.

With modern experimental techniques, a direct investigation of dynamic molecular processes is possible. Spectroscopic approaches like nuclear magnetic resonance spectroscopy [30, 31] or time-resolved infrared spectroscopy [32, 33] allow to probe timescales down to sub-picosecond resolution. Atomic force microscopy [34] and single-molecule Förster resonance energy transfer experiments [35, 36] can be used to study the dynamics of single molecules. Together with the enormous amount of structural information revealed by X-ray crystallography [37] and of course innumerable other methods, the extent of information available on the molecular scale is remarkable. However, experimental information is always incomplete, because it is limited to a few setup-specific observables. Only by the combination of experiments and theoretical models, it has been possible to form our current detailed understanding of the molecular dynamics relevant for biological life.

For many biophysical applications, a surprisingly good approximation [38] for the molecular friction coefficient γ of a particle with effective radius R is given by Stokes' law $\gamma = 6\pi\eta R$, which was derived by Stokes already in 1851 from the viscous laminar flow around a sphere in a liquid with viscosity η [39]. Later in 1905, Einstein recognized the connection between molecular friction and Brownian motion at a temperature T in one of his seminal publications, and derived the Stokes-Einstein relation $D = k_\mathrm{B}T/6\pi\eta R$ [40], where the diffusion constant D is defined by the mean-square displacement $D = \left\langle (\boldsymbol{x}(t) - \boldsymbol{x}(0))^2 \right\rangle / 6t$ of a particle trajectory $\boldsymbol{x}(t)$ for sufficiently large t. This fascinating connection between friction and thermal fluctuations was later generalized as the famous fluctuation-dissipation theorem [41, 42], which relates the thermal fluctuations of a system observable to its response to perturbations. For the case of linear response around equilibrium, exact analytical expressions for transport coefficients in terms of time correlation functions were derived by Green [43] and Kubo [44].

Whereas the long-time translational motion of a single molecule can be well described by the above mentioned relations, most biomolecular reactions are tremendously more complex, as for example is the case for protein folding. Crossing over a barrier in an effective one-dimensional free energy landscape is a prominent and very successful model

for such processes [45–53]. These one-dimensional models can be either described by so-called Langevin equations [54–56], which are stochastic differential equations for individual trajectories, or by the equivalent partial differential equations for the probability distribution, so-called Fokker-Planck equations [55–58].

Langevin introduced his stochastic differential equation for the diffusive dynamics of a particle with mass m in 1908 [54]. It reads

$$m\ddot{x}(t) = -\gamma\dot{x}(t) + \xi(t), \tag{1.1}$$

where the stochastic noise term $\xi(t)$ is assumed to be Gaussian distributed, and the fluctuation-dissipation theorem implies for its ensemble average

$$\left\langle \xi(t)\xi(t')\right\rangle = 2k_{\mathrm{B}}T\gamma\,\delta(t-t'). \tag{1.2}$$

The Langevin equation is thus an equation that describes many individual, random trajectories. It is well suited for computer simulations, since one can easily generate an ensemble of trajectories numerically. Numerous generalizations and applications to a wide range of systems have been derived [55, 59].

The Langevin equation (1.1) assumes the friction contribution to be instantaneous, which is mirrored by the δ-correlated noise and the instantaneous friction force $-\gamma\dot{x}(t)$. For many systems, this is a very good approximation. However, on the molecular scale, the interactions between molecules will take a finite amount of time. In particular, for the description of the short-time dynamics of small water-solvated molecules, this approximation breaks down.

A more rigorous approach to model a larger class of systems is given by the so-called generalized Langevin equation (GLE) derived by Mori in 1965 [60]. He used an exact linear projection technique based on the Liouville operator formalism to show that the phase space dynamics of a Hamiltonian system can always be projected onto a one-dimensional reaction coordinate, leading to the stochastic integro-differential equation

$$m\ddot{x}(t) = -\int_0^t dt'\,\Gamma(t-t')\dot{x}(t') + F_R(t), \tag{1.3}$$

with the noise correlation

$$\langle F_R(t)F_R(0)\rangle = k_{\mathrm{B}}T\Gamma(t). \tag{1.4}$$

The so-called memory kernel $\Gamma(t)$ describes the time correlation of the dissipative and random forces. In his work, Mori gave an exact analytical expression for this function in the Liouville operator formalism [56, 60, 61].

The derivation of the GLE was a remarkable achievement. On the one hand, it establishes a direct connection between Hamiltonian dynamics and stochastic differential equations: Mori's projection technique proves that the memory kernel exactly reflects the degrees of freedom orthogonal to reaction coordinate x, which allows a clear interpretation. In particular, the Langevin equation (1.1) can be obtained by setting $\Gamma(t) = 2\gamma\delta(t)$, and its applicability to molecular systems can thus be well understood

based on the GLE. On the other hand, the GLE has proven to be a very successful tool to model a variety of phenomena [9, 61–72], especially on the molecular scale, where—as mentioned—the Langevin equation does not necessarily hold. One important reason for this success is that for the parametrization of a GLE from experimental or simulation data, no assumptions on a separation of timescales have to be made.

However, these striking advantages come with a price: the memory function $\Gamma(t)$ can in principle be very complicated, and it is difficult to determine for most systems. Several methods for the determination of $\Gamma(t)$ have been proposed in the literature [6, 9, 61, 70, 72–76], but none of them is universally applicable [9, 61].

In addition to these difficulties in parametrizing GLEs and similar stochastic models, a direct determination of the model parameters from experiments is usually not possible for molecular systems, because the required resolution in time *and* space cannot be achieved, despite the astonishing experimental advancement in the recent years.

A very useful and quite universal approach to understand molecular mechanisms are computer simulations. Since their invention in the 1950s [77, 78], the so-called molecular dynamics (MD) simulations, which denote numerical N-body simulations of molecules or atoms, have gained enormous popularity, with applications ranging from proton transfer in water with quantum precision [16, 17, 79] to millisecond simulations of protein folding using custom application-specific integrated circuits [80–83].

In MD simulations, the movements of atoms or molecules are numerically calculated from their interaction potentials. Even for small molecular systems, an exact solution of the dynamics dictated by the Schrödinger equation is usually by far not possible due to the prohibitive computational power such a calculation would require. Instead, various levels of approximation have been introduced.

In the most popular, classical MD simulations, the interactions between atoms are modeled by effective forces, determined and improved over decades to reproduce experimental observables or quantum mechanical calculations as exactly as possible [84]. Due to the accessible timescales reaching up to milliseconds, this technique plays nowadays a central role for our understanding of molecular biophysical processes like protein folding [85–90], ligand binding [90–93] and transport through membrane proteins [90, 94–97]. Even the simulation of an entire tobacco mosaic virus is possible [98].

In so-called ab initio MD simulations, the forces between the nuclei of a system are calculated from the electron density, which is computed for a given nuclei configuration [99–101]. Depending on the simulation method, various approximations are used also for these techniques. Because of the enhanced computational cost, ab initio simulations are limited to smaller systems and shorter timescales, but therefore allow the *in silico* investigation of processes that are not accessible using classical forcefields, like e.g. metallo-organic reactions [102] or the self-repair mechanism of DNA [103, 104]. In particular, ab initio techniques are suitable for the calculation of molecular vibration spectra [101, 105–107], and they have played for example a key role for the assignment of infrared spectral features to protonated water clusters in the transmembrane protein bacteriorhodopsin [108–110], a light-driven proton pump [111–115].

In the present thesis, we combine the predictive power of stochastic and other analytical models with the accuracy of modern simulation techniques. Analytic models are suited to extract key features and to derive general principles from complex all-atom trajectories, and therefore they often constitute the link between theory and experiment. Indeed, this approach will be shown to constitute significant improvement of our view on dynamic molecular processes in water on several timescales and in different friction regimes: We demonstrate the previously unknown dichroism of the infrared continuum absorption caused by the fast proton transfer in non-spherical water clusters. We show for the first time that a confining potential modifies the friction constant of small molecular solutes in water, and we characterize the mass dependence of molecular aqueous friction. We settle a long-lasting question by demonstrating that the dynamics of the torsion angle of a water-solvated butane molecule is dominated by internal friction. Furthermore, we reveal the universal property of barrier-crossing (transition) paths that their velocity distributions deviate from equilibrium.

We start in Chapter 2 with the computation of infrared spectra for protonated and unprotonated water clusters with different geometries from ab initio molecular dynamics trajectories. For all protonated systems, we find pronounced continuum bands, which extend over a broad frequency range. They are shown to exhibit significant polarization anisotropy for chains and discs with increased absorption along the direction of maximal extension. The molecular origin of the continuum band is elucidated by a local spectral analysis. These findings can be used directly to interpret experimental, polarization-resolved infrared spectra of bacteriorhodopsin recorded by Mattia Saita under supervision of Prof. Dr. Joachim Heberle at the Freie Universität Berlin: we show that the protonated water cluster responsible for the continuum band of bacteriorhodopsin is oriented perpendicularly to the proton pumping direction.

In Chapter 3, we investigate basic features of molecular diffusion in liquids based on simulations of externally confined, water-solvated methane molecules. We extract the friction constant and the memory kernel by a newly developed method in the framework of a generalized Langevin model. A new effect going beyond the assumptions of the very established Stokes' law is discovered: if a molecule is confined by an external potential, its friction increases and the water dynamics in the surrounding hydration shell slows down. These findings are relevant for the interpretation of spectroscopy experiments, and our scaling analysis suggests that similar effects play a role for macromolecular solutes in sufficiently viscous solutions.

Similar analysis methods are applied in Chapter 4 to the (previously known) kinetic isotope effect that different isotopes of small solutes have a slightly mass dependent diffusion constant in water. The mass range investigated spans over four orders of magnitude, and it includes the massless and the infinite mass limits to understand the scaling behavior of this effect. The combination of the results from Chapters 3 and 4 hints at the general principle that a reduced dynamic response of a solute to the solvent increases the friction constant and slows down the hydration shell dynamics.

As a next step, we analyze the more complex isomerization dynamics of water-solvated butane in Chapter 5. A new method for the parametrization of a generalized Langevin equation in the presence of a non-linear potential is developed. We compare the dynamics of a partly frozen butane molecule with no internal degrees of freedom to a free molecule, and vary the water viscosity by two orders of magnitude. This systematic approach settles a long-lasting question about the origin of internal friction: the insensitivity of the dihedral angle isomerization rate to the solvent viscosity, which was identified earlier as an important source of internal friction in large polymers [116–124], is itself due to internal friction, in contrast to speculations from the literature. This result is not only relevant for butane, but also for polymer dynamics and protein folding.

Finally, in Chapter 6, we study intrinsic properties of so-called transition paths, which denote paths that reach a target without revisiting the initial position. Transition paths are a relevant concept in the context of barrier crossing. We show that the ensemble properties of these paths deviate from equilibrium: the velocity distribution, which we describe by an effective temperature, is heated up. By a comprehensive analysis extending over five orders of magnitude, we show how this effect and other properties of transition paths depend on the ratio between mass and friction.

Chapter 2

Orientation of Non-Spherical Protonated Water Clusters Revealed by Infrared Absorption Dichroism

Bibliographic information: Parts of this chapter and of Appendix A have previously been published. Reprinted with permission from Ref. [i]. License: CC BY 4.0.

Water is an excellent conductor for protons since the Grotthuss mechanism allows for transport of protons via the fast motion of a H_3O^+ defect [16, 17]. Proton transfer events are key for many essential biological functions, consequently, one finds protein-bound water molecules and internal water wires in proton-conducting transmembrane proteins such as cytochrome c oxidase, photosystem II, bacteriorhodospin and channelrhodopsin [112, 125–127].

Because a proton easily moves from one water molecule to a neighboring one, which is a consequence of low barriers in the proton energy landscape [128–131], the infrared (IR) absorption spectrum of an excess proton in water is not characterized by sharp bands, but rather by very broad, so-called continuum bands. The first IR continuum band was detected in concentrated acid solutions [132] and later seen in a host of different bulk systems [128].

A well studied transmembrane protein where protein-bound water molecules play a crucial role is the light-driven proton pump bacteriorhodopsin (bR) [111–115]. For bR, light-induced broad IR absorption bands have been observed to rise and decay during the photocycle [110, 133–135]. The interpretation of these broad bands is subtle due to several complications: i) Three water clusters exist in bR, so it is a priori not clear which water cluster gives rise to which spectral feature [110]. ii) The translocation of a proton from the cytoplasmic to the extra-cellular side involves a number of transient states. iii) More than one excess proton presumably is present at a time. iv) In the wavenumber range $(2500 - 3000)\,\mathrm{cm}^{-1}$ broad bands have been assigned to strongly hydrogen-bonded

water molecules that do not contain an excess proton [136]. v) The energy dissipated from the retinal excitation might be absorbed by bulk water molecules, also generating transient broad bands [134].

The continuum band observed in the $(1800 - 2200)\,\mathrm{cm}^{-1}$ range, devoid of any other spectral contributions, has been interpreted in terms of protons that are delocalized over a hydrogen-bonded network of amino acid side chains and water molecules. Yet, the precise molecular origin of this continuum band is still under debate. One plausible scenario involves a group of water molecules close to the extracellular protein surface where the proton is released [108, 109]. Therefore, we will assume from here on that the continuum band is generated by this protonated cluster of water molecules. An alternative scenario involves a proton that is shared between glutamate residues [137], see Ref. [110] for a recent overview.

In this chapter, we compute the infrared spectra for protonated and unprotonated water clusters from ab inito molecular dynamics (AIMD) trajectories on the BLYP/TZV2P level using previously established techniques [138]. We compare the spectra for water clusters that are linear, and essentially consist of a single water chain, with two-dimensional water discs and three-dimensional water droplets. We demonstrate that the continuum band in non-spherical protonated water clusters is anisotropic and that such an anisotropy is experimentally detectable in proton-conducting transmembrane proteins, which allows to draw conclusions on the shape and orientation of the protonated water cluster within the protein. In the experimental IR spectra recorded by Mattia Saita under supervision of Prof. Dr. Joachim Heberle at the Freie Universität Berlin, we resolve the continuum band of bacteriorhodopsin aligned in oriented purple membranes. We demonstrate its linear dichroism with a preferred orientation in the plane orthogonal to the membrane normal. This result is consistent with a protonated water cluster extended perpendicularly to the direction of proton pumping. Based on our ab initio simulations, we perform a local spectral analysis of the protonated water chain, which shows that the continuum band arises from polarization fluctuations of the excess proton, which is predominantly observed in a Zundel complex as it moves axially along the chain. The electronic polarizability of the chain gives rise to a moderate, but long-ranged amplification of the polarization fluctuations.

2.1. Results

2.1.1. Anisotropic Spectra from Ab Initio Simulations

In the ab initio simulations, we consider three different water cluster geometries, namely chains, discs and droplets, consisting of 15, 15 and 26 water molecules, respectively. The different water cluster geometries are stabilized by harmonic confining potentials with strengths such as to produce realistic water densities (see Methods). For the chain geometry we compare a narrow and a wide version, configurational snapshots are shown in Fig. 2.1. Similar simulations have been previously performed for water chains and fast proton transport has been observed and characterized [140, 141]. The computed

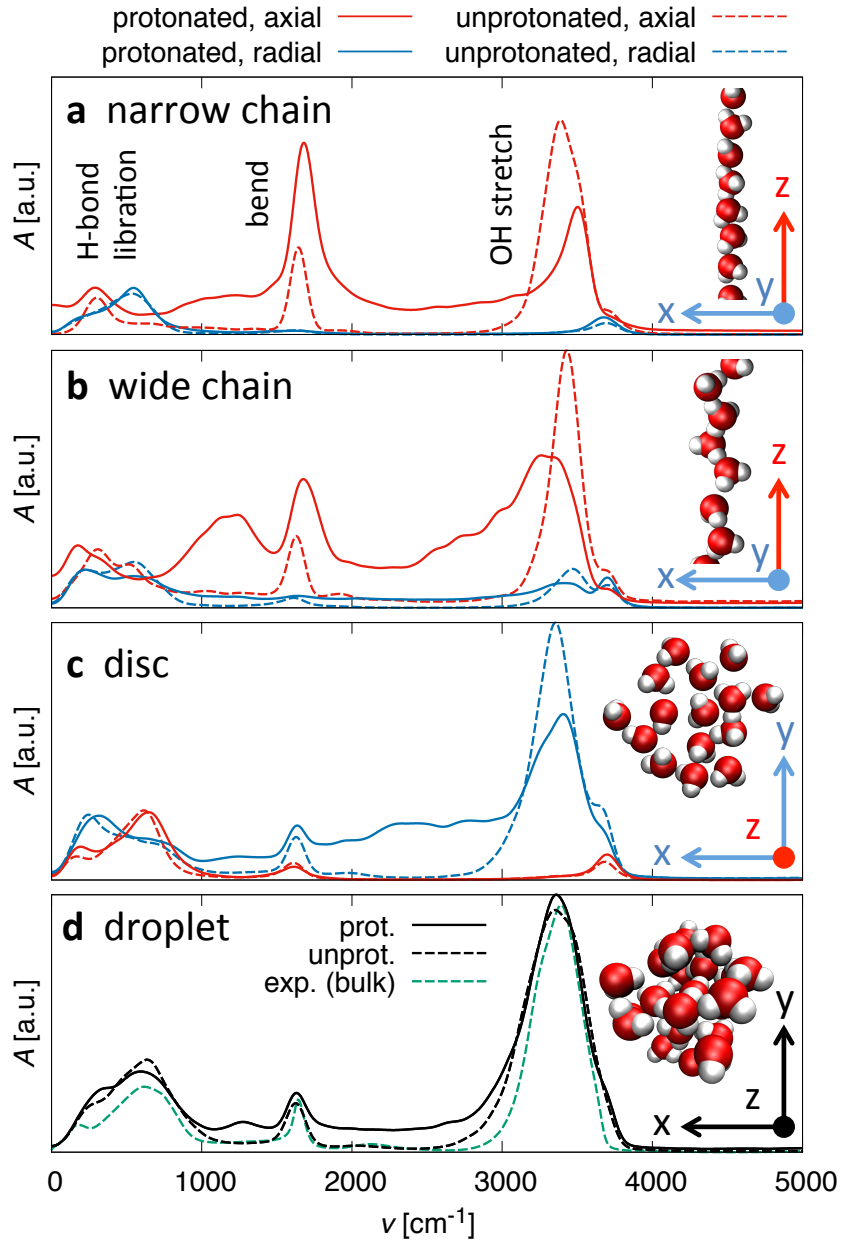

Figure 2.1.: **Simulated spectra and snapshots.** Anisotropic infrared spectra computed from ab initio trajectories for (a) a narrow chain, (b) a wide chain, (c) a disc and (d) a droplet of water with (solid lines) and without (dashed lines) an excess proton. Red lines show the spectrum for an E field in the axial z direction, blue lines the spectrum for an E field in the radial xy directions, radial components are averaged. For the droplet all directions are averaged. In (d), the experimental bulk water absorption spectrum at $T = 25°C$ [139] is included (green dashed line). In each panel, the intensities of the computed spectra are drawn to scale.

infrared spectra are shown in Fig. 2.1, where we compare spectra in the presence of an excess proton (solid lines) to results without an excess proton (dashed lines). For chains and discs we distinguish between absorption with the E field parallel to z, which is the rotational symmetry axis (red lines), and absorption with the E field in the xy-plane (blue lines). Comparison between the absorption along equivalent directions (i.e. x and y directions for chains and discs) allows us to estimate statistical errors (see Figs. A.1 and A.2 in Appendix A).

In all geometries, we resolve well separated bands that correspond to the OH-stretch vibration around wavenumbers $\nu \approx 3400\,\mathrm{cm}^{-1}$, the H_2O bending mode around $\nu \approx 1645\,\mathrm{cm}^{-1}$, and bands at much lower wavenumbers that are due to hydrogen bond vibrations and librations [142]. We compare the simulated water droplet spectra in Fig. 2.1(d) (black lines) with the experimental absorption spectrum of liquid water [139] (green dashed line). Although our ab initio simulations neglect quantum nuclei motion, which in principle can be corrected for heuristically [143], the numerical spectrum for the unprotonated water droplet (black dashed line) reproduces the experimental band positions and shapes quite nicely.

For all geometries, the presence of an excess proton gives rise to a broad and pronounced continuum band extending over almost the entire wavenumber range (protonated minus unprotonated difference spectra are shown in Fig. A.3 in Appendix A). Most importantly, the continuum band is almost completely polarized along the direction of maximal cluster extension, i.e. along the z-axis for chains in Figs. 2.1(a) and (b) and along the xy-plane for the disc in Fig. 2.1(c). This resonates well with the intuitive notion that the continuum band is caused by the motion of a delocalized proton, which due to the confinement occurs along the z-axis for a water chain and in the xy-plane for the disc. Although the anisotropy of the continuum band is more pronounced for the narrow chain in Fig. 2.1(a), it is still significant for the wide chain in Fig. 2.1(b), which demonstrates that the continuum band anisotropy is robust with respect to the water chain structure.

A closer look at the spectra reveals that the high wavenumber shoulder of the OH stretch vibration peak, which is ascribed to dangling OH bonds [144, 145], comes from polarization fluctuations that are perpendicular to the cluster extension, both in the presence and absence of an excess proton. This nicely confirms the intuitive expectation, since dangling OH bonds are predominantly oriented radially for chains and axially for discs. For the bending mode the opposite anisotropy is observed, demonstrating that the water dipole moment (and thus the predominant absorption in the bending mode) points along the direction of maximal extension for the non-spherical clusters. This shows that polarization resolved IR spectroscopy of non-spherical aligned water clusters allows to obtain detailed information on the water cluster structure and orientation.

We conclude that an excess proton gives rise to a pronounced continuum band, regardless of the water cluster geometry. This in turn means that the mere presence of a continuum band in an IR spectrum conveys little information on the proton-solvating water cluster geometry. However, and as we will show now by comparison with the experimental results for bR, the pronounced polarization anisotropy of the continuum

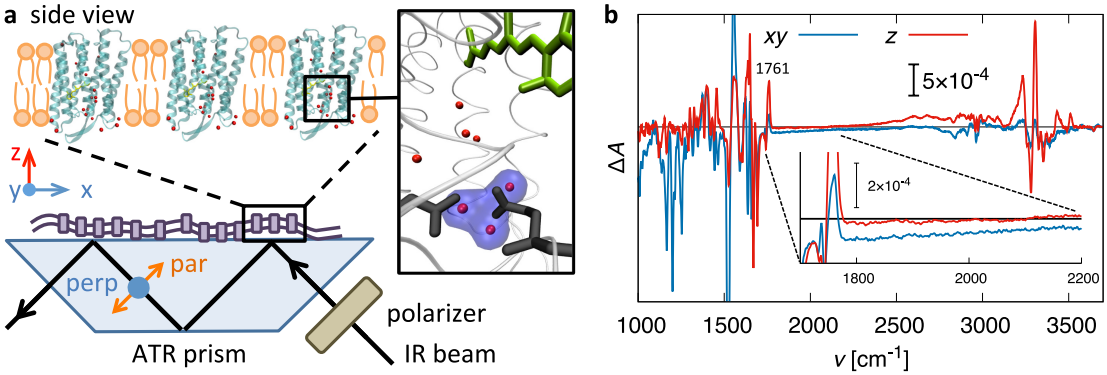

Figure 2.2.: **Experimental polarization-resolved spectra.** (a) In the experimental setup, the purple membranes are oriented in the xy-plane and the proton pumping direction is along z. The black arrow indicates the direction of the probing IR light, which is polarized parallel or perpendicular with respect to the plane of incidence. The inset shows a zoom-in of the crystal structure of bacteriorhodopsin [146], with three water molecules highlighted in blue, which presumably cause the continuum band [109, 110]. (b) Experimental IR light-minus-dark difference spectra calculated along the xy and z directions over the whole measured range between $1000\,\mathrm{cm}^{-1}$ and $3800\,\mathrm{cm}^{-1}$. In the inset, the enlarged difference absorption spectra in the relevant wavenumber range $(1700 - 2200)\,\mathrm{cm}^{-1}$ are shown together with the (positive) band at $1761\,\mathrm{cm}^{-1}$ of the C=O stretching vibration of D85.

band can be used to reveal whether the protonated water cluster is non-spherical and if so what its orientation is.

2.1.2. Polarization-Resolved Experimental Infrared Spectra

Fourier-transform infrared (FTIR) difference spectroscopic experiments on purple membrane films using the attenuated total reflection (ATR) method [147] were performed by Mattia Saita under supervision of Prof. Dr. Joachim Heberle at the Freie Universität Berlin. The purple membranes spontaneously form parallel stacks of membrane sheets with the membrane normal along the z direction upon drying on the ATR silicon surface [148], as schematically shown in Fig. 2.2(a). The sample was kept in a controlled semi-dry state (see Ref. [i] for experimental details), which reduces the amount of bulk water molecules [149] and slows down the bR photocycle [150], but preserves the internal water molecules. As a control, a more hydrated sample was prepared, which resulted in almost indistinguishable IR difference spectra, although of smaller intensity (see Ref. [i]). Light absorption by the chromophore triggers a sequence of transitions that have been well characterized by experimental and theoretical means [151]. According to the generally accepted view, in the dark state, an excess proton resides in a water cluster close to the exit site at the extracellular side of the protein, as schematically

indicated in the inset of Fig. 2.2(a). Continuous illumination leads to the accumulation of the intermediate M state under the experimental conditions (with only minor contributions from the subsequent N state) [152, 153], where the excess proton is not present in the proton release group, but has just been transferred to the extracellular medium. Thus, the light-induced difference spectrum of bR under continuous illumination contains differential information about the proton release group.

IR light with polarization parallel and perpendicular to the plane of incidence [154] was employed, see Fig. 2.2(a) for a schematic illustration of the geometry. The light-minus-dark difference spectrum measured with perpendicularly polarized IR radiation provides the difference spectrum in the xy-plane of bR, denoted as ΔA_{xy}, while parallel IR light gives rise to a linear combination of the difference spectra in the xy-plane and along the z direction (the latter being denoted as ΔA_z) [155]. The difference spectrum ΔA_z is calculated according to a published formalism [154, 156]. Both spectra ΔA_{xy} and ΔA_z are presented in Fig. 2.2(b). The continuum band in the frequency range $(1700 - 2200)\,\mathrm{cm}^{-1}$ is enlarged in the inset. We restrict our analysis to this range, because it is of diagnostic value for the presence of a protonated hydrogen-bonded network of water molecules. In contrast, the dichroism of the broad band above $2500\,\mathrm{cm}^{-1}$ presumably arises from a neutral cluster of strongly hydrogen-bonded water molecules located at the cytoplasmic side of the protein [135]. Note that the sharp band at $1761\,\mathrm{cm}^{-1}$ at the lower end of the continuum band arises from the C=O stretching vibration of the aspartic acid D85, which is the proton acceptor of the retinal Schiff base [157].

The continuum band is clearly evident in the lateral difference spectrum ΔA_{xy} with a near-constant negative intensity, but almost completely absent in the normal difference spectrum ΔA_z (Fig. 2.2(b), inset). As expected, the continuum band in the light-minus-dark spectrum ΔA_{xy} is negative, since the corresponding water cluster is protonated in the dark state and deprotonated in the M intermediate state (which dominates under illumination). The recorded FTIR spectra are thus not consistent with a protonated water wire along the z direction, in which case ΔA_z should be negative, nor with a protonated isotropic water cluster, in which case both ΔA_z and ΔA_{xy} should be negative. Rather, this experimental result suggests a delocalized proton in the dark state of bR that is delocalized in the xy-plane perpendicular to the pumping direction. This delocalization could in principle originate from a water wire perpendicular to the z-axis or from a disc oriented in the xy-plane. We also cannot exclude a contribution from a delocalized proton that moves laterally at the surface of the protein [158] or at the surface of the purple membrane, although amino acid exchange studies of the protein [159] invalidate this hypothesis. It is known that protons exhibit enhanced residence times at the surface of lipid membranes [158, 160, 161], but we expect the surface concentrations of protons in the light and dark state to be rather similar due to the excess of buffer molecules present as well as due to the buffering effect of the protein surface itself. Therefore, we suggest that the contribution of delocalized protons on the membrane surface to the difference spectrum is negligible.

2.1.3. Microscopic Characterization of the Continuum Band

To learn more about the origin of the continuum band in protonated water clusters, we compare in Fig. 2.3 the simulated axial spectrum of a narrow protonated water chain including contributions from vibrations of the nuclei and electron polarization fluctuations (denoted as n+e and already shown in Fig. 2.1(a), red line) with the spectrum obtained from the nuclear motion alone (denoted by n, broken line); for the latter we assign effective charges $q_{\mathrm{H}} = +\mathrm{e}$ and $q_{\mathrm{O}} = -2\,\mathrm{e}$ to protons and oxygens. This choice overestimates the water dipole moment and thus exaggerates the water vibration bands, but gives the excess proton the correct charge (see Appendix A for details). All spectra are plotted to scale and thus can be compared with each other. Fig. 2.3 shows that in the wavenumber range $\nu \approx (2000 - 3000)\,\mathrm{cm}^{-1}$, the amplitude of the continuum band in the full n+e spectrum is doubled compared to the n spectrum, indicating a sizable electronic contribution to the continuum band. We also compute the spectral contribution of the excess proton together with its two neighboring water molecules, which together make up the Zundel complex $\mathrm{O_2H_5^+}$ (see Appendix A for details on the projection formalism [138, 162]). Note that the Zundel complex is the dominant solvation state of the excess proton in water chains [140], in contrast to discs and bulk water, where the Eigen state dominates (see Appendix A for a comparison of Zundel occupation probabilities in the different water cluster geometries). In Fig. 2.3 the contribution of the Zundel complex to the axial spectrum is shown including contributions from nuclear motion and electronic polarization (denoted n+e, violet line) and nuclear motion alone (denoted n, yellow line). Interestingly, the nuclear motion spectrum of the Zundel complex (yellow line) is sufficient to describe the nuclear motion spectrum of the entire chain (dashed black line) in the range between $\nu \approx (2000 - 3000)\,\mathrm{cm}^{-1}$. At the same time, the difference between the Zundel spectrum including only nuclear motion (yellow line) and the Zundel spectrum including also the electronic contribution (violet line) is minimal in this frequency range. This means that the nuclear contribution to the continuum band comes from a very localized region around the excess proton, while the electrons in the Zundel complex contribute little to the spectrum. We conclude that the axial continuum band in protonated water chains is caused by local nuclear polarization fluctuations in the immediate vicinity of the excess proton, which predominantly corresponds to a Zundel complex. The nuclear polarization fluctuations are amplified by the rather long-ranged electronic polarizability which extends further out to next-nearest neighboring water molecules.

2.2. Discussion

We have computed the infrared spectra for protonated and unprotonated water clusters with different geometries from AIMD trajectories, namely water clusters that are linear and essentially consist of a single water chain with two-dimensional water discs and three-dimensional water droplets. The IR spectra of all protonated water clusters, but not the neutral ones, exhibit pronounced and broad continuum bands, irrespective of

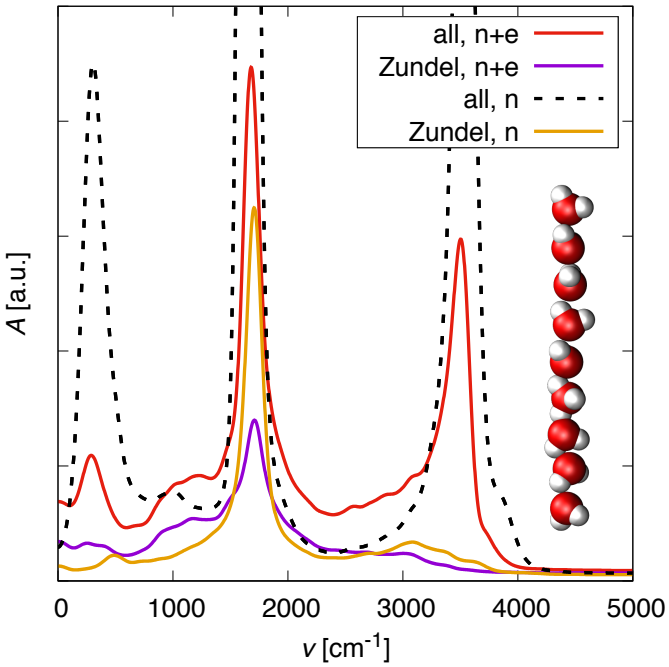

Figure 2.3.: **Spectral decomposition for a protonated chain.** Comparison of the simulated infrared spectrum of the protonated narrow chain in the axial direction including electronic degrees of freedom (n+e, red line) to the spectrum obtained from nuclei only by assigning effective charges $q_{\mathrm{H}} = -q_{\mathrm{O}}/2 = 1\,\mathrm{e}$ (n, broken line), the spectrum of the projected Zundel ensemble including electronic degrees of freedom (violet line) and the spectrum calculated from the Zundel ensemble using nuclei only (yellow line).

the shape. Therefore, the mere existence of a continuum band contains no information about the shape of the protonated water cluster. However, the IR continuum band exhibits strong dichroism for chains and discs, i.e., the absorption is maximal for IR light that is polarized axially for the water chain and in a radial direction for the water disc. For spherical water droplets, the continuum band is isotropic, as expected. This means that the continuum band appears for IR radiation that is polarized along the direction of proton motion.

This anisotropy of the continuum band is not only interesting per se, but also aids in the interpretation of the continuum band of bR: different water clusters that exist in bR and which play a role at different stages of the proton transfer reaction, presumably have different shapes and orientations. Therefore, measurements of the IR absorption dichroism allow to exclude certain proton transfer scenarios. In fact, the experimental polarization-resolved IR absorption difference spectra of oriented bR molecules in native purple membranes show a pronounced continuum band with a polarization perpendicular to the membrane normal, suggesting that the protonated water cluster responsible for the signal is predominantly oriented perpendicularly to the membrane normal. To be more specific, while at the cytoplasmic side of bR, where protons enter, water forms a linear water chain that is parallel to the proton transfer direction, the water cluster close to the extracellular release site was indeed speculated to be more likely oriented perpendicularly to the proton transfer direction, i.e. parallel to the membrane [110].

The continuum band has previously been intensely studied by time-resolved FTIR spectroscopy using unpolarized [113, 133, 134, 153, 159, 163] and to less extend polarized [164] IR radiation. Here, we resolve its polarization dependence under equilibrium continuous illumination conditions, which excludes spectral artifacts by laser-induced heat transfer from the protein to the aqueous solution [134].

Our decomposition of the numerically calculated spectra into the separate contributions stemming from nuclear dynamics (i.e. actual vibrations) and from electronic polarization effects shows that the continuum band is mostly caused by nuclear motion, which are amplified by slaved electronic polarization effects. A further projection onto the immediate vicinity of the excess proton suggests that indeed the continuum band is caused by the moving excess proton, in agreement with previous results [128, 162].

We note that our simulations neglect the coupling to flanking amino acid side chains, which has been demonstrated to be important [137], and instead represent the chemical confinement by a smooth and structureless external potential. More detailed simulations are planned, but we do not expect the basic qualitative features concerning the anisotropy of the continuum band to be dependent on the detailed description of the chemical environment.

The described experimental approach is general and can be used to study the orientation of protonated water clusters also in other membrane proteins, particularly those that involve proton translocation, like e.g. photosystem II [165], photosynthetic reaction center [166, 167], archaerhodopsin-3 [168], and cytochrome c oxidase [169]. Apart from proteins, we expect similar effects also in other systems that contain water clusters, for example in inverted hexagonal lipid phases, where water forms hexagonally ordered par-

allel cylinders, or in lipid lamellar phases, where water forms thin slabs [170]. Such lipid systems are known to orient on surfaces [171], which enables IR dichroism studies with similar techniques as used by us. A different system that contains thin water chains are sub-nanometer diameter carbon nanotubes, that can be embedded and thereby oriented in lipid membranes [172].

2.3. Methods

2.3.1. Ab Initio Simulations

The AIMD simulations are carried out with the CP2K 2.5 software package [173], using a TZV2P basis set [174] and the BLYP exchange correlation functional [175]. Box sizes are determined from the extension of typical snapshots of the systems so that each atom is at at least 0.8 nm away from the nearest boundary. For all systems we use non-periodic boundary conditions based on the Martyna-Tuckerman method [176]. For the production runs, we first generate 15 ps trajectories using a massive Nosé-Hoover chain thermostat [177, 178] (chain length of 3) to generate an equilibrium ensemble at $T = 300\,\mathrm{K}$. From multiple snapshots of this trajectory we start NVE runs of about 5 ps each to obtain a total NVE simulation time of 130 ps per system.

2.3.2. Calculation of Infrared Spectra

For the calculation of the molecular dipole moments, localized Wannier centers for all electron pairs are computed and saved in each simulation step. Infrared spectra are computed from the trajectories via

$$A(\omega) \propto \int \langle \dot{\boldsymbol{\mu}}(0)\dot{\boldsymbol{\mu}}(t)\rangle\, e^{-i\omega t} dt, \tag{2.1}$$

where $\boldsymbol{\mu}$ denotes the dipole moment computed from the nuclei and Wannier center positions. For visualization, the spectra are smoothed by a Gaussian kernel with a width of $\sigma_\nu = 50\,\mathrm{cm}^{-1}$.

2.3.3. Simulation System Setup

The oxygen atoms of the water chains are radially constrained by a harmonic potential $U_{xy}^{\mathrm{chain}}(x,y) = K_{xy}(x^2+y^2)/2$, with $K_{xy} = 2000\,\mathrm{kJ\,mol^{-1}\,nm^{-2}}$ for the narrow chain and $K_{xy} = 20\,\mathrm{kJ\,mol^{-1}\,nm^{-2}}$ for the wide chain. Note that the oriented water molecules in the chain weakly localize the excess proton in the chain center [179].

The disc system is axially constrained by the potential $U_z^{\mathrm{disc}}(z) = K_z z^2/2$, with $K_z = 2000\,\mathrm{kJ\,mol^{-1}\,nm^{-2}}$ and laterally by a soft potential of the form $U_{xy}^{\mathrm{disc}}(x,y) = K_{xy}(x^2+y^2)/2$ with $K_{xy} = 30\,\mathrm{kJ\,mol^{-1}\,nm^{-2}}$. The number of water molecules and the force constant K_{xy} are determined from the radial distribution function of a periodic two-dimensional water slab simulated using classical force fields, as explained in Appendix A.

The droplet system is constrained by a soft isotropic potential $U^{\mathrm{drop}}(x, y, z) = K_r(x^2 + y^2 + z^2)/2$ with $K_r = 40\,\mathrm{kJ\,mol^{-1}\,nm^{-2}}$, see Appendix A.

Chapter 3

External Potential Modifies Friction of Molecular Solutes in Water

Bibliographic information: Parts of this chapter and of Appendix B have previously been published. Reprinted with permission from Ref. [ii]. License: CC BY 4.0.

Friction sets the fundamental timescale for all processes that occur in a solvent. For a sphere with radius R in a continuous solvent with viscosity η the no-slip friction coefficient γ follows Stokes' law $\gamma = 6\pi\eta R$, so that the friction force F_f is for small enough velocity v given by $F_f = \gamma v$. Modifications of Stokes' law on the molecular scale due to water discreteness and water-solute interactions have been amply discussed [7, 180]. In this chapter we discuss a different modification of Stokes' law, demonstrated by MD simulations of a single methane in water that is subject to a harmonic confinement potential of strength K. In fact, we find γ to depend sensitively on K in the range $10^2\,\mathrm{kJ/(mol\,nm^2)} < K < 10^4\,\mathrm{kJ/(mol\,nm^2)}$ so that γ for larger K is increased by about 60% compared to the value of γ for small (or vanishing) K. This dramatic slowing down of the methane diffusivity in confinement is mirrored by an increase of the escape time from the first to the second hydration shell from $\tau_{esc1} \approx 8\,\mathrm{ps}$ for small K to $\tau_{esc1} \approx 18\,\mathrm{ps}$ for large K. The intimate coupling of solute and hydration shell dynamics had been suggested based on NMR studies that showed a solute to increase the viscosity in its hydration layer, which in turn slows down the solute diffusion, an effect that has been called secondary dynamic solvent effect [181]. Our results demonstrate a direct consequence of this coupling between solute and hydration shell dynamics: By a detailed analysis of the solute friction memory function, which we extract from our simulation trajectories using a novel method, we show that solute diffusivity and hydration shell kinetics are coupled and both influenced by the inherent timescale of solute motion, in our simulation model set by the external potential strength K.

There are various consequences of our findings: In simulation studies, it is common practice to constrain the position of a solute in order to determine spatially dependent

solvation properties in inhomogeneous systems, for example in hydrated lipid bilayer systems [182]. While this is unproblematic for static properties such as free energy profiles, our results show that this procedure potentially perturbs kinetic properties such as the diffusivity profile. In fact, there are various alternative techniques that allow to extract free energy and diffusivity profiles from simulation trajectories of unconstrained solutes [183, 184] and which therefore do not suffer from this potential complication.

The direct experimental test of our predictions is principally possible with optical traps, which are used to confine micron-sized plastic or metal beads in water [67]. Recent technological advances allow for the laser trapping of gold nanoparticles with a radius as small as 9 nm [185], which however is still much larger than the radius of a methane molecule employed in our simulations. Anti-Brownian electrokinetic trapping techniques have been demonstrated to efficiently trap single molecules with sub-nanometer hydrodynamic radii [186], but the achievable confinement potential strengths are rather weak. The potential-induced friction enhancement we observe for methane in water is expected to disappear for large solutes for which the inertial timescale $\tau_m \equiv m/\gamma$ (where m denotes the solute mass) is larger than the longest solvent relaxation time. Based on time scaling arguments, we argue in the Discussion section that the confinement-potential induced modification of the solute friction coefficient should be observable experimentally also for larger solutes, if the solvent relaxation time is suitably increased by using high-viscosity solvents.

A less direct but nevertheless relevant experimental consequence concerns the coupling between the dynamics of molecular probes and the surrounding hydration shell dynamics, which is studied by various experimental techniques. It is known that the hydration shell dynamics slows down considerably upon transferring a molecular probe from bulk water to the surface of a macromolecule, in line with our results. While in the experimental system the anchoring of a molecular probe not only confines the molecular probe but also changes its environment due to the presence of a linker group and an anchoring scaffold, it is clear that the confinement-induced mechanism we demonstrate in this chapter contributes also in these more complex experimental scenarios, as we will explain in the Discussion section.

3.1. Friction Constant in Harmonic Potential

For an unconfined solute the diffusion constant and the friction coefficient follow from the long-time limit of the mean-square displacement. Obviously, for a solute that is confined by an external potential this standard protocol is not applicable. Instead, we have to use a more indirect route and extract the friction coefficient γ from the symmetric memory function $\Gamma(t) = \Gamma(-t)$, defined by the generalized Langevin equation (GLE) [60, 73]

$$m\ddot{x}(t) = -\int_0^\infty dt'\, \Gamma(t')\dot{x}(t-t') - \nabla U(x(t)) + F_{\mathrm{R}}(t), \tag{3.1}$$

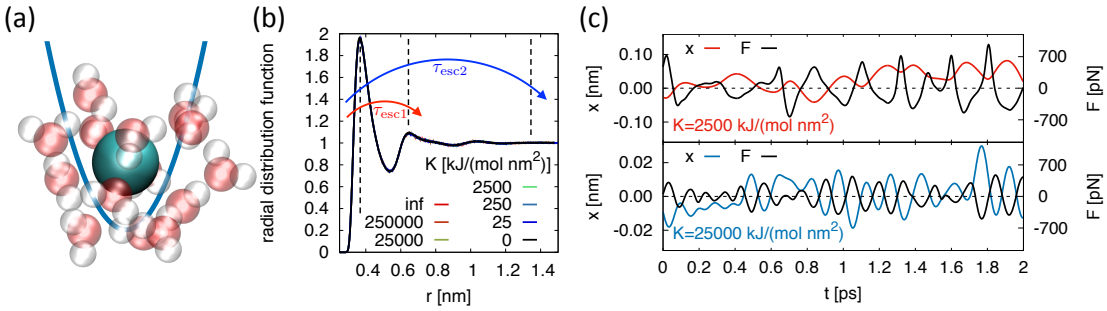

Figure 3.1.: Simulation setup. (a) A single methane is solvated in water and confined in an external harmonic potential of strength K. (b) Radial distribution functions (RDF) of the separation between methane and water oxygens for box size $L = 4.5\,\mathrm{nm}$ and different K including the frozen limit $K = \infty$, all curves perfectly superimpose. The positions of the first two maxima, used to calculate the mean escape time τ_{esc1}, and the positions used to calculate the mean escape time τ_{esc2}, are indicated by vertical dashed lines. (c) Methane position $x(t)$ and total force $F(t)$ trajectories for two different K values.

where $U(x) = \frac{1}{2}Kx^2$ is a harmonic potential, and $F_{\mathrm{R}}(t)$ denotes the random force, which obeys $\langle F_{\mathrm{R}}(0)F_{\mathrm{R}}(t)\rangle = k_{\mathrm{B}}T\Gamma(t)$ according to the fluctuation-dissipation theorem. We include the inertial term proportional to the solute mass m in order to correctly account for the short-time behavior where the solute dynamics is ballistic instead of diffusive. In some publications the upper integration boundary of the memory term in Eq. (3.1) is t instead of ∞. The two formulations are for positive time $t > 0$ related by a shift of the random force by $\Delta F_{\mathrm{R}}(t) = \int_0^\infty dt'\,\Gamma(t+t')\dot{x}(-t')$. Our formulation simplifies the Fourier analysis and does not require to specify initial conditions, for a detailed discussion we refer to Ref. [61]. Our novel method to extract the memory function $\Gamma(t)$ from simulation trajectories, which can also be used for experimental trajectories, is based on the solvent force experienced by the particle,

$$F_{\mathrm{sol}}(t) = m\ddot{x}(t) + \nabla U(x(t)). \tag{3.2}$$

The autocorrelation function

$$C_{FF}^{\mathrm{sol}}(t) = \langle F_{\mathrm{sol}}(0)F_{\mathrm{sol}}(t)\rangle \tag{3.3}$$

is after Fourier transformation $\tilde{C}_{FF}^{\mathrm{sol}}(\omega) = \int_{-\infty}^{\infty} dt\, e^{-i\omega t} C_{FF}^{\mathrm{sol}}(t)$ given by

$$\tilde{C}_{FF}^{\mathrm{sol}}(\omega) = \frac{k_{\mathrm{B}}T\,\tilde{\Gamma}(\omega)}{\left|1 - i\omega\tilde{\Gamma}_+(\omega)/(m\omega^2 - K)\right|^2}, \tag{3.4}$$

where we introduced the single-sided memory function $\Gamma_+(t) \equiv \Gamma(t)$ for $t \geq 0$ and $\Gamma_+(t) \equiv 0$ for $t < 0$ (see Appendix B for the full derivation). Since the friction coefficient

γ is given by $\gamma \equiv \int_0^\infty dt\, \Gamma(t)$, we see from Eq. (3.4) that for $K \neq 0$

$$\gamma \equiv \frac{\tilde{\Gamma}(0)}{2} = \frac{\tilde{C}_{FF}^{\mathrm{sol}}(0)}{2k_{\mathrm{B}}T} = \frac{1}{k_{\mathrm{B}}T}\int_0^\infty dt\, C_{FF}^{\mathrm{sol}}(t). \tag{3.5}$$

Note that in the limit $K = 0$ the integral over the force autocorrelation function $C_{FF}^{\mathrm{sol}}(t)$ vanishes and therefore cannot be used to extract γ, as amply discussed in the literature [187, 188].

3.2. Simulation Setup

We perform MD simulations of a single water-solvated methane modeled as a Lennard-Jones particle in a harmonic potential of strength K, see Fig. 3.1(a) for a schematic simulation setup. We use the GROMACS 5.1 [189, 190] simulation package. The Lennard-Jones parameters corresponding to methane are taken from the GROMOS 53a6 [191] force field, for water we use SPC/E [192] parameters. We perform NVT simulations with a time step of 2 fs at a temperature of $T = 300\,\mathrm{K}$, controlled by the velocity rescaling [193] thermostat coupled with a time constant of 0.5 ps to water only, for three different cubic box sizes $L = 3\,\mathrm{nm}$ (894 H_2O), $L = 4.5\,\mathrm{nm}$ (3008 H_2O) and $L = 6\,\mathrm{nm}$ (7159 H_2O). In the Appendix B we compare these results to simulations in the NVE ensemble and thereby demonstrate that the ensemble and the thermostat have no significant influence. We use simulation lengths of roughly 500 ns per parameter combination. Before the production runs, all systems are equilibrated for 5 ns in the NpT ensemble with $p = 1$ bar using a Berendsen [194] barostat to determine the box size. The solvent force $F_{\mathrm{sol}}(t)$ acting on the methane is calculated from the difference of the total force, which is due to interactions with all water molecules, and the force generated by the harmonic potential; in the case $K = \infty$ the methane is frozen at the potential minimum and the solvent force equals the total force. Position, velocity and total force acting on the methane are saved at every time step. Fast Fourier transforms are used for the calculation of autocorrelation functions and integrals over the solvent force autocorrelation function are computed by trapezoidal integration.

3.3. Results

Typical trajectories of the 1D methane position $x(t)$ and the conjugated total force $F(t) = m\ddot{x}(t)$ for two different values of K are shown in Fig. 3.1(c). As expected, the methane oscillates in the confining potential, with frequency and amplitude depending on the force constant K. In Fig. 3.1(b) radial distribution functions (RDF) of the methane-water oxygen separation are depicted for different K, including the frozen limit $K = \infty$. All RDFs superimpose perfectly, reflecting that the equilibrium properties of the methane hydration shell do not depend on K.

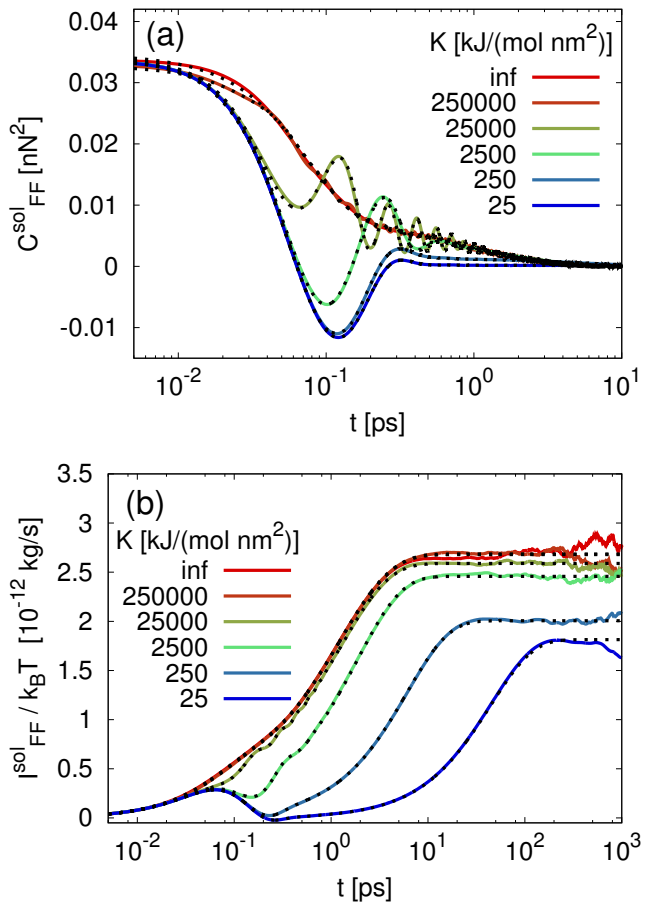

Figure 3.2.: Simulated solvent force autocorrelations for box size $L = 4.5$ nm. (a) Autocorrelation functions $C^{\mathrm{sol}}_{FF}(t)$ defined in Eq. (3.3) and (b) integrals $I^{\mathrm{sol}}_{FF}(t)$ defined in Eq. (3.6) for different confinement potential strengths K. Colored lines denote simulation results, dotted lines are analytic predictions according to Eq. (3.4) using the best-fit memory function $\Gamma(t)$.

We show simulated solvent force autocorrelation functions $C_{FF}^{\mathrm{sol}}(t)$ for different K as colored lines in Fig. 3.2(a), mild oscillatory behavior is seen, particularly for intermediate K. Note that position, velocity and force autocorrelation functions show more pronounced oscillations, as discussed in Appendix B.4. In Fig. 3.2(b) we show running integrals over the autocorrelations, defined by

$$I_{FF}^{\mathrm{sol}}(t) = \int_0^t dt'\, C_{FF}^{\mathrm{sol}}(t'), \tag{3.6}$$

as colored lines. According to Eq. (3.5), $I_{FF}^{\mathrm{sol}}(t \to \infty)/(k_{\mathrm{B}}T) = \gamma$ and thus the plateau values observed in Fig. 3.2(b) for large t reflect the friction coefficient γ. Most importantly, we see that the simulation prediction for γ significantly depends on K, which is somewhat unexpected, since the hydration structure around methane is independent of K, as witnessed by the RDF in Fig. 3.1(b).

3.3.1. Memory Function

To gain insight into this puzzling finding, we extract the memory function from simulation data. For this we introduce a variant of existing methods [6, 70, 73, 74, 76] that gives robust and reliable results for kernels and friction coefficients over a wide range of confinement potential strengths. We first observe that in the frozen limit, $K = \infty$, Eq. (3.4) predicts that $C_{FF}^{\mathrm{sol}}(t) = k_{\mathrm{B}}T\Gamma(t)$, i.e., in this limit, the solvent force autocorrelation function equals the memory function. We fit $C_{FF}^{\mathrm{sol}}(t)$ in Fig. 3.2(a) for $K = \infty$ by a sum of stretched exponentials

$$\Gamma(t) = \sum_{i=1}^{n} A_i \exp\left(-\left|\frac{t}{\tau_i}\right|^{\alpha_i}\right) \tag{3.7}$$

with $n = 2$, shown as a black dotted line. To extract $\Gamma(t)$ also for $K \neq \infty$, we calculate $C_{FF}^{\mathrm{sol}}(t)$ and $I_{FF}^{\mathrm{sol}}(t)$ numerically based on Eqs. (3.4) and (3.6) using the functional form Eq. (3.7) and extract the parameters by simultaneous fits (black broken lines) to the simulation data (colored lines) in Fig. 3.2(a) and (b); the agreement between fits and data is perfect.

The resultant memory kernels are presented in Fig. 3.3(a). They show a fast decay at 50 fs and a long-time tail extending to about 5 ps. In between, a pronounced and quite abrupt shoulder at a decay time of about 100 fs is present for intermediate K values, qualitatively similar to previous results for the diatomic kernel spectrum in Lennard-Jones fluids [74]. The fitted decay times τ_i are shown in Fig. 3.3(b), note that for intermediate K values we use $n = 3$ stretched exponentials for the fit (see Appendix B for details on the fit procedure, analysis of the robustness of the fit results, and a comparison with alternative methods). The shortest decay time τ_1 reflects water-methane repulsive interactions: from a fit to the short-distance part of the RDFs in Fig. 3.1(b) we estimate the fastest relaxation time as $\tau_1 = 58$ fs for $K = 0$ and $\tau_1 = 85$ fs for $K = \infty$ (see Appendix B.1 for details), in good agreement with the τ_1 data and

indicated in Fig. 3.3(b) by red arrows. The intermediate K-dependent decay time τ_2 agrees quantitatively with the harmonic oscillation period $\tau_0 = 2\pi\sqrt{m/K}$, shown as a broken line. The longest decay time τ_3 is rather independent of K and similar to the hydrogen-bond breakage time $\tau_{HB} \approx 1.4\,\mathrm{ps}$ [195], we thus associate this time with an intrinsic water relaxation time. We see in Fig. 3.3(a) that the memory kernel $\Gamma(t)$ changes with K only in the finite K range for which $\tau_1 < \tau_2 \approx \tau_0 < \tau_3$, i.e., when the harmonic oscillation period is between the shortest and longest memory relaxation times. The friction kernel thus results from the dynamic interplay of the methane harmonic oscillations, characterized by the relaxation time τ_2 and governed by the external potential strength K, with the solvent relaxation modes in the relaxation time window between τ_1 and τ_3. Based on this insight we develop a dynamic scaling argument for the behavior of large solutes in generic viscous solvents, see Discussion section.

While the fitted exponents α_1 and α_3 are not too different from unity and thus can be thought of as representing single-exponential relaxation modes, the exponent α_2 is of the order of 10, which indicates strongly non-linear relaxation (see Appendix B for details). It is this high value of α_2 which leads to the abrupt drop of the memory function at the timescale τ_2 visible in Fig. 3.3(a). Note that the hydrodynamic power-law tail predicted from continuum hydrodynamics [196], recently observed in optical trap experiments [67] and MD simulations of a supercritical Lennard-Jones fluid [71], makes a negligible contribution to $\Gamma(t)$ in the friction-relevant ps timescale, see Appendix B.

3.3.2. Friction Coefficient

The results for γ, obtained by the integral over the fitted $\Gamma(t)$, are presented in Fig. 3.4 for the three simulation box sizes considered and agree nicely with the limiting results for $K = \infty$ (obtained from simulations of a completely frozen methane), and $K = 0$ (obtained from mean-square displacements for a freely diffusing methane), as indicated by colored bars. The deviation of the $K = 0$ value from the experimental result $\gamma = 2.2 \cdot 10^{-12}$ kg/s [197] reflects that the SPC/E water viscosity is smaller than the experimental value. From the close agreement between the data for $L = 4.5\,\mathrm{nm}$ and $L = 6.0\,\mathrm{nm}$ we conclude that hydrodynamic finite size effects [198] are negligible for $L \gtrsim 4.5\,\mathrm{nm}$. Fig. 3.4 demonstrates that γ significantly depends on K and reaches at strong confinement ($K \to \infty$) a value about 1.6 times the free-diffusion limit ($K = 0$). These results are in qualitative agreement with previous simulations that demonstrated the friction of frozen ions to be larger than their free-diffusion values [199]. Note however that earlier simulation studies suggested frozen ions to be characterized by a smaller friction coefficient compared to free ions, a disagreement that was never discussed or settled [200, 201]. Together with our simulation results for a hydrated water molecule in an external potential, which are shown in Appendix B.2 and exhibit similar effects as for methane, we conclude that friction modification in confinement is thus a general phenomenon that applies to ions, non-polar as well as polar uncharged molecules. It transpires that simulations of frozen or confined molecules cannot be used to estimate the friction coefficient or the memory function of free molecules, since—as we

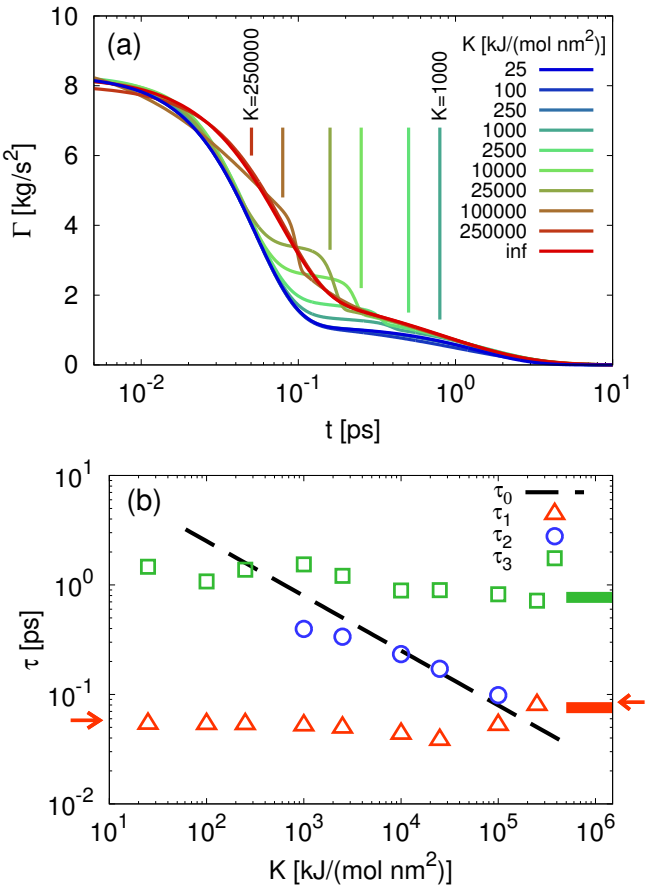

Figure 3.3.: Memory kernels. (a) Best-fit memory functions $\Gamma(t)$ according to the parametrization Eq. (3.7) for box size $L = 4.5\,\mathrm{nm}$ and different K. The result for the frozen case $K = \infty$ is shown as a red line. The harmonic oscillation periods $\tau_0 = 2\pi\sqrt{m/K}$ are indicated by vertical lines. (b) Fitted decay times τ_i (data points) from Eq. (3.7) as a function of K. Statistical errors are smaller than the symbol size. The two timescales for the frozen limit $K = \infty$ are denoted by horizontal colored lines on the right. The harmonic oscillation period $\tau_0 = 2\pi\sqrt{m/K}$ is shown as a dashed line, the relaxation times in the $K = 0$ and $K = \infty$ limits estimated from methane-water repulsive interactions are denoted by red arrows.

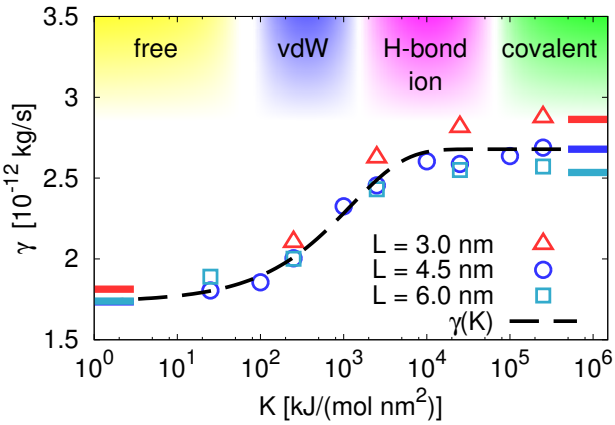

Figure 3.4.: Friction coefficient. Results for γ from the best-fit friction kernels are shown as a function of K for three simulation box sizes L. Statistical errors are of the order of the symbol size. The results for $K = 0$ and $K = \infty$ are obtained from free diffusion and frozen simulations and denoted by horizontal colored lines. For $L = 4.5\,\mathrm{nm}$ an empiric fit is included (dashed line).

show here—the memory function depends crucially on the precise strength of the confinement potential. The increase of γ with K, at first sight surprising in light of the decrease of τ_2 with K in Fig. 3.3(b), is solely caused by the prefactor A_3 of the slowest kernel contribution, as shown in Appendix B.3. Together with our interpretation that the slowest timescale τ_3 is related to an intrinsic water relaxation time that reflects the hydrogen-bond breakage dynamics, this means that the external confinement potential mostly modifies the hydration-shell contribution to the total friction.

We include typical values of K for van der Waals (vdW), hydrogen, ion and covalent bonds (estimated in the Appendix B) at the top of Fig. 3.4, and we see that the most drastic change of γ occurs in the range $K \approx (10^2 - 10^4)\,\mathrm{kJ/(mol\,nm^2)}$, which matches the strength of typical non-covalent bonds. We also include in Fig. 3.4 an empiric fit

$$\gamma = \gamma_\infty - (\gamma_\infty - \gamma_0)\exp\left(-\left(K/K_0\right)^c\right) \tag{3.8}$$

with the four fit parameters $\gamma_\infty = 2.67 \cdot 10^{-12}\,\mathrm{kg/s}$, $\gamma_0 = 1.73 \cdot 10^{-12}\,\mathrm{kg/s}$, $K_0 = 1,234\,\mathrm{kJ/(mol\,nm^2)}$ and $c = 2/3$ for the system with $L = 4.5\,\mathrm{nm}$. This simple function will be useful for comparison with other simulations and experimental data. The parameters K_0 and c correspond to the midpoint and the width of the potential strength range over which the friction changes with K. The small value of the exponent $c = 2/3$ reflects a rather broad range over which γ changes with K. Interestingly, the value K_0 corresponds to a methane mean-square displacement $\sqrt{\Delta x^2} = \sqrt{k_\mathrm{B}T/K_0} \approx 0.05\,\mathrm{nm}$, comparable to the width of the first hydration shell in Fig. 3.1(b).

3.3.3. Hydration Shell Dynamics

As mentioned in the introduction of this chapter, based on NMR experiments [180, 181] the friction coefficient of molecular solutes and the hydration shell dynamics have been shown to be coupled. In this section we explore the influence of an external potential acting on a solute on the hydration shell dynamics and in particular check whether the change of the friction coefficient with K is paralleled by a change of the hydration water relaxation dynamics. In Fig. 3.5(a) we plot the water escape time τ_{esc1} [202], defined as the mean first-passage time to reach the second hydration shell at water-methane separation $r = 0.65\,\mathrm{nm}$ starting from the first hydration shell at $r = 0.37\,\mathrm{nm}$ (see Fig. 3.1(b) for a graphical definition) as a function of K. The averages are calculated from typically 50,000 escape events per parameter combination, from which we estimate the relative error to be less than 1%. τ_{esc1} has the limiting values $\tau_{\mathrm{esc1}} = 8\,\mathrm{ps}$ for $K = 0$ and $\tau_{\mathrm{esc1}} = 18\,\mathrm{ps}$ for $K \to \infty$, showing that the increase of γ with K in Fig. 3.4 is paralleled by a slow-down of the escape dynamics of water molecules from the first hydration shell.

Water mean escape times and water translational relaxation times around molecular probes can experimentally be probed by Overhauser dynamic nuclear polarization techniques [203, 204]. Obviously, the increase of τ_{esc1} with K has a trivial contribution due to the fact that the relative distance coordinate relevant for the escape dynamics is governed by the sum of the methane and water translational diffusion constants [203]. To see this, we neglect for a moment that the methane position and the methane-water separation are dynamically coupled, and approximate the relative diffusion constant by the sum of the bulk translational diffusion constants $D_{\mathrm{rel}}^{\mathrm{trans}} = D_{\mathrm{CH_4}}^{\mathrm{trans}} + D_{\mathrm{H_2O}}^{\mathrm{trans}}$. In the completely confined case, corresponding to $K = \infty$, the methane diffusion constant $D_{\mathrm{CH_4}}^{\mathrm{trans}}$ is obviously zero and thus $D_{\mathrm{rel}}^{\mathrm{trans}} = D_{\mathrm{H_2O}}^{\mathrm{trans}}$. Approximating the relative diffusion constant to be independent of the methane-water separation (which we know from simulation studies on the relative motion of two water molecules not to be entirely true [205]), the reciprocal relationship between reaction times and diffusion constant, $\tau_{\mathrm{esc1}} \sim 1/D_{\mathrm{rel}}^{\mathrm{trans}}$, leads to the prediction $\tau_{\mathrm{esc1}}(K = \infty)/\tau_{\mathrm{esc1}}(K = 0) = (D_{\mathrm{CH_4}}^{\mathrm{trans}} + D_{\mathrm{H_2O}}^{\mathrm{trans}})/D_{\mathrm{H_2O}}^{\mathrm{trans}}$. From the simulation values $D_{\mathrm{CH_4}}^{\mathrm{trans}} = (2.38 \pm 0.01) \cdot 10^{-5}\mathrm{cm}^2/\mathrm{s}$ (see Appendix B) and $D_{\mathrm{H_2O}}^{\mathrm{trans}} = (2.70 \pm 0.02) \cdot 10^{-5}\mathrm{cm}^2/\mathrm{s}$ (calculated from the mean-square displacement of a single water molecule, taken from a 250 ns long simulation of pure water in a $L = 4.5\,\mathrm{nm}$ box) we thus obtain the estimate $\tau_{\mathrm{esc1}}(K = \infty)/\tau_{\mathrm{esc1}}(K = 0) = 1.88$, which is considerably smaller than the ratio $\tau_{\mathrm{esc1}}(K = \infty)/\tau_{\mathrm{esc1}}(K = 0) = 18\,\mathrm{ps}/8\,\mathrm{ps} = 2.25$ extracted from the simulation data in Fig. 3.5(a). Is the deviation of the simulated escape time ratio in Fig. 3.5(a) from the simple estimate associated with a change of the hydration water viscosity (and thus a change of $D_{\mathrm{H_2O}}^{\mathrm{trans}}$) in the first hydration shell with rising confinement potential strength K?

To look into this, we show in Fig. 3.5(b) the mean escape time τ_{esc2} for water molecules starting from the first hydration shell at $r = 0.37\,\mathrm{nm}$ and reaching the much higher distance $r = 1.37\,\mathrm{nm}$, for which we obtain values from $\tau_{\mathrm{esc2}} = 60\,\mathrm{ps}$ for $K = 0$ to $\tau_{\mathrm{esc2}} = 110\,\mathrm{ps}$ for $K \to \infty$. The mean escape times are higher by about an order of magnitude

compared to the results for τ_{esc1} in Fig. 3.5(a) and the change of τ_{esc2} with K is shifted to considerably lower values of K. The ratio of escape times from the completely immobilized and the free methane is now $\tau_{\mathrm{esc2}}(K=\infty)/\tau_{\mathrm{esc2}}(K=0) = 1.83$ and thus considerably smaller than the ratio obtained in the first hydration shell and quite close to our estimate based on the bulk diffusion constants $(D^{\mathrm{trans}}_{\mathrm{CH_4}} + D^{\mathrm{trans}}_{\mathrm{H_2O}})/D^{\mathrm{trans}}_{\mathrm{H_2O}} = 1.88$, as expected: the methane confinement does not seem to significantly influence the water dynamics beyond the first solvation shell. We conclude that while the main contribution to the translational slow-down of water in the first hydration shell around a methane with rising K comes from the trivial shift of the relative diffusion constant, a significant contribution to this slow-down comes from the modification of the water viscosity in the first hydration shell that accompanies the increase of the methane friction coefficient with rising K. This relates well with our finding that the change of γ with increasing K is predominantly caused by a variation of the long-time contribution to the memory function, as shown in Appendix B.3, which in turn is related to the intrinsic water dynamics.

The influence of the confinement potential on the hydration shell dynamics is more directly reflected by the water orientational dynamics around methane, since here we do not need to consider a relative coordinate. In Fig. 3.6(a), we show the orientation correlation function

$$C_{\mathrm{rot}}(t) = \langle P_2(\boldsymbol{u}(0)\cdot\boldsymbol{u}(t))\rangle \tag{3.9}$$

of water molecules with an initial separation below 0.4 nm around a free and a frozen methane molecule. Following previous studies [206], $\boldsymbol{u}(t)$ denotes the normalized vector along the OH bond of a water molecule and $P_2(x) = \left(3x^2-1\right)/2$ is the second Legendre polynomial. We include exponential fits $C_{\mathrm{rot}}(t) \propto \exp(-t/\tau^{\mathrm{rot}}_{\mathrm{CH_4}})$ for $t > 2\,\mathrm{ps}$ as dashed lines. The orientational relaxation times are $\tau^{\mathrm{rot}}_{\mathrm{CH_4}}(K=0) = 3.1\,\mathrm{ps}$ and $\tau^{\mathrm{rot}}_{\mathrm{CH_4}}(K=\infty) = 3.6\,\mathrm{ps}$ for free and frozen methane and thus differ by a factor of $\tau^{\mathrm{rot}}_{\mathrm{CH_4}}(K=\infty)/\tau^{\mathrm{rot}}_{\mathrm{CH_4}}(K=0) = 1.16$. The orientational relaxation time is inversely related to the rotational diffusion constant, $\tau^{\mathrm{rot}}_{\mathrm{CH_4}} \sim 1/D^{\mathrm{rot}}$, in the overdamped limit. We thus conclude that the rotational diffusion of water in the first solvation shell around a methane molecule slows down considerably as the translational methane motion is progressively inhibited by the increasing confinement potential.

In Fig. 3.6(b) we show orientation correlation functions of water molecules in the first hydration shell around a free and a frozen water molecule (note that in the frozen case both position and orientation of the central water molecule are fixed). The fitted relaxation times are $\tau^{\mathrm{rot}}_{\mathrm{H_2O}}(K=0) = 2.5\,\mathrm{ps}$ (in agreement with literature values [206]) and $\tau^{\mathrm{rot}}_{\mathrm{H_2O}}(K=\infty) = 3.8\,\mathrm{ps}$ and thus differ by a factor $\tau^{\mathrm{rot}}_{\mathrm{H_2O}}(K=\infty)/\tau^{\mathrm{rot}}_{\mathrm{H_2O}}(K=0) = 1.5$. Not surprisingly, due to the formation of directional hydrogen bonds, a frozen water molecule slows down the orientational hydration water dynamics much more than a frozen methane molecule.

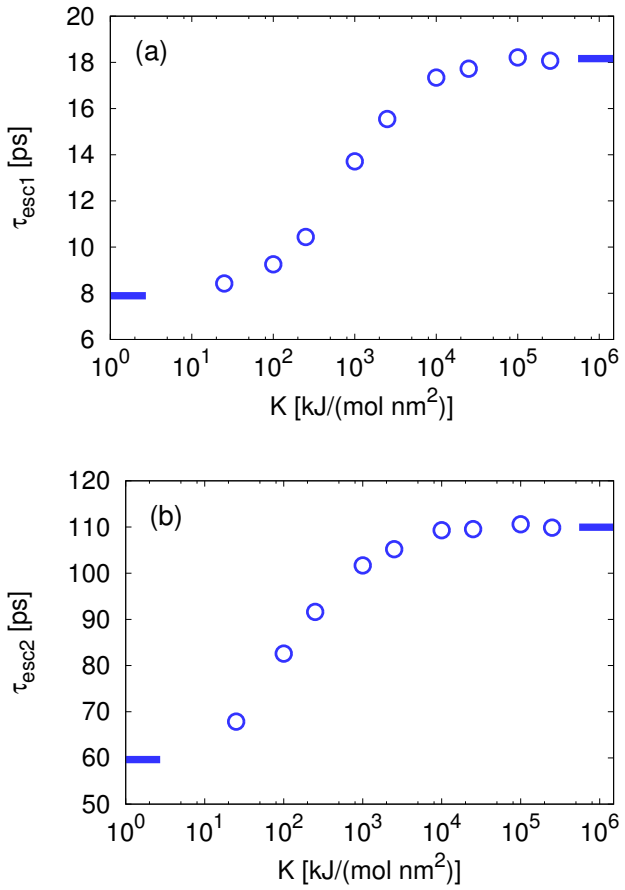

Figure 3.5.: Mean escape times of water from the first hydration shell around methane. (a) Results for τ_{esc1}, defined as the mean first-passage time from $r = 0.37\,\mathrm{nm}$ to a target distance of $r = 0.65\,\mathrm{nm}$ (indicated by dashed vertical lines in the RDF in Fig. 3.1(b)), are shown as a function of K. Results in the limits $K = 0$ and $K = \infty$ are denoted by horizontal lines. (b) The mean escape time τ_{esc2} from $r = 0.37\,\mathrm{nm}$ to a target distance of $r = 1.37\,\mathrm{nm}$ as a function of K.

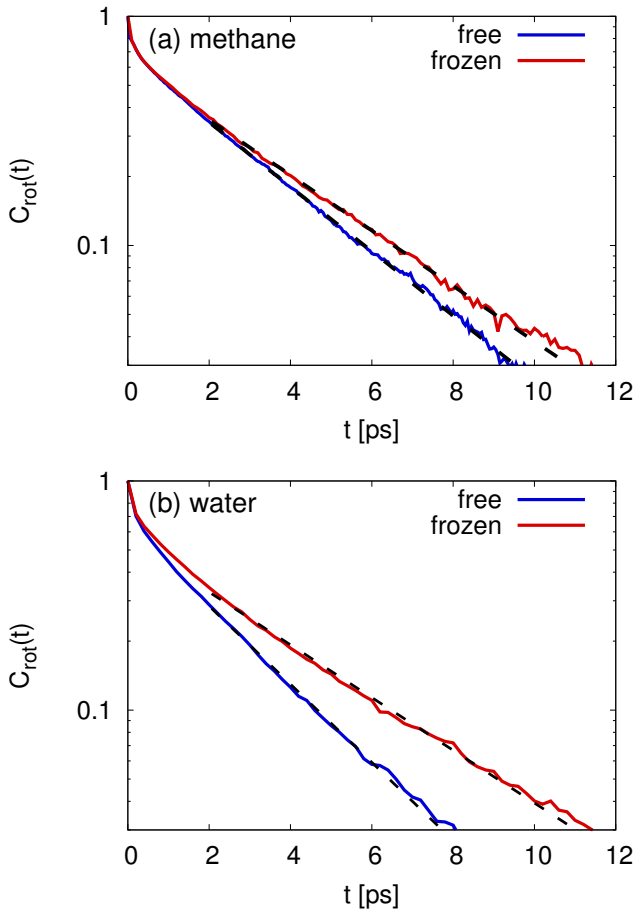

Figure 3.6.: Orientation correlation function $C_{\mathrm{rot}}(t)$ defined in Eq. (3.9) of water molecules within a radius 0.4 nm around (a) a free and a frozen methane molecule and (b) around a free and a frozen water molecule. Broken lines denote exponential fits for times $t > 2$ ps.

3.4. Discussion and Conclusion

In conclusion, the friction coefficient γ of a methane molecule is shown to significantly depend on the confinement potential strength K, which constitutes a generic and unexpected modification of Stokes' law $\gamma = 6\pi\eta R$. This reflects on the one hand that friction coefficients of fixed solutes differ from free solutes, as suggested previously [207], on the other hand it means that free-solution friction coefficients and memory functions cannot be obtained from confined or frozen simulations, contrary to common practice. More generally, our results demonstrate that friction and diffusion on the molecular scale result from the intricate dynamic coupling of solute and hydration degrees of freedom.

Interestingly, the maximal variation of the friction coefficient γ with K we find is similar to the change in γ of a sphere as one goes from a slip (characterized by $\gamma = 4\pi\eta R$) to a stick situation (in which case one recovers the standard result $\gamma = 6\pi\eta R$). Clearly, the similarity of this variation of γ to our results is purely coincidental.

For more complicated potentials involving multiple local minima and barriers, for example for proteins in a suitably defined folding landscape, we speculate that in analogy to our results obtained for methane in a harmonic potential, a local free energy minimum would produce a local increase in the conjugate friction landscape and, conversely, a free energy barrier would tend to reduce the local friction. Indeed, this might explain certain universal features seen in diffusivity landscapes extracted from water-explicit simulation trajectories of simple proteins [183]. Along the same lines, the diffusivity profile of a water molecule as a function of the distance from a planar wall indicates a reduced diffusion at local minima of the free energy profile [208].

The limit of an infinitely strong confinement potential $K \to \infty$ is equivalent to a solute with an infinite mass $m \to \infty$, which directly follows from the fact that the solute is at rest in both cases. By analogy with our results for the friction coefficient γ in Fig. 3.4, where a continuous increase with rising K is observed, we would expect that γ also goes up continuously as m increases. This is indeed confirmed by experimental measurements of the diffusion coefficient of different isotopes of molecules (such as $^{13}CO_2/^{12}CO_2$) and atoms (such as ^{3}He $/^4$He) in water [209], and will be studied extensively in the next chapter of this thesis.

The methane molecule is in our simulations represented as a simple Lennard-Jones sphere, so the friction increase and the hydration shell dynamics slowdown with rising K presumably is a rather universal effect that should hold for other molecular solutes as well. Indeed, the effect has been seen for ions in previous simulations [199–201] and in Appendix B.2 is demonstrated for a hydrated water molecule in an external potential, which serves as a simple model for a confined polar molecule.

Our simulation setup closely resembles optical trap experiments, where particles that are dispersed in aqueous solution are confined in laser-light-induced harmonic potentials [67]. The lower size limit of the trapped particles has reached the 10 nm scale [185], which is still substantially larger than the size of a methane molecule used in our simulations. Anti-Brownian electrokinetic trapping techniques allow to trap nanometer sized molecules [186], but the confinement potential strengths are rather weak. So the

legitimate question is whether the effects we predict survive for larger particles, for which a timescale discussion is needed.

The timescale above which a particle in a viscous solvent starts to feel frictional effects is on the scaling level given by the inertial timescale $\tau_{\mathrm{m}} \equiv m/\gamma$ (where m denotes the solute mass), at which the particle behavior crosses over from ballistic to diffusive [56]. Using the particle density ρ, particle radius R and the Stokes friction $\gamma = 6\pi\eta R$ we obtain $\tau_{\mathrm{m}} \sim \rho R^2/\eta$, from which we see that the inertial timescale increases strongly with particle radius R. An external harmonic potential of large strength K gives rise to an oscillation time $\tau_0 \simeq 2\pi\sqrt{m/K}$, for small K, in the overdamped regime, the timescale is rather $\tau_\gamma \simeq 2\pi\gamma/K$. The crossover between the oscillatory inertial and the overdamped regimes occurs at a critical potential strength $K^* \simeq \gamma^2/m \sim \eta^2/\rho R$ where one has $\tau_0 \sim \tau_\gamma \sim \tau_{\mathrm{m}}$. Using the notation we introduced when discussing our simulation results, we assume that the memory function is characterized by the longest and shortest relaxation times τ_3 and τ_1, respectively; in between these times there could in principle be a whole spectrum of intermediate relaxation modes. For water-solvated methane, we have argued that τ_3 is an intrinsic relaxation time of the solvent and thus independent of solute properties (in principle, τ_3 could also depend on internal solute relaxation modes for more complex, large solutes, which however does not change our argumentation and thus is not explicitly considered). The timescale τ_1 stems from the fast relaxation of solute-solvent interactions, i.e. the Lennard-Jones repulsion. Besides a trivial dependence via the relative mass of a solute-water pair (see Appendix B.1 for details), also τ_1 will be rather insensitive to the solute size. In Fig. 3.7(a) we show the potential timescales τ_0 and τ_γ as a function of K for a large particle, for which the inertial timescale τ_{m} is larger than the longest solvent relaxation time τ_3. In this case the particle oscillates in an inertial, friction-less fashion over the entire solvent relaxation time range $\tau_1 < t < \tau_3$ and we do not expect any dynamic coupling between the particle and the solvent for any value of K, in other words, an external potential does not influence the particle friction and all the effects we discuss in this chapter are absent.

In Fig. 3.7(b) we show the opposite situation where the inertial timescale τ_{m} is smaller than the longest solvent relaxation time τ_3. In the example shown in Fig. 3.7(b) the particle dynamics changes from inertial to diffusive within the solvent relaxation time range and in this case we do expect the particle friction γ to depend on the potential strength K. This is the situation we encountered in our simulations of methane in water and for which the memory kernel relaxation times are depicted in Fig. 3.3(b). Note that we draw the potential timescale in Fig. 3.7(b) in the time range $\tau_{\mathrm{m}} < t < \tau_3$ as a dotted line, since it is not clear whether in this time range it follows the oscillatory or the overdamped prediction; in fact, the simulation results in Fig. 3.3(b) seem to follow the oscillatory prediction $\tau_0 \simeq 2\pi\sqrt{m/K}$ in the entire range $\tau_1 < t < \tau_3$. To put in explicit numbers, with the methane mass $m_{\mathrm{CH_4}} = 16u = 2.7 \cdot 10^{-26}\,\mathrm{kg}$ and the methane diffusion constant $D^{\mathrm{trans}}_{\mathrm{CH_4}} = 2.38{\cdot}10^{-5}\mathrm{cm}^2/\mathrm{s}$ we obtain for the inertial timescale $\tau_{\mathrm{m}} = m_{\mathrm{CH_4}} D^{\mathrm{trans}}_{\mathrm{CH_4}}/k_B T = 15\,\mathrm{fs}$, which is even smaller than the fastest water relaxation time $\tau_1 = 58\,\mathrm{fs}$ for $K = 0$ or $\tau_1 = 85\,\mathrm{fs}$ for $K = \infty$.

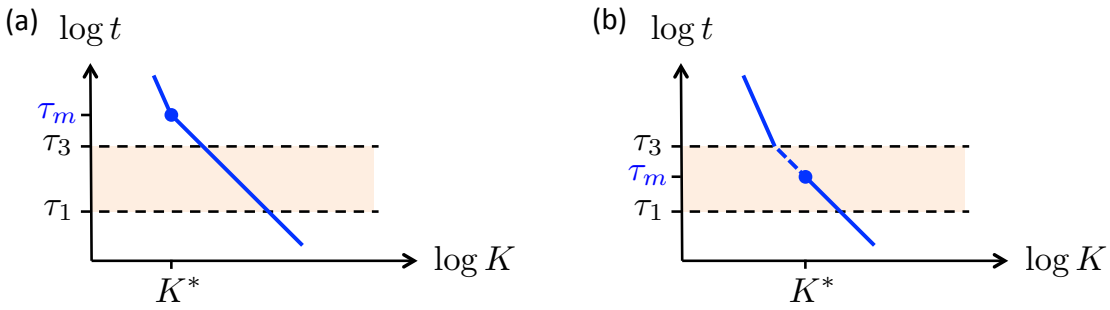

Figure 3.7.: Dynamic scaling diagrams for (a) a large solute particle and for (b) a small particle. In (a) the inertial timescale τ_{m} lies above the longest water relaxation time τ_3 and the particle relaxation time in the potential (shown as a solid line) changes from the harmonic oscillator prediction $\tau_0 \simeq 2\pi\sqrt{m/K}$ (for $K > K^*$) to the overdamped prediction $\tau_\gamma \simeq 2\pi\gamma/K$ (for $K < K^*$) above τ_3. In (b) τ_{m} is smaller than τ_3 and the potential relaxation time becomes overdamped within the relaxation time range. In this case we expect the external potential of strength K to modify the particle friction.

It transpires that the coupling scenario depicted in Fig. 3.7(b) can also for a large particle be obtained if the longest solvent relaxation time τ_3 is increased accordingly. This can be achieved by the use of highly viscous solvents, such as glycerol or polymer solutions. For entangled polymer solutions, the longest relaxation time scales as a power law with the polymer length and can thus be increased straightforwardly [24]. In essence, in order to be able to observe the K-dependent friction effects we describe in this chapter also with large particles, which can be easily confined in optical traps, one has to sufficiently increase the solvent viscosity which will lift the upper solvent relaxation time τ_3 and at the same time bring down the inertial timescale $\tau_{\mathrm{m}} \equiv m/\gamma$.

A fundamentally different experimental consequence of our results concerns the hydration shell dynamics around probe molecules, which is measured by a number of different experimental methods such as combined ^{2}H–^{17}O nuclear relaxation [180, 181], nuclear Overhauser effect [210], dynamic Stokes shift [211], Overhauser dynamic nuclear polarization [203], fluorescence [212], 2D infrared spectroscopy [213], quasi-elastic neutron scattering [214] and THz absorption [215, 216]. The water hydration dynamics around methane slows down significantly above potential strength values that correspond to covalent bonds, this is seen for the translational water motion in Fig. 3.5, although here the trivial shift of the effective relative diffusivity contributes (as discussed in Section 3.3.3), as well as for the orientational water dynamics in Fig. 3.6. These results thus suggest that hydration water relaxation times not only depend on the type of probe molecule, i.e. polar versus non-polar [217], but also on how tightly the probe molecule is confined or bound to a macromolecule.

The translational diffusion of hydration water relative to probes attached to proteins or lipid assemblies is experimentally observed to be about 3.5 to 5 times slower than

around probes that freely diffuse in bulk water [203, 214, 218], for probes attached to DNA segments a slowdown by only a factor of about 2 was reported [204], which seems to be the lower bound for these type of measurements. A similar slowdown of the orientational correlation time of hydration water at the protein water interface by a factor of about 2 compared to bulk was reported based on experiments [219] and simulations [206]. Clearly, when a probe molecule is anchored at a larger molecule, not only is its motion confined by an effective potential whose stiffness depends on the elasticity of the anchoring group, also the environment around the probe molecule is modified due to the presence of the linker groups and the scaffold to which the probe is attached, which for typical systems has been shown to be the main factor determining the hydration water dynamics around the probe [206, 220, 221]. Nevertheless, we argue that the confinement-induced friction modification we demonstrate in this chapter will certainly contribute to the water hydration slowdown—among other factors—and thus is a noteworthy mechanism.

In fact, in two experiments the flexibility of the scaffold onto which a probe molecule was anchored was varied without a drastic change in the environment of the probe. In a site-specific femtosecond-resolved fluorescence study using 16 tryptophan labeled myoglobin mutants, the water relaxation time was shown to be correlated with the local protein structural rigidity [212]. Based on THz absorption studies, the hydration shell relaxation dynamics was argued to become faster with increasing protein flexibility; in these experiments, the protein flexibility was modified by suitably chosen mutations [215]. The range over which a protein perturbs the hydration shell dynamics according to the analysis of THz experiments extends to several hydration layers, whereas in our analysis of translational water motion we only see an effect of the confining potential in the first hydration layer. Nevertheless, we conclude that these two experimental studies suggest that water hydration dynamics is coupled to the local rigidity of the probe molecule, even when the probe molecule is attached to a large protein. This is fully confirmed by simulations that show a significant slowdown of hydration shell dynamics around a frozen protein compared to a flexible protein of the same structure [222].

Chapter 4

Mass-Dependent Solvent Friction of a Hydrophobic Molecule

Bibliographic information: The content of this chapter and of Appendix C is in preparation to be submitted to a peer-reviewed journal (Ref. [iii]).

For many biophysical applications, the diffusivity of a particle is assumed to depend on solvent properties such as the viscosity η and particle-solvent interaction details but not on the particle mass. A prominent estimate for the no-slip friction coefficient γ of a particle with radius R is given by the Stokes relation $\gamma = 6\pi\eta R$, which has been shown to work down to molecular scales [38].

On the other hand, for geochemical applications, the fractionations of isotope ratios of noble gases in natural water bodies are an important indicator to understand various environmental processes [223–228]. Mass-dependent diffusion in water was therefore subject to analytical [229], simulational [230–233] and experimental [209, 234] efforts.

In this context, empiric power-law relations for the diffusion constant $D \propto m^{-\beta}$ with $0 < \beta \leq 0.5$ were found to hold over broad ranges of solute masses m [232], but their origin is understood poorly.

Based on molecular simulations of a hydrophobic particle of the size of a methane molecule in water (see Fig. 4.1(a)), we demonstrate in this chapter how the friction coefficient increases, when the particle mass is varied over 4 orders of magnitude, and that it saturates at a value roughly 1.6 times as large as for the physical methane mass $m = 16\,\mathrm{u}$ in the infinite mass limit, i.e., for a methane molecule fixed in space. Note that this limit is equivalent to the infinite confinement limit from the previous chapter. By extrapolation, we show that also in the massless limit $m \to 0$, which can be regarded as a model for a stable vacuum bubble, the friction constant as a function of mass saturates at about 0.9 times the physical methane friction. This saturation in the limit $m \to 0$ clearly indicates that the aforementioned power-law relations are purely empirical.

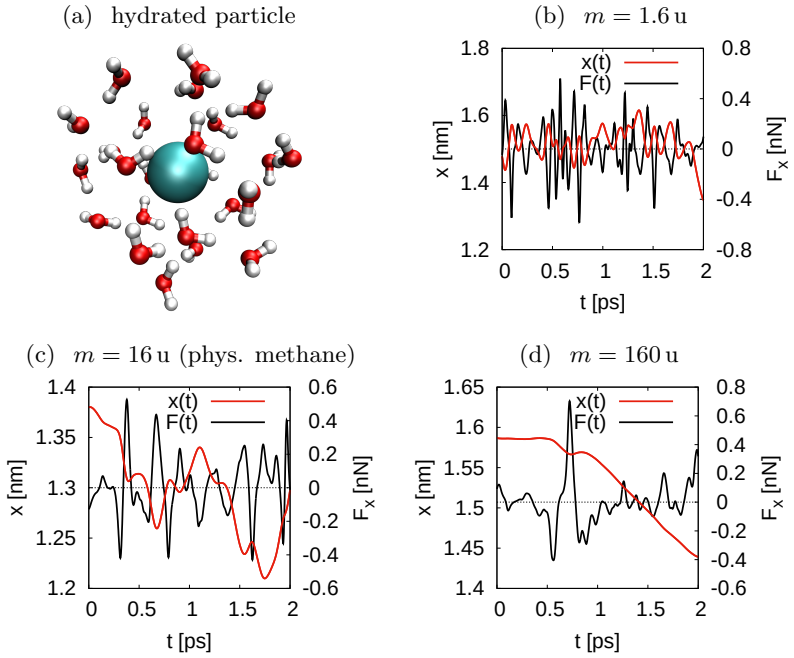

Figure 4.1.: (a) Visualization of a water-solvated methane molecule with its first hydration shell. (b)–(d) Typical simulated trajectories for the position $x(t)$ (red line) and the force $F_x(t)$ (black line) for different solute masses m.

Analytic predictions for the force autocorrelation function and the particle mean-square displacement based on the generalized Langevin equation (GLE) allow to extract the mass dependence of the solvent memory friction kernel for a hydrophobic particle in explicit water. Using the best-fit friction memory kernels, we show that these analytic predictions perfectly agree with simulation results.

To give a microscopic interpretation of the mass dependence of the friction constant, we calculate the mean escape times of water molecules from the first hydration shell of the methane molecule, and demonstrate that the hydration shell dynamics is significantly slowed down by an increased mass of the diffusing particle, with escape times being three times as long for a heavy than for a light particle. These results are in agreement with previous findings for ions [235], but the magnitude of this effect for a hydrophobic particle is surprising.

Our analysis allows a direct prediction of the diffusion constants for (similarly sized) methane isotopes. By a scaling analysis, we show that mass-dependent friction is expected also for larger particles, in particular in highly viscous solvents. Together with our finding from Chapter 3 that the friction of an externally confined methane molecule increases with confinement strength, the results from this chapter allow to speculate that the friction increase and the slowing down of the hydration shell dynamics due to

a reduced dynamic response of a solute to the solvent, is a quite universal phenomenon, which might be widely underestimated.

4.1. Simulation Details

The simulation setup closely resembles the setup from the previous chapter. We perform NVT molecular dynamics simulations of a Lennard-Jones particle in SPC/E water [192] at $T = 300\,\mathrm{K}$ using the GROMACS [189] simulation package version 4.6. As Lennard-Jones parameters for the particle we use the united atom parameters for a methane molecule from the GROMOS 53a6 [191] force field. The temperature is controlled by a velocity rescaling [193] thermostat, which is coupled exclusively to the solvent with a time constant of 1 ps. Before production runs, each system is equilibrated for 5 ns in the NPT ensemble using a Berendsen [194] barostat with $P = 1\,\mathrm{bar}$ to adjust the box size. The simulations for solute masses $m \geq 1.6\,\mathrm{u}$ are carried out with a timestep of 2 fs. For the lightest mass $m = 0.16\,\mathrm{u}$, we use a timestep of 0.5 fs.

Mean-square displacements (MSDs) are for $m \geq 1.6\,\mathrm{u}$ calculated from trajectories with a total simulation time of 1 μs each for the systems with $l = 3.0\,\mathrm{nm}$ (894 H_2O) and $l = 4.5\,\mathrm{nm}$ (3008 H_2O), and from 500 ns for the system with $l = 6.0\,\mathrm{nm}$ (7159 H_2O). For $m = 0.16\,\mathrm{u}$, we simulate trajectories of length 400 ns for $l = 3.0\,\mathrm{nm}$ and $l = 4.5\,\mathrm{nm}$, 200 ns for $l = 6.0\,\mathrm{nm}$. Mean-square displacements are calculated relative to the solvent center of mass, see Appendix C for a detailed discussion.

Force autocorrelation functions are obtained from 500 ns trajectories in the infinite mass limit, and from 100 ns trajectories for all other scenarios. The infinite mass limit (frozen) is realized by fixing the particle at the origin. Radial distribution functions and escape times are computed based on 50 ns trajectories with a time resolution of 50 fs.

4.2. Analytical Treatment

To investigate the interplay between the diffusing particle and the solvent, we compare the simulated systems to one-dimensional generalized Langevin dynamics. Diffusion in the presence of a friction memory kernel $\Gamma(t) = \Gamma(-t)$ can be described by the generalized Langevin equation (GLE) [56, 60]

$$m\ddot{x}(t) = -\int_0^\infty dt'\,\Gamma(t')\dot{x}(t-t') + F_\mathrm{R}(t), \tag{4.1}$$

where $x(t)$ denotes the particle position and $F_\mathrm{R}(t)$ refers to the random force, which obeys $\langle F_\mathrm{R}(t)F_\mathrm{R}(t')\rangle = k_\mathrm{B}T\,\Gamma\,(t-t')$ due to the fluctuation-dissipation theorem. The GLE can be rigorously derived by a linear projection technique [56, 60]. The derivation shows that the memory kernel represents the orthogonal degrees of freedom, which correspond to the solvent degrees of freedom in the present case. The generalized

Langevin equation implies that the friction constant γ defined via the diffusion constant $D = k_\mathrm{B}T/\gamma$ is equal to the integrated memory kernel, i.e.

$$\gamma = \int_0^\infty dt' \, \Gamma(t'). \tag{4.2}$$

We solve the GLE Eq. (4.1) by Fourier transform. For the calculation, we introduce $\Gamma_+(t) \equiv \Theta(t)\Gamma(t)$, so that the dissipative integral can be extended over the full time axis. $\Theta(t)$ denotes the Heaviside step function defined by $\Theta(t) = 0$ for $t < 0$ and $\Theta(t) = 1$ for $t \geq 0$. Solving the Fourier transformed GLE for $\tilde{x}(\omega) = \int_{-\infty}^{\infty} dt \, e^{-i\omega t} x(t)$ then yields

$$\tilde{x}(\omega) = \frac{\tilde{F}_\mathrm{R}(\omega)}{-m\omega^2 + i\omega\tilde{\Gamma}_+(\omega)}. \tag{4.3}$$

From the solution, one can calculate the autocorrelation function $C_{FF}(t) = \langle F_x(0)F_x(t)\rangle$ of the one-dimensional force $F_x(t) = m\ddot{x}(t)$

$$\tilde{C}_{FF}(\omega) = \frac{m^2\omega^4 k_\mathrm{B}T\tilde{\Gamma}(\omega)}{\left|m\omega^2 - i\omega\tilde{\Gamma}_+(\omega)\right|^2}, \tag{4.4}$$

as well as the mean-square displacement

$$\left\langle (x(t) - x(0))^2 \right\rangle = 2C(0) - 2C(t), \tag{4.5}$$

where $C(t) = \langle x(0)x(t)\rangle$ obeys

$$\tilde{C}(\omega) = \frac{k_\mathrm{B}T\,\tilde{\Gamma}(\omega)}{\left|m\omega^2 - i\omega\tilde{\Gamma}_+(\omega)\right|^2}, \tag{4.6}$$

with $\tilde{\Gamma}(\omega) = 2\,\mathrm{Re}\,\tilde{\Gamma}_+(\omega)$. Note that the expression Eq. (4.4) is equivalent to Eq. (3.4) from the previous chapter with $K = 0$.

4.3. Results

4.3.1. Mean-Square Displacements

Typical trajectories of the one-dimensional particle position $x(t)$ as well as of the one-dimensional force $F_x(t)$ obtained from the molecular dynamics simulations are depicted in Fig. 4.1(b)–(d) for the masses $m = 1.6\,\mathrm{u}$, $m = 16\,\mathrm{u}$ (physical methane) and $m = 160\,\mathrm{u}$. As a first step, we calculate the mean-square displacements (MSDs) $\left\langle \Delta\boldsymbol{r}^2(t)\right\rangle = \left\langle (\boldsymbol{r}(t) - \boldsymbol{r}(0))^2\right\rangle$ for all solute masses. For the system with $l = 4.5\,\mathrm{nm}$ they are shown in Fig. 4.2(a) and (b). As expected, the transition from the ballistic $\left\langle \Delta\boldsymbol{r}^2(t)\right\rangle \propto t^2$ to the diffusive regime $\left\langle \Delta\boldsymbol{r}^2(t)\right\rangle \propto t$ shifts to larger times for higher methane masses.

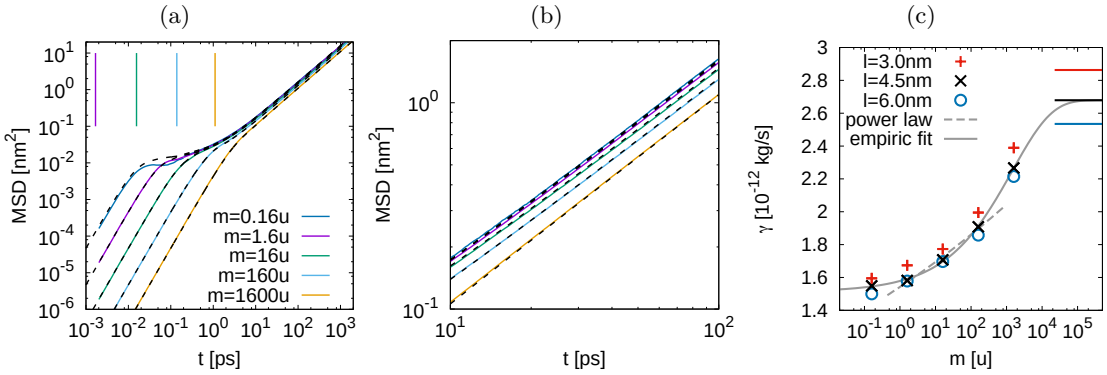

Figure 4.2.: (a) and (b) The simulated mean-square displacements (MSDs) of Lennard-Jones particles with different masses m in the system with $l = 4.5\,\mathrm{nm}$ (solid lines) compared to the analytic predictions for the MSDs based on the GLE Eq. (4.1) (dashed lines). In (a), the inertial timescale $\tau_m = m/\gamma$ is indicated by vertical lines. (c) The friction coefficients γ obtained from linear fits to the MSDs as a function of the particle mass m for all system sizes considered (data points). Estimated errors are smaller than the symbols. The friction coefficients from the integrated force autocorrelation functions of the frozen systems are represented by horizontal lines. For $l = 4.5\,\mathrm{nm}$, an empiric fit according to Eq. (4.7) is included as a solid line and a power-law fit $\gamma \propto m^\beta$ to the masses $0.16\,\mathrm{u} \leq m \leq 160\,\mathrm{u}$ is shown as a dashed line.

We calculate the diffusion constants from linear fits to the diffusive regime between $50\,\mathrm{ps} < t < 1\,\mathrm{ns}$.

The friction constants $\gamma = k_\mathrm{B}T/D$ are shown as a function of solute mass in Fig. 4.2(c). They decrease with increasing system size due to hydrodynamic self-interaction [198]. However, the comparison of the curves for $l = 4.5\,\mathrm{nm}$ and $l = 6.0\,\mathrm{nm}$ shows that finite-size effects are already reasonably small for $l = 4.5\,\mathrm{nm}$. We find a monotonic dependence of the friction constant γ on the particle mass m with an increase of a factor of almost 1.7 between the lightest mass and the frozen system. To interpolate the data, we fit the empiric function

$$\gamma = \gamma_\mathrm{inf} - (\gamma_\mathrm{inf} - \gamma_0) \exp\left[-\left(\frac{m}{m_0}\right)^c\right] \tag{4.7}$$

to the friction constants of the $l = 4.5\,\mathrm{nm}$ system (solid line in Fig. 4.2(c)). Using the friction coefficient $\gamma_\mathrm{inf} = 2.68 \times 10^{-12}\,\mathrm{kg/s}$ computed from the integrated force autocorrelation function of a frozen methane (see Section 4.3.3), we obtain the parameters $\gamma_0 = 1.51 \times 10^{-12}\,\mathrm{kg/s}$, $m_0 = 1461\,\mathrm{u}$ and $c = 0.39$. Thus, the simulation data extrapolates to a finite value $\gamma_0 = 1.51 \times 10^{-12}\,\mathrm{kg/s}$ for the friction constant of a massless Lennard-Jones sphere, which can be seen as a simple model for a stable vacuum bubble. In addition, we fit a power law $\gamma \propto m^\beta$ to the masses $1.6 \leq m \leq 160\,\mathrm{u}$ for the $l = 4.5\,\mathrm{nm}$ system (dashed line in Fig. 4.2 (c)) and obtain an exponent of $\beta = 0.04$. Our result

for β is a bit smaller than the exponents obtained earlier by MD simulation of isotopes of the noble gases He (0.17), Ne (0.15), Ag (0.08) and Xe (0.06) [232]. Note that this power-law fit is not consistent with the data points for $m = 0.16\,\mathrm{u}$ and $m = 1600\,\mathrm{u}$ nor with the massless or infinite mass limits.

4.3.2. Force Autocorrelation Functions

From the simulated trajectories, we calculate the autocorrelation functions $C_{FF}(t) = \frac{1}{3}\langle \boldsymbol{F}(0)\boldsymbol{F}(t)\rangle = \langle F_x(0)F_x(t)\rangle$ of the force $\boldsymbol{F}(t)$ experienced by the particle for the different masses as well as for a frozen particle corresponding to $m \to \infty$. The results for the system with $l = 4.5\,\mathrm{nm}$ are collected in Fig. 4.3(a) (colored solid lines). All curves show a fast initial decay with a mass-dependent decay length. For finite mass, the initial decay is followed by a negative regime. Whereas the autocorrelation function of the lightest particle ($m = 0.16\,\mathrm{u}$) is equal to zero for $t \gtrsim 0.1\,\mathrm{ps}$, we observe significantly non-zero correlation for $t \lesssim 5\,\mathrm{ps}$ for $m = 1600\,\mathrm{u}$ and in the frozen case.

In Fig. 4.3(b), the integrated force autocorrelation functions

$$I_{FF}(t) = \int_0^t dt'\, C_{FF}(t') \tag{4.8}$$

calculated from the MD trajectories are depicted. In all cases with finite mass, $I_{FF}(t)$ decays to zero, as one would expect [187], and as one can directly see from Eq. (4.4) since $\tilde{\Gamma}_+(0) = \gamma$ is finite. Note that thus, the friction constant cannot be obtained from this integral.

4.3.3. Frozen Fit

In the frozen case the free GLE Eq. (4.1) simplifies to $m\ddot{x}(t) = F_\mathrm{R}(t)$ since the particle is at rest, and the total force $F_x(t) = m\ddot{x}(t)$ is given by the random force $F_\mathrm{R}(t)$. Thus, the fluctuation-dissipation theorem implies $\Gamma_\infty(t) = C_{FF}(t)/k_\mathrm{B}T$. This approximation is referred to as the rigid bond approximation [74] and allows a direct calculation of the memory kernel $\Gamma_\infty(t)$ experienced by the frozen particle. We parametrize the kernel by a 3-exponential fit

$$\Gamma(t) = \sum_{i=1}^{3} A_i \exp\left(-|t|/\tau_i\right) \tag{4.9}$$

with the additional constraint $\frac{d\Gamma(t)}{dt}\big|_{t=0} = 0$, which follows from $\Gamma(t) = \Gamma(-t)$ if one assumes that the memory kernel is analytic. The fit is included in Fig. 4.3(a) as a dotted line, the fit parameters are given in Table C.1 in Appendix C.

We calculate the friction constant at infinite mass from Eq. (4.2) by evaluating the running integral $I_{FF}(t)$ shown in Fig. 4.3(b) at $t = 10\,\mathrm{ps}$, where the force autocorrelation has decayed to zero. We estimate the error to be less than 5% from the deviations between the numerical running integral and the integral over the fit according to Eq. (4.9)

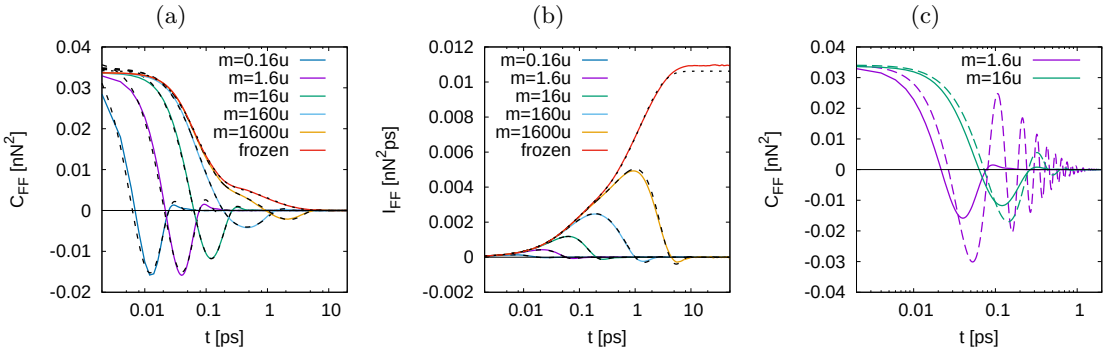

Figure 4.3.: (a) The simulated force autocorrelation functions $C_{FF}(t)$ for $l = 4.5\,\mathrm{nm}$ (solid lines) with the corresponding theoretical curves based on Eq. (4.4) using the memory kernels obtained by fits to the force autocorrelation function (dashed lines). In addition, the fit to the force autocorrelation function of the frozen particle according to Eq. (4.9) is included (dotted line). (b) The simulated integrated force autocorrelation functions $I_{FF}(t)$ (solid lines) with the analytical predictions based on Eqs. (4.4) and (4.8) (dashed lines), as well as the integrated fit for the frozen case (dotted line). (c) $C_{FF}(t)$ for $l = 4.5\,\mathrm{nm}$ (solid lines) with the theoretical curves based on Eq. (4.4) using $\Gamma_\infty(t)$ (dashed lines) for $m = 1.6\,\mathrm{u}$ and $m = 16\,\mathrm{u}$.

to the autocorrelation function of the frozen particle (included in Fig. 4.3(b) as a dotted line). The results for different simulation box sizes are included as horizontal lines in Fig. 4.2(c). For the system with $l = 4.5\,\mathrm{nm}$, the estimate for γ at infinite mass is about 1.6 times as large as for the methane mass $m = 16\,\mathrm{u}$. Clearly, the rigid bond approximation overestimates the friction dramatically, which agrees with the findings recently presented in Ref. [72] for several systems including HOD in H_2O.

4.3.4. Dynamic Fits

The mass dependence of the friction coefficient γ implies via Eq. (4.2) that the friction memory kernels $\Gamma(t)$ must differ as a function of particle mass. The parametrization Eq. (4.9), allows to evaluate Eq. (4.4) analytically with

$$\tilde{\Gamma}_+(\omega) = \sum_{i=1}^{3} \frac{A_i \tau_i}{1 - i\omega\tau_i}. \tag{4.10}$$

Using the result, we fit the coefficients of the parametrization Eq. (4.9) by matching the analytic predictions Eq. (4.4) for the force autocorrelation function in the time domain to the simulation results. According to Eq. (4.2), we additionally constrain the integral over the kernel to be equal to the friction constant obtained from MSDs to correctly recover the long-time dynamics. The force autocorrelation functions are fitted successively with decreasing mass, where we use the results from the previous fit as a

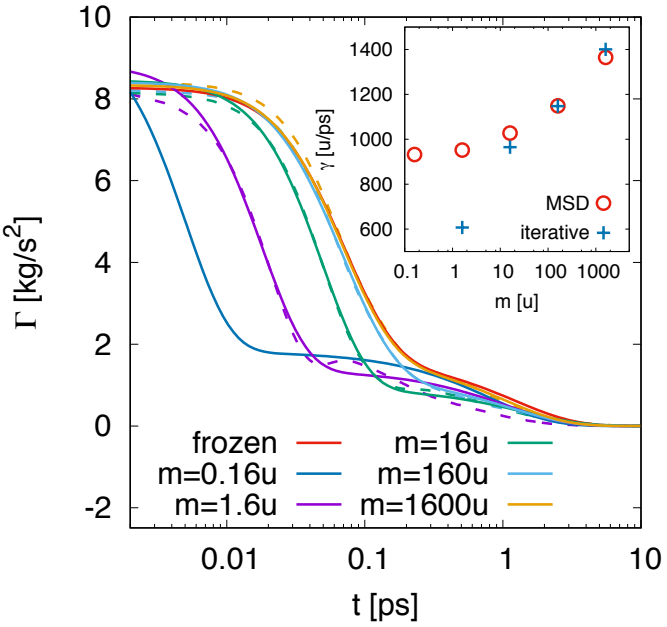

Figure 4.4.: The memory kernels $\Gamma(t)$ extracted from the simulation data for the system with $l = 4.5\,\mathrm{nm}$ by fitting $C_{FF}(t)$ (solid lines) and by iteratively solving Eq. (4.11) (dashed lines). In the inset, the friction constants calculated from the integrated memory kernels $\gamma = \int_0^t dt'\,\Gamma(t)$ obtained by Eq. (4.11) (blue plus symbols) are compared to the values from MSDs (red circles).

starting point. Note that this method is similar to the method we applied in Chapter 3 to extract the memory kernels of harmonically confined methane. The analytically predicted autocorrelation functions are included in Fig. 4.3(a) and (b) as dashed lines. Clearly they show very good agreement. In Fig. 4.3(c), it is shown that the memory function $\Gamma_\infty(t)$ from the rigid bond approximation results into significant disagreement between the predicted force autocorrelation functions $C_{FF}(t)$ (dashed lines) and the simulation results (solid lines) for smaller masses.

The resulting memory kernels for $l = 4.5\,\mathrm{nm}$ are depicted in Fig. 4.4 as solid lines, their parameters are given in Table C.1 in the Appendix C. For larger masses $m \geq 16\,\mathrm{u}$, the amplitude of the long-time tail increases significantly with the solute mass and the kernels approach the result from the frozen methane (red solid line). For $m \leq 16\,\mathrm{u}$, the short-time decay time τ_1 is significantly faster than for larger masses. The amplitude of the long-time tail increases with lighter masses in this case, but the associated decay time τ_2 goes down at the same time. A plot of the timescales τ_1 and τ_2 as a function of solute mass is shown in Appendix C. Since the memory kernels represent the projected degrees of freedom, i.e., the coordinates and velocities of the solvent molecules, we conclude that the dynamic solvent properties significantly change as a function of the diffusing particles mass.

Additionally, we calculate the MSDs from Eqs. (4.5) and (4.6), which are sensitive to short and long-time dynamics. The analytical results are included as dashed lines in Fig. 4.2(a) and (b). Also they show perfect agreement (up to small deviations around $0.1\,\mathrm{ps}$ for the lightest mass $m = 0.16\,\mathrm{u}$).

4.3.5. Alternative Methods

The method for the computation of the memory kernels employed here is based on the parametrization Eq. (4.9). There are several methods for the computation of memory kernels from atomistic trajectories which do not rely on a parametrization of the memory kernel [61, 70, 72, 74, 236]. However, the excellent agreement between simulations and analytical predictions (Fig. 4.2(a),(b) and Fig. 4.3(a),(b)) clearly indicates that we extracted the relevant features of the memory kernels. As an additional cross check, we compute the memory kernels by iteratively solving the relation [236]

$$m\frac{dC_{vv}(t)}{dt} = -\int_0^t dt'\,\Gamma(t-t')C_{vv}(t'), \tag{4.11}$$

after discretizing the integral as a sum. Here, $C_{vv}(t) = \langle \dot{x}(t)\dot{x}(0)\rangle$ denotes the velocity autocorrelation function. We remark that a similar method was used to study the mass dependence of friction memory kernels for ions in Ref. [233]. For the lightest mass $m = 0.16\,\mathrm{u}$ this method results in a kernel which does not decay to zero (not shown). The memory kernels for the other masses are included as dashed lines into Fig. 4.4, and they qualitatively agree well with our results. The most pronounced disagreement is observed for $m = 1.6\,\mathrm{u}$. However, the long-time contributions obtained by solving Eq. (4.11) are significantly underestimated for $m = 1.6\,\mathrm{u}$, since the integral over the

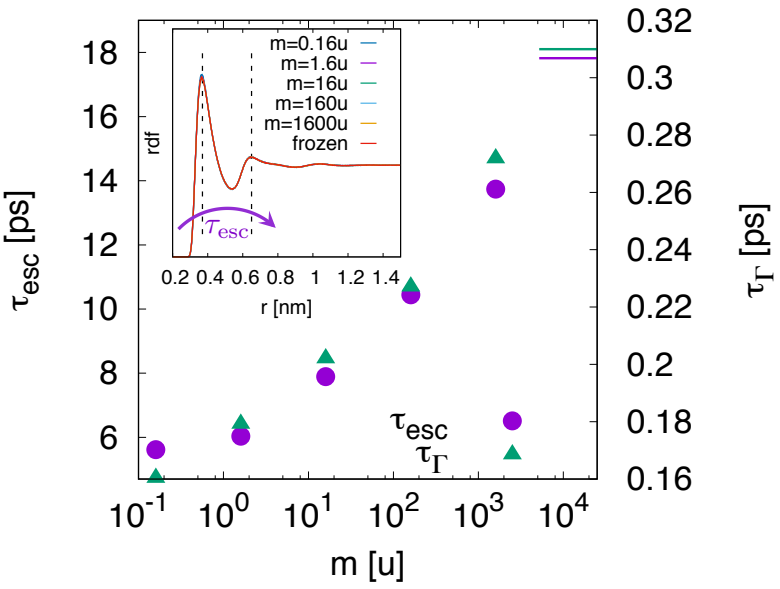

Figure 4.5.: The mean escape time τ_{esc} of water molecules from the first hydration shell, defined as the mean first-passage time from the first to the second maximum (indicated by dashed lines) of the radial distribution function of the oxygen atoms around the particle (shown in the inset) as a function of mass m (circles). For comparison, the effective memory time τ_Γ is included (note the different axes).

respective kernel shown in the inset of Fig. 4.4 as a function of mass (plus symbols) is 40% to small. For the memory kernels obtained by fits to the force autocorrelation function, the integral is equal to the friction constant by construction.

4.3.6. Mean Escape Times

To elucidate the molecular origin of the mass-dependent friction, we compute the mean escape time τ_{esc} of a water molecule from the first hydration shell of the solvated particle, defined as a mean first-passage time from $r = 0.37\,\text{nm}$ to $r = 0.65\,\text{nm}$, where r denotes the distance between the particle and the water molecule of interest. This definition is illustrated in the inset of Fig. 4.5; the two radii are indicated by vertical dashed lines. The escape time τ_{esc} is shown as a function of mass in Fig. 4.5, and it significantly depends on the mass of the solute; it increases by a factor of three over the mass range considered. Hence, the dynamics of the first hydration shell around heavier particles is significantly slower than around lighter particles.

Additionally, the effective memory time defined by

$$\tau_\Gamma = \frac{\gamma}{\Gamma(0)} = \frac{1}{\Gamma(0)} \int_0^\infty dt\, \Gamma(t) \tag{4.12}$$

is included in Fig. 4.5 for the memory kernels shown in Fig. 4.4. Clearly, the two observables obey the same qualitative trend, i.e. slower solvent relaxation around more massive particles.

4.4. Conclusions and Discussion

In summary, we have shown that the friction constant of a methane molecule increases significantly with the solute mass, with finite limits for zero and infinite mass. We have modeled the diffusion process in terms of a generalized Langevin equation and we have shown that the long and short-time contributions of the memory kernel depend on the solute mass. These findings go clearly beyond predictions from hydrodynamics. We have elucidated the origin of the friction increase by showing that the mean escape times of water molecules from the first hydration shell of the methane molecule increase monotonically by up to a factor of three with increasing solute mass.

From the fit $\gamma \propto m^{\beta}$ around the physical methane mass included in Fig. 4.2(c), the friction constant of $^{14}CH_4$ ($m = 18\,\mathrm{u}$) in H_2O is estimated to be about 0.46% larger than for $^{12}CH_4$ ($m = 16\,\mathrm{u}$) in H_2O. For $^{13}CH_4$ ($m = 17\,\mathrm{u}$) we estimate the friction constant to be about 0.23% larger than for $^{12}CH_4$. These differences can be resolved experimentally [234, 237], and particularly the result for $^{13}CH_4$ might be a small correction to better understand bacterial methane isotope fractionation [238–240]. Furthermore, hydrogen-deuterium isotopes of methane will also show a mass dependence of the diffusion constant, but in these cases, also the molecule size will depend more strongly on the type of isotope due to the mass dependence of the ground state energy of the bond vibration, which should be taken into account.

Since the massless limit can be regarded as a simple model for a stable vacuum bubble, one might conclude that it is a general principle that vacuum bubbles on the molecular scale diffuse faster than similarly sized massive objects. However, since actual vacuum bubbles can deform and since the rigid Lennard-Jones particle introduces a spurious interaction between non-neighboring water molecules this conclusion remains speculative.

The timescale at which frictional effects become relevant is given by the inertial timescale $\tau_m = m/\gamma$ (indicated by horizontal lines in Fig. 4.2(a)), which reflects the crossover from ballistic to diffusive behavior [56]. For the heaviest particle considered, where the friction is about 10% smaller than for frozen methane (see Fig. 4.2(c)), we have $\tau_m = 1.2\,\mathrm{ps}$. The latter timescale is in the order of magnitude of the decay time τ_2 of the long-time tail of the memory kernels shown in Fig. 4.4. Hence, we expect mass-dependent friction to be relevant for $\tau_m \lesssim \tau_2$. This observation allows us to carry out a similar scaling analysis than presented in Chapter 3, in order to answer the question in how far mass-dependent friction is relevant for larger solutes. As an estimate for the friction, we use the Stokes formula $\gamma = 6\pi\eta R$ with an effective radius R. The mass of the solute will then depend on the radius according to $m \sim \rho R^3$, where ρ denotes the particle density. Thus, we can estimate the inertial timescale

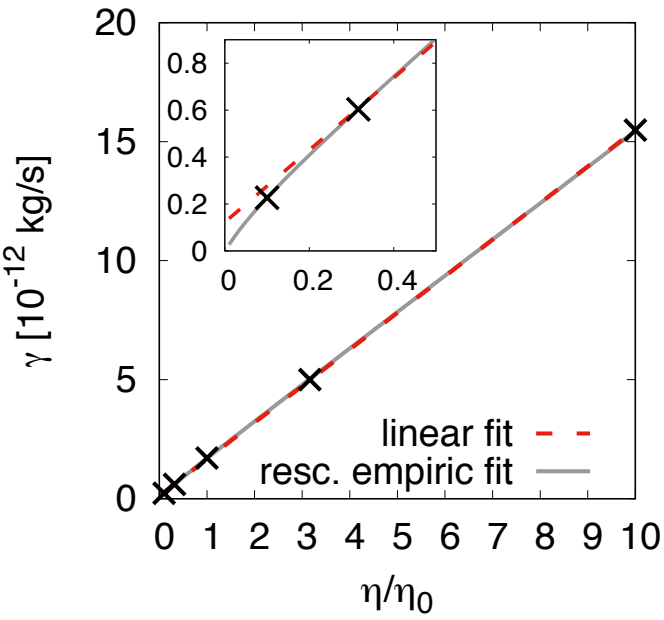

Figure 4.6.: The friction constant of physical methane in water with different water molecule masses as a function of viscosity η/η_0, where η_0 denotes the normal SPC/E water viscosity. The rescaled empiric fit Eq. (4.7) is included as a gray solid line, a linear fit according to Eq. (4.14) is included as a red dashed line. In the inset, the low-viscosity region is enlarged.

$\tau_m \sim \rho R^2/\eta$, and we conclude that mass-dependent friction will occur for $\rho R^2/\eta \lesssim \tau_2$. Since the longest timescale of the memory kernel τ_2 increases with viscosity, whereas τ_m decreases, we expect mass-dependent friction to be relevant even for nanometer sized objects in highly viscous solvents like polymer solutions. Clearly, objects of this size vary significantly in mass depending on the material composition. For physical methane, we have $\tau_m = 16\,\mathrm{fs} \ll \tau_2$. Thus, also in water, we expect mass-dependent friction for (sufficiently rigid) solutes that are larger than methane.

Our results show that power-law relations of the form $D \propto m^{-\beta}$ do not hold over the complete range of solute/solvent mass ratios. In particular the finite friction constant observed for $m \to 0$ is in contradiction to such a relation. The power law is motivated by kinetic gas theory, where one has $D \propto \mu^{-0.5}$, with $\mu = mm_0/(m + m_0)$ denoting the reduced mass of the tracer particle and a gas molecule with masses m and m_0 respectively. Applying the power-law relation over the whole mass range considered here would thus require to introduce an effective hydration shell mass, which could indeed be consistent with saturation of the friction constant at infinite mass, but it would clearly be inconsistent with the observed saturation at $m \to 0$.

By a rescaling of the simulation time $\propto \sqrt{m/m_{\mathrm{CH_4}}}$, our simulations are equivalent to simulations of physical methane in water with a rescaled water molecule mass

$$m_{\mathrm{w}} = (m_{\mathrm{CH_4}}/m)\, m_{\mathrm{H_2O}}, \tag{4.13}$$

where $m_{\mathrm{CH_4}} = 16\,\mathrm{u}$ and $m_{\mathrm{H_2O}} = 18\,\mathrm{u}$ denote the physical methane and water masses, and m is the simulated methane mass. Since the viscosity η scales according to $\eta \propto \sqrt{m_{\mathrm{w}}}$ [241], we can plot the (rescaled) methane friction as a function of water viscosity in Fig. 4.6. The rescaled empiric fit Eq. (4.7) is included as a gray solid line. The solute-mass dependence of the friction constant discussed so far translates then into a deviation from a linear viscosity dependence of the friction constant. We fit a linear function

$$\gamma = \gamma_a + \gamma_b(\eta/\eta_0) \tag{4.14}$$

to the data points (dashed red line in Fig. 4.6), where we obtain $\gamma_a = 0.12 \times 10^{-12}\,\mathrm{kg/s}$ and $\gamma_b = 1.53 \times 10^{-12}\,\mathrm{kg/s}$. The non-zero offset γ_a, which corresponds to 7% of the methane friction in normal SPC/E water, could be interpreted as apparent internal friction. Note, however, that this expression is misleading because the Lennard-Jones particle used for this work has no internal degrees of freedom.

The mean residence time of water molecules in the first hydration shell, i.e., the mean time a water molecule stays in the first hydration shell, has been linked to the mass of diffusing ions and (hypothetical) ion isotopes previously [231, 233, 235]. The mean escape time is related, but it has the advantage to be less sensitive to (oscillatory) short-time movements of the particle itself, which is relevant for small particle masses. Compared to an ion, a hydrophobic particle is expected to interact less with the solvent molecules. Thus, the magnitude of the hydration shell dynamics slow-down demonstrated here is quite surprising, and we speculate that this effect is universal and of (possibly underestimated) importance for the interpretation of dynamical properties of a broad class of systems.

Since equilibrium properties are independent of the particle mass, the mass-dependent friction can only be explained by the cooperative dynamics of the water molecules and the particle. A heavy or frozen particle will show little immediate reaction to the water dynamics, whereas a lighter particle will more cooperatively diffuse with the water molecules. I.e., the reduced response to the water molecules itself must slow down the hydration shell dynamics. Hence, it goes along with longer residence times of the water molecules near the surface.

In Chapter 3, we have shown that a water-solvated methane molecule confined by an external potential is subject to increased friction with increasing potential strength. We conclude that molecular friction is naturally influenced by the coupling of hydration and particle dynamics. As a general principle, a reduced response of a solute to the solvent appears to be accompanied by increased friction.

Chapter 5

Butane Dihedral Angle Dynamics in Water is Dominated by Internal Friction

Bibliographic information: Parts of this chapter and of Appendix D have previously been published. Reprinted with permission from Ref. [iv].

For the understanding of conformational and biochemical reactions, a low-dimensional stochastic description in suitable reaction coordinates is a powerful approach. In particular in the context of protein folding, diffusion in a one-dimensional free-energy landscape is a prominent model to come to terms with the high-dimensional phase-space dynamics of proteins [45, 46, 48]. By projection onto a one-dimensional reaction coordinate, orthogonal degrees of freedom produce effective friction and random force contributions [56, 60]. These byproducts of projection cannot be neglected, since friction decisively influences reaction rates [242].

Obviously, the friction that characterizes a protein folding coordinate contains contributions from the surrounding solvent as well as from internal protein degrees of freedom [10], but it is less clear how to separately measure these two contributions (experimentally or in simulations). Typically, the prime object in protein studies concerned with friction effects is the folding time τ_{fold}. In the overdamped limit, when inertia and memory effects are neglected, τ_{fold} scales with the effective friction coefficient γ as $\tau_{fold} \sim \gamma$ [242]. By the addition of viscogenic agents the solvent viscosity η increases relative to the pure water value; assuming that solvent and internal friction are additive according to $\gamma = \gamma_{sol} + \gamma_{int}$ and furthermore that Stokes' law holds for the solvent friction contribution, $\gamma_{sol} \sim \eta$, the internal contribution γ_{int} can be obtained by linear extrapolation of $\tau_{fold} \sim \gamma_{sol} + \gamma_{int}$ down to vanishing solvent viscosity [10]. Via this procedure, internal friction has been demonstrated for various proteins [8, 10, 25–29, 52, 243, 244]. In fact, deviations from a linear dependence $\gamma_{sol} \sim \eta$ have been experimentally observed for some proteins [25], while for other proteins no internal friction was detected at all [11]. Even in simulations, where—in contrast to experiments—the water friction

can be reduced and a modification of the folding free energy landscape with changing viscosity can be excluded, the extrapolation down to vanishing solvent friction is not trivial [119–122, 241].

The above definition of internal friction hinges on a few critical assumptions which are not necessarily satisfied in real systems: i) It was pointed out that inertia effects lead to deviations from the simple law $\tau_{fold} \sim \gamma$ and ultimately to Kramers turnover, which can be misinterpreted as internal friction [117, 245, 246]. While one would intuitively think that the effective mass of a protein reaction coordinate is small, the balance of effective inertial and friction parameters of reaction coordinates that describe complex reactions is not really settled. ii) Friction will in general not be constant along a reaction coordinate [241, 244], so the linear additivity assumption $\gamma = \gamma_{\mathrm{sol}} + \gamma_{\mathrm{int}}$ not necessarily holds when averaged over the reaction coordinate and needs to be checked directly. iii) Most serious are memory effects, which decisively influence barrier crossing dynamics [120]. Recently it was shown that memory effects can, depending on the value of the memory time, slow down or even accelerate barrier crossing [vi], which starkly invalidates the overdamped Kramers scaling $\tau_{fold} \sim \gamma$.

Previous theoretical approaches to internal friction are based on reaction times, they suffer from the indirect connection between transition times and friction and necessarily rely on various model assumptions [119–122, 241] (not so different from the experimental situation). Direly needed are models which allow to check for the presence of internal friction independently of any theoretical assumptions that relate friction to reaction times, as well as methods to extract friction and memory functions directly from simulations instead of inferring friction effects indirectly from measured reaction times.

In this chapter we introduce methods to meet both challenges. We consider butane, since it is the simplest molecule that shows a non-trivial conformational transition in a solvent and since it has been a testing ground for theoretical and experimental developments [247–251]. In fact, dihedral isomerization rates are known to be quite insensitive to the solvent viscosity [116–124] which was argued to be due to inertial and memory effects [120, 252, 253]. In our work, we first simulate a single butane molecule in water and compare two scenarios, the free scenario, where all four carbons can freely move, subject to bond length and bond angle constraints, and the constrained scenario, where three carbons are fixed in space and only one terminal carbon can move. While the free energy landscape for the dihedral is the same in both scenarios, the transition times differ for high water viscosities (which we modify in our simulations by changing the water mass) by a factor of ten. This unequivocally demonstrates that the additional butane degrees of freedom (which are orthogonal to the dihedral angle) in the free scenario significantly change the effective friction along the reaction coordinate. Secondly, we introduce a method to extract the friction memory kernel that couples to the reaction coordinate, in our case the dihedral angle, from simulation trajectories. A memory kernel accounts for the fact that friction on the molecular scale is not instantaneous but rather depends on the system's history in a non-Markovian manner. Our calculated memory kernels reveal that indeed the friction substantially differs between the constrained and free butane scenarios. The friction coefficients,

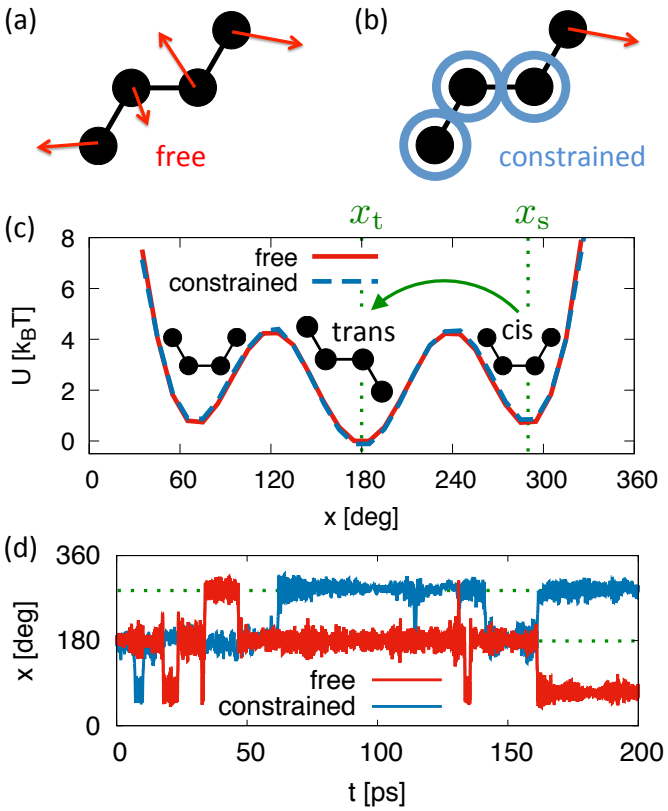

Figure 5.1.: Schematic illustration of (a) a free butane molecule where all four carbons can move and (b) a constrained butane where three carbons are fixed in space and only one terminal carbon can move. (c) Comparison of the free energy U as a function of the dihedral angle x for the free and constrained butane solvated in SPC/E water, extracted from simulation trajectories. The starting and target angles x_s and x_t for the calculation of the *cis*-to-*trans* dihedral barrier crossing time are indicated by dotted vertical lines. (d) Typical dihedral angle simulation trajectories for free and constrained butane for elevated water viscosity $\eta = \sqrt{10}\eta_0$.

which follow by an integral over the memory kernels, are used to predict the transition times of the free and constrained butane scenarios in quantitative agreement with direct simulation results, for this we need to use reaction rate theory that accounts for inertial effects. This shows that our theoretical framework, which simultaneously yields reaction times as well as friction effects, is consistent. Finally, the internal friction contribution is extracted from a fit of the extracted total friction versus the water viscosity: for the constrained butane the internal contribution is negligible, as expected, while for the free butane the internal contribution overwhelms the solvent contribution by a factor of eight, which explains why the butane dihedral reaction is rather insusceptible to an increase of the water viscosity.

We unambiguously show that the dihedral angle dynamics of a butane molecule is dominated by internal friction, which stems from the coupled dynamics of the four carbons. This demonstrates that internal friction exists already for the simplest molecular system that possesses a conformational transition, in line with previous works where dihedral angle isomerization has been argued to be a source of internal friction in protein folding [25, 119, 121–124].

5.1. Results and Discussion

5.1.1. Butane Dihedral Barrier Crossing Times

In our simulations we place a single butane in a water box and systematically vary the mass of water molecules m_{w} while keeping the butane mass fixed. This modifies all intrinsic water timescales and in particular also the water viscosity according to $\eta \propto \sqrt{m_{\mathrm{w}}}$, but leaves all equilibrium distribution functions invariant [241]. We use a united-atom force field for butane that neglects the hydrogens and approximates butane by four Lennard-Jones beads that are subject to fixed bond lengths and fixed bond angles, for water we use the SPC/E model (see Methods). We compare the free scenario, where all four butane carbons can move, with the constrained scenario, where three carbons are fixed in space and only one terminal carbon can rotate, see Fig. 5.1(a) and (b) for an illustration. The only degree of freedom in the constrained scenario is the dihedral angle, while in the free scenario one has six additional degrees of freedom, three translational and three orientational. The free energy profiles in the free and constrained scenarios in Fig. 5.1(c) perfectly overlap, as expected based on translational and orientational invariance of the problem.

The mean first-passage times τ_{MFP} for the *cis*-to-*trans* transition of the dihedral, as defined in Fig. 5.1(c) and extracted from the simulation trajectories as shown in Fig. 5.1(d), are depicted as a function of the rescaled water viscosity η/η_0 in Fig. 5.2 for the free and constrained scenarios. Here η_0 denotes the bulk viscosity of water with the normal mass. τ_{MFP} for free butane is rather insensitive to η, in agreement with previous results [120]. Constrained butane behaves differently for $\eta > \eta_0$ and shows a linear increase of τ_{MFP} with η (indicated by a broken straight line), while for $\eta < \eta_0$ the results for the free and constrained scenarios are rather similar and depend only

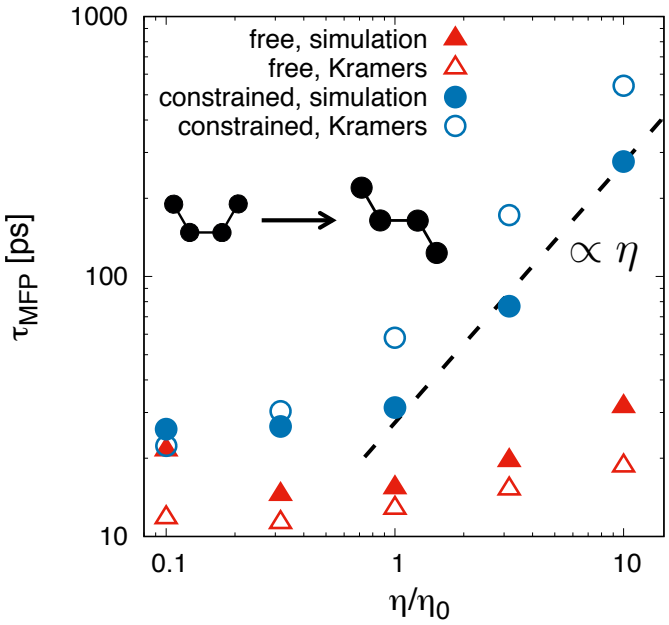

Figure 5.2.: Mean first passage times τ_{MFP} of the *cis*-to-*trans* transition of the butane dihedral for free (triangles) and constrained (circles) butane extracted from simulation trajectories (filled symbols) are shown as a function of the rescaled water viscosity η/η_0, where η_0 refers to the SPC/E water viscosity. The estimates based on the Kramers formula for medium to strong friction Eq. (5.5) are included as open symbols.

weakly on η, which will later be explained by inertial effects (i.e. Kramers turnover). The stark deviation between the free and constrained scenarios for $\eta > \eta_0$, amounting to a difference in the reaction times by a factor of ten for the highest viscosity $\eta = 10\eta_0$, is caused by the six additional degrees of freedom for free butane that are orthogonal to the dihedral angle coordinate. Since the dihedral free energy is the same for both scenarios, we conclude that the friction is different in the two scenarios and that this friction difference is caused by the additional degrees of freedom that are present in the free scenario and absent in the constrained scenario. We will later show that the difference in the total friction between the free and constrained scenarios is accompanied by an internal friction contribution for the free case.

5.1.2. Memory Kernels and Friction Coefficients

To quantify the friction that acts on the dihedral angle, we map the dynamics of the butane dihedral angle x onto the generalized Langevin equation (GLE)

$$m\ddot{x}(t) = -\int_0^t dt'\,\Gamma(t')\dot{x}(t-t') - \nabla U[x(t)] + F_R(t), \tag{5.1}$$

where $\Gamma(t)$ denotes the memory kernel. The random force $F_R(t)$ obeys the fluctuation-dissipation theorem and satisfies $\langle F_R(t)F_R(t')\rangle = k_\mathrm{B}T\,\Gamma\,(t-t')$. For vanishing potential, the GLE has been derived by linear projection techniques [56, 60]. The mass m is an effective one and follows directly from the simulated dihedral angle trajectory $x(t)$ via the equipartition theorem $m\langle\dot{x}^2\rangle = k_\mathrm{B}T$ (see Methods). The potential $U(x)$ in the GLE is in fact a free energy and follows from the simulated equilibrium probability density along the reaction coordinate, $p(x)$, as $U(x) = -k_\mathrm{B}T\log p(x)$ and is shown in Fig. 5.1(c). To extract $\Gamma(t)$ from simulation trajectories we extend previous methods [9, 61, 73] to account for a finite potential $U(x)$. For this we multiply Eq. (5.1) by $\dot{x}(0)$ and average to obtain

$$m\,\langle\dot{x}(0)\ddot{x}(t)\rangle = -\int_0^t dt'\,\Gamma(t')\,\langle\dot{x}(0)\dot{x}(t-t')\rangle - \langle\dot{x}(0)\nabla U[x(t)]\rangle\,, \tag{5.2}$$

where we used that the random force is not correlated with the initial velocity, i.e. $\langle\dot{x}(0)F_R(t)\rangle = 0$ [60]. Discretizing all functions as $\Gamma_i = \Gamma(i\Delta t)$ with a timestep Δt we obtain the iteration equation

$$\Gamma_i = -\frac{1}{\omega_{i,i}\Delta t C_0^{\dot{x}\dot{x}}}\left(\sum_{j=0}^{i-1}\omega_{i,j}\Delta t\Gamma_j C_{i-j}^{\dot{x}\dot{x}} + mC_i^{\dot{x}\ddot{x}} + C_i^{\dot{x}\nabla U}\right), \tag{5.3}$$

where we defined the correlation function $C_i^{\dot{x}\ddot{x}} = \langle\dot{x}(0)\ddot{x}(i\Delta t)\rangle$ (and similarly $C_i^{\dot{x}\dot{x}}$ and $C_i^{\dot{x}\nabla U}$) and the integration weight $w_{i,j} = 1 - \delta_{i,0}/2 - \delta_{i,j}/2$. The correlation function $C_i^{\dot{x}\nabla U} = \langle\dot{x}(0)\nabla U[x(i\Delta t)]\rangle$ is obtained by cubic spline interpolation of $U(x)$. In the Appendix D we demonstrate the numerical robustness of our method.

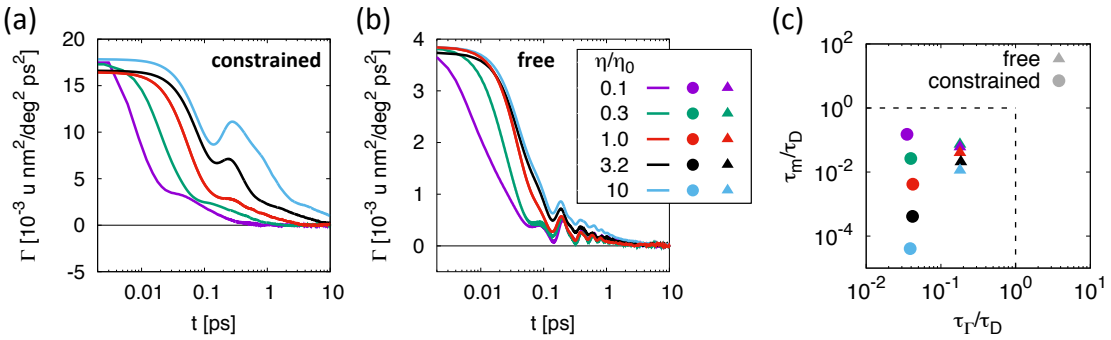

Figure 5.3.: Memory kernels $\Gamma(t)$ for different rescaled water viscosities η/η_0 extracted from simulation trajectories via Eq. (5.3) for (a) constrained and (b) free butane, where η_0 denotes the SPC/E water viscosity. (c) Inertial and memory timescale ratios τ_m/τ_D and τ_Γ/τ_D calculated from the memory kernels of free and constrained butane for different viscosities, where τ_D denotes the characteristic diffusion time (same color coding as in (b)).

The extracted memory kernels $\Gamma(t)$ for free butane in Fig. 5.3(b) are quite similar for different water viscosities, while for constrained butane the kernels in Fig. 5.3(a) differ strongly for different viscosities. In particular, for free butane the long time tail of $\Gamma(t)$, which is mostly responsible for the effective friction, is almost independent of η and oscillations appear that we associate with the presence of orthogonal degrees of freedom. In qualitative accordance with our results in Fig. 5.2 for the barrier crossing time, we can say that for free butane, the effective friction is less sensitive to solvent viscosity compared to constrained butane.

In Fig. 5.4, we show the friction coefficient γ for free and constrained butane as a function of water viscosity, which follows from an integral over the memory function according to $\gamma = \int_0^\infty dt\, \Gamma(t)$. For numerical integration, we fit the long time decay of $\Gamma(t)$ by an exponential function (see Appendix D). The friction for constrained butane is linearly proportional to the solvent viscosity, as expected based on the hydrodynamic Stokes equation. To make this more explicit, we denote the translational friction coefficient of a methyl group by $\gamma_{\text{trans}} = 6\pi\eta R_{\text{CH}_3}$. For a methyl group of radius $R_{\text{CH}_3} \approx 0.18\,\text{nm}$ that rotates at a fixed bond angle $\alpha = 111°$ and C–C bond length $l_\text{B} = 0.15\,\text{nm}$ around a fixed point in space, which approximates the constrained butane case, we estimate the dihedral friction constant $\gamma = (2\pi/360)^2 (l_\text{B} \sin(\alpha))^2 \gamma_{\text{trans}} = 0.01 \cdot (\eta/\eta_0)\,\text{u}\,\text{nm}^2/\text{deg}^2\,\text{ps}$, not so different from what we extract from the simulations in Fig. 5.4 for constrained butane. In contrast, the dynamics of free butane is characterized by a friction coefficient that very weakly depends on the water viscosity, in stark contrast to the hydrodynamic Stokes equation.

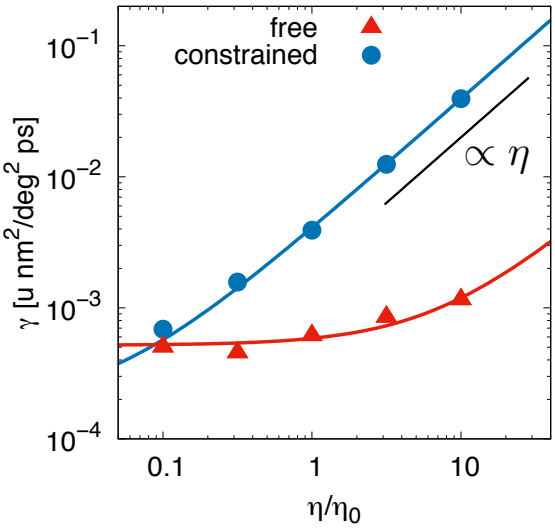

Figure 5.4.: Friction coefficient γ extracted from the memory kernels in Fig. 5.3(a) and (b) as a function of the rescaled water viscosity η/η_0 for free and constrained butane. Empirical fits according to Eq. (5.4) (denoted by lines) yield internal-to-solvent friction ratios of $\gamma_{\text{int}}/\gamma_{\text{sol},0} = 7.7$ for free and $\gamma_{\text{int}}/\gamma_{\text{sol},0} = 0.05$ for constrained butane.

5.1.3. Internal Versus Solvent Friction

We include empirical fits according to [10, 25, 28]

$$\gamma = (\eta/\eta_0)\,\gamma_{\text{sol},0} + \gamma_{\text{int}} \tag{5.4}$$

into Fig. 5.4 as solid lines. The fits are very good, which validates the assumption of additive solvent and internal contributions. For constrained butane we obtain $\gamma_{\text{int}} = 1.8 \cdot 10^{-4}\,\text{u}\,\text{nm}^2/\text{deg}^2\,\text{ps}$ and $\gamma_{\text{sol},0} = 3.9 \cdot 10^{-3}\,\text{u}\,\text{nm}^2/\text{deg}^2\,\text{ps}$, which corresponds to a ratio of $\gamma_{\text{int}}/\gamma_{\text{sol},0} = 0.05$ and shows that internal friction is negligible in this case. A small spurious internal friction contribution is in fact expected from the finite difference between the friction coefficient of immobilized and free solutes, as we have demonstrated based on simulations of water-solvated methane in Chapter 4. In contrast, for free butane we find $\gamma_{\text{int}} = 5.2 \cdot 10^{-4}\,\text{u}\,\text{nm}^2/\text{deg}^2\,\text{ps}$ and $\gamma_{\text{sol},0} = 6.7 \cdot 10^{-5}\,\text{u}\,\text{nm}^2/\text{deg}^2\,\text{ps}$, and thus a ratio $\gamma_{\text{int}}/\gamma_{\text{sol},0} = 7.7$. Hence, the dynamics of free butane is dominated by internal friction effects for normal water viscosity η_0. The substantial reduction of the solvent friction contribution $\gamma_{\text{sol},0}$ in the free case compared to the constrained case is at first sight surprising. This reduction can be rationalized by the fact that the dihedral angle for free butane is a relative coordinate that depends on the motion of all four carbons and is governed by a relative diffusion constant that results from the weighted sum of the individual carbon diffusion constants.

It remains to be checked whether the friction coefficients we extract from simulation trajectories in Fig. 5.4 explain the independently measured dihedral barrier crossing

times in Fig. 5.2. This is non-trivial in the present case since, as mentioned earlier, memory and inertia effects invalidate the simple Kramers prediction $\tau_{\mathrm{MFP}} \sim \gamma$. To proceed, it is useful to introduce the characteristic timescales of the system. These are the inertial time $\tau_m = m/\gamma$, which measures the time at which ballistic motion crosses over to diffusive motion, the memory time $\tau_\Gamma = \gamma/\Gamma(0)$, which measures the decay time of the memory kernel, and the diffusive time $\tau_D = L^2\gamma/(k_B T)$, which measures the free-diffusion time to advance over a characteristic angle of $L = 60°$. In Fig. 5.3(c) we demonstrate that $\tau_m < \tau_D$ and $\tau_\Gamma < \tau_D$ holds for all simulation data, in which case Kramers' formula for the mean first passage time in the medium to strong friction case [242]

$$\tau_{\mathrm{MFP}} = \frac{2\pi\,\omega_{\mathrm{max}}/\omega_{\mathrm{min}}}{[\gamma^2/4m^2 + \omega_{\mathrm{max}}^2]^{1/2} - \gamma/2m} \exp\left(\frac{\Delta U}{k_{\mathrm{B}}T}\right), \tag{5.5}$$

is expected to be valid. For the barrier height we extract $\Delta U = 3.7\,k_{\mathrm{B}}T$ from the free energy in Fig. 5.1(c), $m\omega_{\mathrm{max}}^2 = 6 \cdot 10^{-3}\,k_{\mathrm{B}}T/\mathrm{deg}^2$ and $m\omega_{\mathrm{min}}^2 = 9 \cdot 10^{-3}\,k_{\mathrm{B}}T/\mathrm{deg}^2$ are the curvatures of the free energy at the maximum and minimum. The results from Eq. (5.5) for free and constrained butane are included as open data points in Fig. 5.2; the comparison with the simulation data, which does not use any adjustable parameter, is quite good. The simulation data in the constrained case show a shorter barrier crossing time than expected based on the Kramers formula, whereas for free butane we see the opposite. Both trends can be explained based on memory effects, since an intermediate memory time $\tau_\Gamma/\tau_D \approx 0.01 - 0.1$ significantly accelerates barrier crossing, while a longer memory time increases the barrier crossing time, as has been shown recently in Ref. [vi]. Thus, our results for constrained butane presumably correspond to the regime where memory reduces the reaction time, while the results for free butane (which have slightly larger values of τ_Γ/τ_D, as shown in Fig. 5.3(c)) correspond to the crossover regime where the memory effect switches from acceleration to slowing down of the reaction time. The saturation of τ_{MFP} for the constrained case in the low-viscosity limit in Fig. 5.2 is thereby shown to be solely due to inertia effects and thus reflects Kramers turnover, this follows from the fact that the friction γ for the constrained case in Fig. 5.4 is roughly linear in η over the entire range of water viscosities. In contrast, the behavior of τ_{MFP} for the free case can only be explained by a combination of inertia and internal friction effects. This shows that the present simulation strategy, which compares the free and constrained scenarios and at the same time extracts memory functions, is necessary and useful.

5.2. Conclusions

The dihedral barrier-crossing dynamics of a constrained butane molecule, where only one carbon atom is allowed to move and thus the dihedral angle is the only degree of freedom (besides solvent degrees of freedom) is shown to be very different from the dynamics of a free butane, where a total of seven positional degrees of freedom are present. This unambiguously demonstrates that friction generated by degrees of

freedom that are coupled but orthogonal to the reaction coordinate (in our case the dihedral angle) is dominant in butane. By monitoring the friction, which we directly extract from the memory kernel, as a function of the solvent viscosity, we show that orthogonal degrees of freedom significantly modify the solvent friction contribution and also produce an additional contribution which we denote, in analogy to experiments on protein folding, as internal friction. The internal friction contribution in butane thus stems from the dynamic partitioning of energy over the orthogonal degrees of freedom (which in addition to the six positional also include six conjugate momentum degrees of freedom).

Based on our finding that already for butane, which arguably is a very simple system for which the orthogonal degrees of freedom in fact correspond to the translational and orientational degrees of freedom, internal friction dominates the dynamics, we expect that for larger and more complex molecules, which possess more orthogonal degrees of freedom, internal friction plays an even more important role for the dynamics. For macromolecular conformational transitions where the rate-limiting step involves dihedral angle isomerization [22, 117, 119, 246, 254], our findings constitute one mechanism for the emergence of internal friction effects. But other mechanisms, for example based on interactions between molecular subunits, certainly also exist.

Beyond these applications to polymers and proteins, dihedral isomerization of butane is also interesting in its own right and has been studied by two-dimensional infrared spectroscopy [251]. The experimental dihedral isomerization time of a butane derivative solvated in CCl_4 was found to be in the 10 ps range, which agrees with predictions from classical MD simulations [248] and is similar to the simulation results we obtain here. Our analysis thus reveals that in such experiments the internal friction, which for normal water viscosity makes up about 89% of the total friction, dominates the dynamics, a fact that does not transpire from the simulations per se.

It seems difficult to derive the empirical Eq. (5.4), according to which internal and solvent contributions, the latter being defined as the contribution that scales linearly with solvent viscosity η, are additive, from first principles. We note that according to the fluctuation-dissipation theorem the friction coefficient follows from the force autocorrelation function (see Chapter 3); a decomposition of the force acting on a reaction coordinate into solute and solvent contributions (which is exactly possible) would necessarily give rise to a solvent, a solute and a mixed solute-solvent contribution, and the linear additivity in Eq. (5.4) is not obvious. The good comparison between Eq. (5.4) and the simulation data in Fig. 5.4 validates the linear additivity thus only in a heuristic sense, and could break down for more complicated systems.

5.3. Methods

All simulations are carried out using the GROMACS 5.1 [189, 190] simulation package with double precision. The butane molecule is parametrized by the GROMOS [191] united atom force field, for water we use the SPC/E [192] model. All angles and bonds

of water and butane are constrained to their equilibrium values using the SHAKE [255] algorithm. Real butane possesses additional degrees of freedom that we neglect in our classical simulations, namely bond angle and bond length vibrations of carbon-carbon as well as carbon-hydrogen bonds. However, they are not expected to contribute significantly to the dynamics due to the high quantum-mechanical excitation energies for carbon-carbon bonds and due to the relatively small effective mass of carbon-hydrogen bonds. We perform NVT molecular dynamics (MD) simulations and vary the water molecule mass m_w in order to change the water viscosity. For water mass larger than or equal to the normal water mass, we use a time step of 2 fs, for lighter water mass we lower the timestep by a factor $\eta/\eta_0 \propto \sqrt{m_\mathrm{w}}$. The temperature is controlled by the velocity rescaling [193] thermostat at $T = 300\,\mathrm{K}$, which is coupled only to the solvent with a time constant of $\eta/\eta_0 \cdot 1\,\mathrm{ps}$. In the Appendix D we compare results for the memory kernels calculated from NVT and NVE simulations of a free butane molecule at a water viscosity of $\eta/\eta_0 = \sqrt{10}$ and demonstrate that the ensemble and thus the thermostat have no influence on our results.

The equipartition theorem dictates $m\langle\dot{x}^2\rangle = k_\mathrm{B}T$, which is used to extract the effective mass m from the simulated dihedral angle trajectories $x(t)$. For constrained butane, we find values between $m = 0.92 \cdot 10^{-4}\,\mathrm{u\,nm^2/deg^2}$ and $m = 1.03 \cdot 10^{-4}\,\mathrm{u\,nm^2/deg^2}$, which agree with the expected value for the moment of inertia of a single methyl group of mass $m_{\mathrm{CH_3}} = 15\,\mathrm{u}$ that rotates with a fixed bond angle $\alpha = 111°$ and C–C bond length $l_\mathrm{B} = 0.15\,\mathrm{nm}$ around a fixed pivot point, which leads to $m_\mathrm{I} = m_{\mathrm{CH_3}}(l_\mathrm{B}\sin(\alpha))^2(2\pi/360)^2 = 0.93 \cdot 10^{-5}\,\mathrm{u\,nm^2/deg^2}$. For free butane we obtain smaller effective masses between $m = 2.13 \cdot 10^{-5}\,\mathrm{u\,nm^2/deg^2}$ and $m = 2.18 \cdot 10^{-5}\,\mathrm{u\,nm^2/deg^2}$, as expected for the effective mass that describes a relative coordinate.

Chapter 6

Transition Paths Are Hot

Bibliographic information: Parts of this chapter and of Appendix E have previously been published. Reprinted with permission from Ref. [v]. Copyright: Europhysics Letters Association, 2016.

The bottleneck of biophysical and chemical reactions are the rare but fast barrier crossing events, which receive steadily increasing theoretical attention [49, 256, 257]. A useful concept in this context is the notion of transition paths that connect the initial state x_A to the target state x_B without returning back to the origin, see Fig. 6.1(a) for an illustration. By advanced single-molecule experiments, studies of transition paths and estimates of transition path times were possible for conformational transitions of proteins [258–261] and nucleic acid molecules [262, 263]. In fact, in the context of protein folding, transition paths are considered to constitute the most important part of the trajectories, since they entail complete information on the folding mechanism [260].

Typical experimental observations project the dynamics of a system onto a one-dimensional reaction coordinate, for example the distance between two fluorescent dyes. Motivated by this, one-dimensional stochastic models play a crucial role to analyze and interpret experimental data [260, 261, 263]. Since for molecular reactions in solvent, friction typically dominates over inertia, the overdamped Langevin equation and the equivalent Fokker-Planck equation are prominent models for their theoretical description. In this framework, a closed-form expression for the mean transition path time has been derived by Szabo [256, 264] and been used to interpret experimental measurements of transition path times [259–261] as well as to predict transition path times of protein and nucleic acid folding from experimentally determined free energy landscapes [265, 266].

In contrast, many chemical reactions occur in the low-friction regime, even when immersed in solvent, and are dominated by inertia effects so that the overdamped Fokker-Planck description is not valid [267]. This has experimentally been demonstrated for isomerization and dissociation reactions using pico-second resolved spectroscopy

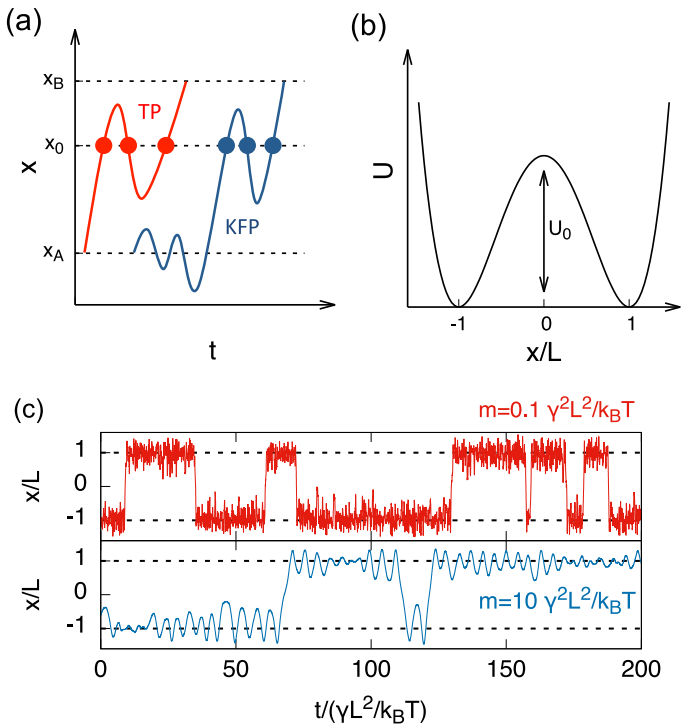

Figure 6.1.: (a) Schematic visualization of a transition path (TP) and a Kramers first passage path (KFP) from x_A to x_B. Mean shapes of paths result from averaging the times of all crossing events at x_0 (denoted by circles). (b) The quartic potential used as a model for a typical two state system. (c) Simulated trajectories for masses $m = 0.1\,\gamma^2 L^2/k_\mathrm{B}T$ and $m = 10\,\gamma^2 L^2/k_\mathrm{B}T$ for a barrier height of $U_0 = 3\,k_\mathrm{B}T$.

techniques [268, 269]. Since transition path times are typically a few orders of magnitude shorter than mean reaction times [259–261], it seems plausible that inertia effects play an even more important role for correctly predicting transition path times than for reaction times. In fact, the mean transition path time for a harmonic barrier was recently calculated in the asymptotic frictionless limit based on conservative dynamics and shown to behave drastically different from the overdamped result [270]. Note that in the context of polymer and protein dynamics, theoretical findings suggest that solvent memory effects also affect the short time dynamics [120, 248, 253], which however is not treated in this chapter.

Here, we consider transition paths in a quartic double-well potential and study the full crossover between the friction to the inertia dominated regimes using Brownian dynamics simulations as well as asymptotic analysis. We show that the ensemble of transition paths exhibits significant deviations from the equilibrium velocity distribution. The effective temperature of transition paths, $T_{\mathrm{eff}}^{\mathrm{TP}}$, defined by the second moment of the velocity distribution, is a convenient measure for the departure from equilibrium. We show that transition paths are significantly hotter than the ambient temperature at their initial start position in the potential well for large mass and for high potential barriers. In fact, at the barrier top, transition paths still show significant deviations from equilibrium which surprisingly are most pronounced for intermediate mass. We thus reveal a connection between rare barrier-crossing events and local departure from equilibrium thermodynamics that can be directly tested in experiments and simulations. Since every successful transition event is terminated by a transition path, our results describe a generic feature of thermally activated reactions. We further characterize transition paths by their mean shape, for which we compare simulation results with recent analytic results in the friction and inertia dominated limits.

6.1. Methods

We use the one-dimensional Langevin equation

$$m\ddot{x}(t) = -\gamma\dot{x}(t) - \nabla U[x(t)] + \xi(t), \tag{6.1}$$

with mass m and friction coefficient γ, where the stochastic force $\xi(t)$ obeys $\langle\xi(t)\xi(t')\rangle = 2k_{\mathrm{B}}T\gamma\,\delta(t-t')$. The quartic potential $U(x) = U_0\left((x/L)^2-1\right)^2$ has two minima at $x = \pm L$ and a barrier of height U_0, see Fig. 6.1(b). We investigate three different barrier heights $U_0/k_{\mathrm{B}}T = 1, 3, 5$ and rescaled masses in the range $m/(\gamma^2L^2/k_{\mathrm{B}}T) = 10^{-3} - 10^2$. After rescaling, the continuous problem is fully described by the choice of these two parameters. Note that the rescaled mass $m/(\gamma^2L^2/k_{\mathrm{B}}T)$ is equal to the ratio of the inertial timescale $\tau_m = m/\gamma$ and the diffusive timescale $\tau_D = L^2/D$, where $D = k_{\mathrm{B}}T/\gamma$ denotes the diffusion constant. For our simulations, we discretize time with a typical step width of $\Delta t = 10^{-4}(mL^2/k_{\mathrm{B}}T)^{1/2}$ and use a standard Runge-Kutta scheme of 4th order. Averages are obtained from 400 independent trajectories of $2\cdot10^9$ time steps each where the first 10^7 steps are skipped to ensure equilibration. Two examples of

typical trajectories for different masses are shown in Fig. 6.1(c), it is clearly seen that the curve for larger mass is much smoother and shows fewer transition events.

6.2. Transition Path Times

From the trajectories, we compute mean transition path times $\tau^{\mathrm{TP}}(x_{\mathrm{B}}|x_{\mathrm{A}})$ as well as Kramers mean first passage times $\tau^{\mathrm{KFP}}(x_{\mathrm{B}}|x_{\mathrm{A}})$ from the initial position $x_{\mathrm{A}} = -L$ to the target position $x_{\mathrm{B}} = L$. Note that $\tau^{\mathrm{KFP}}(x_{\mathrm{B}}|x_{\mathrm{A}})$ allows for multiple recrossings of x_{A} and therefore corresponds to the inverse reaction rate one would measure experimentally (see Fig. 6.1(a) for an illustration). The results are collected as a function of m in Fig. 6.2. In contrast to τ^{KFP}, which exponentially increases with the barrier height U_0, τ^{TP} inversely depends on U_0 for all masses m, i.e., transition paths become faster for increasing barrier height. We include as horizontal dashed lines the analytic results in the overdamped limit $m/(\gamma^2 L^2/k_{\mathrm{B}}T) \to 0$ for τ^{KFP} [55, 242]

$$\tau_{\gamma}^{KFP}(x_B|x_A) = \frac{\gamma}{k_{\mathrm{B}}T}\int_{x_A}^{x_B} dy\, e^{\frac{U(y)}{k_{\mathrm{B}}T}} \int_{-\infty}^{y} dz\, e^{-\frac{U(z)}{k_{\mathrm{B}}T}} \tag{6.2}$$

and for the transition path times τ^{TP} [256]

$$\tau_{\gamma}^{TP}(x_B|x_A) = \frac{\gamma}{k_{\mathrm{B}}T}\int_{x_A}^{x_B} dy\, e^{\frac{U(y)}{k_{\mathrm{B}}T}} \int_{x_A}^{x_B} dz\, \frac{\phi_A(z)\phi_B(z)}{e^{\frac{U(z)}{k_{\mathrm{B}}T}}}, \tag{6.3}$$

where $\phi_A(x)$ and $\phi_B(x)$ denote the splitting probabilities

$$\phi_A(x) = 1 - \phi_B(x) = \left(\int_{x_A}^{x_B} dy\, e^{\frac{U(y)}{k_{\mathrm{B}}T}}\right)^{-1} \int_{x}^{x_{\mathrm{B}}} dz\, e^{\frac{U(z)}{k_{\mathrm{B}}T}}. \tag{6.4}$$

The inertial limit $m/(\gamma^2 L^2/k_{\mathrm{B}}T) \to \infty$ corresponds to conservative dynamics, the transition path time follows by a flux-weighted average over the high energy tail ($E > U_0$) of the equilibrium energy distribution at $x = x_{\mathrm{A}}$ as [270]

$$\tau_{m}^{\mathrm{TP}}(x_{\mathrm{B}}|x_{\mathrm{A}}) = \int_{U_0}^{\infty} \frac{dE\, e^{-\frac{E}{k_{\mathrm{B}}T}}}{k_{\mathrm{B}}T e^{-\frac{U_0}{k_{\mathrm{B}}T}}} \int_{x_A}^{x_B} dx \sqrt{\frac{m/2}{E - U(x)}}, \tag{6.5}$$

included in Fig. 6.2 as solid lines.

Obviously, $\tau_m^{TP}(x_{\mathrm{B}}|x_{\mathrm{A}}) \sim m^{1/2}$ in the inertial limit, in contrast to Kramers mean first passage time which scales as $\tau_m^{KFP}(x_{\mathrm{B}}|x_{\mathrm{A}}) \sim m$ in the inertial limit for sufficiently high barriers [242].

As expected, the simulation results for $\tau^{\mathrm{TP}}(x_{\mathrm{B}}|x_{\mathrm{A}})$ smoothly interpolate between the two limits in Eqs. (6.3) and (6.5) and are well described by the linear interpolation formula

$$\tau^{TP}(x_{\mathrm{B}}|x_{\mathrm{A}}) \approx \tau_{\gamma}^{TP}(x_{\mathrm{B}}|x_{\mathrm{A}}) + \tau_{m}^{TP}(x_{\mathrm{B}}|x_{\mathrm{A}}), \tag{6.6}$$

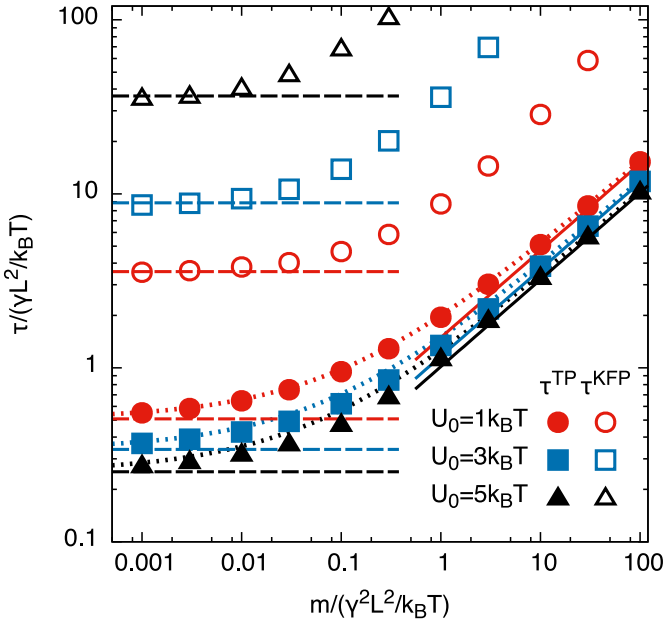

Figure 6.2.: Simulation results for the mean transition path time $\tau^{\mathrm{TP}}(x_{\mathrm{B}}|x_{\mathrm{A}})$ (filled symbols) and Kramers mean first passage time $\tau^{\mathrm{KFP}}(x_{\mathrm{B}}|x_{\mathrm{A}})$ (open symbols) as a function of mass m for three different barrier heights U_0. The analytic overdamped limits Eqs. (6.2) and (6.3) are included as dashed horizontal lines and the inertial limits [270] for $\tau_m^{\mathrm{TP}}(x_{\mathrm{B}}|x_{\mathrm{A}})$, Eq. (6.5), as solid lines. The empirical interpolation according to Eq. (6.6) for the transition path times is shown by dotted lines.

represented as dotted lines in Fig. 6.2. The crossover is located at $m/(\gamma^2 L^2/k_\mathrm{B}T) \approx 0.11, 0.08, 0.06$ for $U_0/k_\mathrm{B}T = 1, 3, 5$ respectively, and thus shifts towards smaller masses with increasing barrier height U_0. As expected, deviations of the transition path times from the overdamped predictions are at small masses around $m/(\gamma^2 L^2/k_\mathrm{B}T) \approx 0.01$ much larger than for the mean first passage times.

6.3. Velocity Distributions and Transition Path Temperatures

The velocity distributions of transition paths at the initial position x_A are shown in Fig. 6.3(a) and (b) for two different masses (red bars). Evidently, they differ substantially from the simulated equilibrium velocity distribution calculated using all paths (i.e. transition paths and paths that return to x_A without reaching x_B), shown as blue circles, which is well described by the expected flux-weighted Maxwell distribution [271]

$$P^\mathrm{eq}(v) \propto |v| \exp\left(-mv^2/2k_\mathrm{B}T\right) \tag{6.7}$$

shown as solid lines. Clearly, transition path velocity distributions at x_A are significantly shifted towards higher velocities and thus higher kinetic energies. To characterize this shift, we introduce the position dependent effective temperature of transition paths via the second moment of velocities evaluated at position x_0,

$$k_\mathrm{B}T_\mathrm{eff}^\mathrm{TP}(x_0) = \frac{1}{2} m \left\langle v^2(x_0)\right\rangle^\mathrm{TP} . \tag{6.8}$$

Note that the factor 1/2 in Eq. (6.8) compared to the position-independent ensemble average stems from the additional factor $|v|$ in the distribution Eq. (6.7) (see Appendix E).

In Fig. 6.3(c), the effective transition path temperature at the initial position is shown to reach multiples of the ambient temperature for higher barrier and large mass. This is intuitively clear, since for small friction, the initial kinetic energy of a transition path has to be large enough to reach the barrier top. Interestingly, for small mass the initial temperature converges to a value of $T_\mathrm{eff}^\mathrm{TP}(x_\mathrm{A})/T \approx 1.3$ independent of barrier height. This can be rationalized by the following approximative argument for a flat potential, i.e. $U(x) = 0$. For times larger than the inertial timescale, $t \gg \tau_m = m/\gamma$, the solution $x(t)$ of the Langevin equation (6.1) with initial conditions $x(0) = x_\mathrm{A}$ and $v(0) = v_0$ obeys $\langle x(t)\rangle = x_\mathrm{A} + mv_0/\gamma$ and $\langle v(t)\rangle = 0$ and the motion becomes purely diffusive. Starting from this position, the probability to exit the interval at x_B is given by the splitting probability calculated according to diffusive dynamics [272], $\phi_\mathrm{B}(v_0) = (\langle x(t)\rangle - x_\mathrm{A})/(x_\mathrm{B} - x_\mathrm{A}) = mv_0/\gamma(x_\mathrm{B} - x_\mathrm{A})$, which obviously depends on the initial velocity v_0. Hence, the overall probability to exit the transition region at x_B, which is the transition path probability itself, is given by the product $P^\mathrm{TP}(v_0) = P^{eq}(v_0)\phi_\mathrm{B}(v_0)$. From this the second moment of the initial velocity of the transition-path ensemble follows as

$$\left\langle v^2(x_\mathrm{A})\right\rangle^\mathrm{TP} = \frac{\int dv\, v^2 P^\mathrm{TP}(v)}{\int dv\, P^\mathrm{TP}(v)} = \frac{3}{2}\left\langle v^2(x_\mathrm{A})\right\rangle \tag{6.9}$$

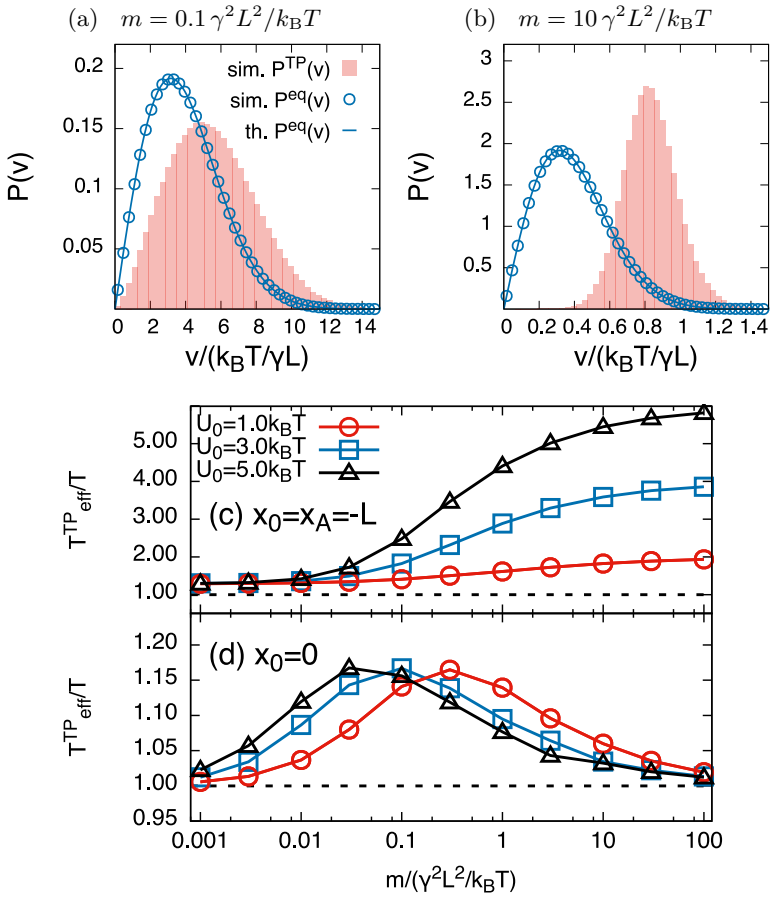

Figure 6.3.: (a) and (b) Velocity distributions of transition paths $P^{\mathrm{TP}}(v)$ (red bars) at the initial position $x_0 = x_A = -L$ compared to the velocity distribution of all paths $P^{\mathrm{eq}}(v)$ (circles) for $U_0 = 3\,k_{\mathrm{B}}T$ and two different masses. The expected equilibrium distribution in Eq. (6.7) is shown as solid lines. (c) Effective transition path temperature $T^{\mathrm{TP}}_{\mathrm{eff}}$ as defined via the second moment of the velocity distribution in Eq. (6.8) at the initial position $x_0 = x_A = -L$ as a function of mass m. (d) $T^{\mathrm{TP}}_{\mathrm{eff}}$ at the barrier top ($x_0 = 0$). The data points are connected by lines to guide the eye.

which is found to be larger than the result for the entire path ensemble by a factor of 3/2 independent of mass. We conclude that $T_{\rm eff}^{\rm TP}(x_{\rm A})/T \approx 3/2$ and thus the velocity distribution is different from the equilibrium one even for $m \to 0$. However, we emphasize that in the over-damped limit the velocity distribution of transition paths quickly relaxes back to the equilibrium one as the paths leave the initial position. A more detailed derivation is given in Appendix E.

In Fig. 6.4, the evolution of $T_{\rm eff}^{\rm TP}(x_0)$ is shown as a function of x_0 along the transition path for $U_0 = 3\,k_{\rm B}T$ and different masses (corresponding plots for $U_0 = 1\,k_{\rm B}T$ and $U_0 = 5\,k_{\rm B}T$ can be found in the Appendix E). For the smallest mass $m = 0.001\,\gamma^2L^2/k_{\rm B}T$, $T_{\rm eff}^{\rm TP}(x_0)$ relaxes down to the equilibrium temperature very quickly. However, already for $m \gtrsim 0.01\,\gamma^2L^2/k_{\rm B}T$, $T_{\rm eff}^{\rm TP}(x_0)$ exhibits significant departures from the ambient temperature throughout the entire spatial region.

In the inertial limit, $m/(\gamma^2L^2/k_{\rm B}T) \to \infty$, the profile of the local transition path temperature can be understood again from conservative dynamics, i.e. by calculating $\langle v^2(x_0)\rangle^{\rm TP}$ from the high energy tail of the flux-weighted Maxwell distribution:

$$\langle v^2(x_0)\rangle^{\rm TP} = \int_{\Delta U}^{\infty} dE\, e^{-\frac{E}{k_{\rm B}T}} v^2(E) \Big/ \int_{\Delta U}^{\infty} dE\, e^{-\frac{E}{k_{\rm B}T}}\ , \tag{6.10}$$

with $\Delta U \equiv U_0 - U(x_0)$ and $v(E) \equiv (2E/m)^{1/2}$. Using Eq. (6.8), we obtain

$$k_{\rm B}T_{\rm eff}^{\rm TP}(x_0) = k_{\rm B}T + U_0 - U(x_0), \tag{6.11}$$

which is shown as a dashed line in Fig. 6.4 and indeed constitutes the upper limit for large mass. Intuitively speaking, the local thermal energy $k_{\rm B}T_{\rm eff}^{\rm TP}(x_0)$ corresponds to the barrier energy minus the local potential energy plus the ambient thermal energy $k_{\rm B}T$. Consequently, the transition path thermal energy at the barrier top never falls below $k_{\rm B}T$, i.e., transition paths are never cooler than the reservoir.

For all masses, $T_{\rm eff}^{\rm TP}(x_0)$ is lowest at the barrier top at $x_0 = 0$, but interestingly for intermediate masses, it is still higher than the equilibrium temperature. $T_{\rm eff}^{\rm TP}(x_0)$ at the barrier top $x_0 = 0$ is shown in Fig. 6.3(d) as a function of mass. We observe a non-monotonic behavior, with a maximum around $m \approx 0.1\,\gamma^2L^2/k_{\rm B}T$ for the energy barriers considered.

6.4. Transition Path Shapes

The ensemble of transition paths can further be characterized by its mean shape, $\tau_{\rm shape}^{\rm TP}(x_0|x_{\rm A})$, defined as the mean time it takes a transition path to reach the point x_0 from the initial position $x_{\rm A}$ before reaching the target state $x_{\rm B}$. In simulations, the mean shape of transition paths is calculated by averaging over all crossing events of the entire transition-path ensemble as indicated in Fig. 6.1(a) by circles. Each crossing event enters with the same weight for the trajectory analysis. In the overdamped limit, this definition turns out to be equivalent to taking only the last crossing event into account, as has been shown recently by an exact calculation [272]. Hence, a transition path

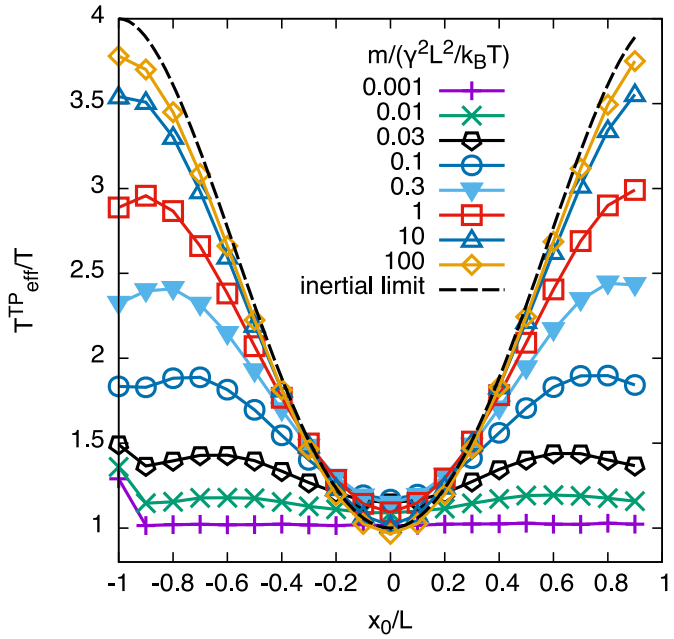

Figure 6.4.: Effective transition path temperature $T_{\mathrm{eff}}^{\mathrm{TP}}$ as a function of position x_0 for fixed barrier height of $U_0 = 3\,k_{\mathrm{B}}T$ and different masses. The data points are connected by solid lines to guide the eye. The inertial limit according to Eq. (6.11) is shown as a dashed line.

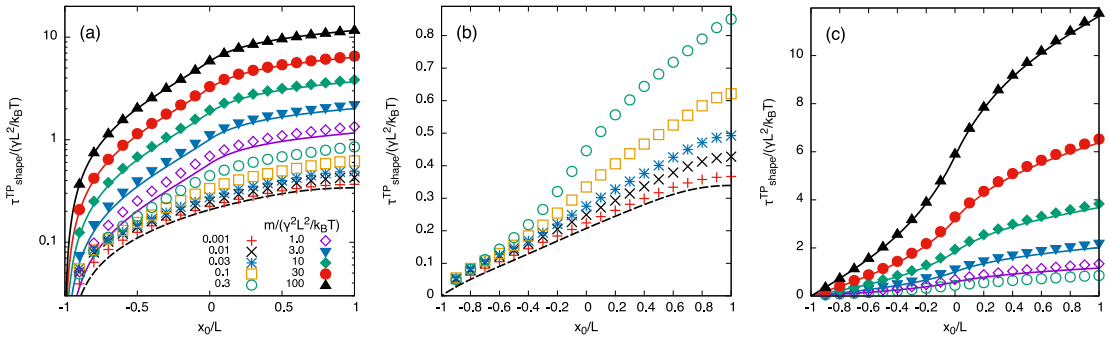

Figure 6.5.: Mean transition path shape $\tau^{\mathrm{TP}}_{\mathrm{shape}}(x_0|x_\mathrm{A})$ for a barrier height of $U_0 = 3\,k_\mathrm{B}T$ as a function of the position x_0 for different masses m in (a) semi-logarithmic and (b/c) linear representation. The overdamped limit Eq. (6.13) is included as a dashed line, the inertial limit Eq. (6.12) is shown as solid lines.

shape is in general time-asymmetric, i.e. $\tau^{\mathrm{TP}}_{\mathrm{shape}}(x_0|x_\mathrm{A}) \neq \tau^{\mathrm{TP}}_{\mathrm{shape}}(x_B|x_\mathrm{A}) - \tau^{\mathrm{TP}}_{\mathrm{shape}}(x_0|x_\mathrm{B})$, which reflects the diffusive character of transition paths. In contrast, the shape of transition paths with only one crossing event, as realized by conservative dynamics in the inertial limit, are time symmetric, as will be demonstrated below. The simulation results are shown in Fig. 6.5 for a barrier height of $U_0 = 3\,k_\mathrm{B}T$ (corresponding results for $U_0 = 1\,k_\mathrm{B}T$ and $U_0 = 5\,k_\mathrm{B}T$ can be found in Appendix E).

In the inertial limit, $m/(\gamma^2L^2/k_\mathrm{B}T) \to \infty$, the transition path shape $\tau^{\mathrm{TP}}_{\mathrm{shape}}(x_0|x_\mathrm{A})$ is simply given by the time it takes the deterministic transition path to go from the initial position x_A to the intermediate position x_0, we thus obtain

$$\tau^{\mathrm{TP}}_{\mathrm{shape},m}(x_0|x_\mathrm{A}) = \tau^{\mathrm{TP}}_{m}(x_0|x_\mathrm{A}) \tag{6.12}$$

with $\tau^{\mathrm{TP}}_{m}(x_0|x_\mathrm{A})$ given by Eq. (6.5). Indeed, for $m/(\gamma^2L^2/k_\mathrm{B}T) \geq 1$ the analytic result according to Eq. (6.12), shown in Fig. 6.5 as solid lines, describes the simulated shapes very well. In particular, the above-mentioned time symmetry of transition paths with $m/(\gamma^2L^2/k_\mathrm{B}T) \gg 1$ is clearly seen in the linear plot in Fig. 6.5(c). In the overdamped limit, on the other hand, the mean shape of a transition path can be expressed as [272]

$$\tau^{\mathrm{TP}}_{\mathrm{shape},\gamma}(x_0|x_\mathrm{A}) = \tau^{\mathrm{TP}}_{\gamma}(x_\mathrm{B}|x_\mathrm{A}) - \tau^{\mathrm{TP}}_{\gamma}(x_\mathrm{B}|x_0), \tag{6.13}$$

with $\tau^{\mathrm{TP}}_{\gamma}(x_0|x_\mathrm{A})$ given by Eq. (6.3). This result, which is shown in Fig. 6.5 as a broken line, describes the simulation data for small masses very well. The time-asymmetry of transition paths with $m/(\gamma^2L^2/k_\mathrm{B}T) \ll 1$ is clearly seen in the linear plot in Fig. 6.5(b). Obviously, the analytic limits Eqs. (6.12) and (6.13) constitute upper and lower limits of the simulation data. We conclude that although the effective temperature of transition paths is significantly increased for large mass, the effect on the mean shapes is less obvious.

6.5. Conclusions

Our work demonstrates that the ensemble of transition paths does not obey thermodynamic local equilibrium and is rather characterized by a local effective temperature that is considerably higher than the ambient temperature, in particular for large mass and high barriers. Hence, as one intuitively would expect, the ensemble of transition paths corresponds to a subset of heated trajectories. This is the case because the transition path time is typically much shorter than the mean first passage time, which makes transition paths more susceptible to short-time inertial effects. We show that the main parameter controlling the departure from equilibrium besides the barrier height is the rescaled mass $m/(\gamma^2 L^2/k_\mathrm{B}T) = \tau_m/\tau_D$, which can be expressed as the ratio of the inertial timescale $\tau_m = m/\gamma$ and the diffusive timescale $\tau_D = L^2/D$. Thus, the non-equilibrium effects we are predicting are observable whenever the mass m is large, the friction coupling γ to the solvent is weak, or when the spatial extend L of the transition region is small. This applies in particular to ultra-fast molecular kinetics that were previously demonstrated to be inertial rather than overdamped [267–269]. Alternatively, our predictions could be tested by direct experimental observations of colloidal dynamics [273–275]. For a colloid of radius R, the Stokes friction obeys $\gamma \propto R$, whereas the mass scales as $m \propto R^3$, we therefore find for the rescaled mass $m/(\gamma^2 L^2/k_\mathrm{B}T) \propto R/L^2$. Hence, one would have to tailor experimental systems with sufficiently short barrier length L compared to the colloid radius R to observe significant influence of inertia. Even in rather damped systems with $m \approx 0.01\,\gamma^2 L^2/k_\mathrm{B}T$, significant departures from equilibrium are observed along the full path, while for sufficiently high damping with $m \lesssim 0.001\,\gamma^2 L^2/k_\mathrm{B}T$, non-equilibrium effects are only observed for the initial segment of transition paths.

For more complex systems with many conformational degrees of freedom, it remains to be investigated how the effective temperature of orthogonal degrees of freedom is determined by the coupling to the reaction coordinate. In the context of transition path sampling techniques, our results might be helpful for designing efficient biased shooting move distributions and thereby improve the performance [49, 276].

Chapter 7

Summary, Conclusions and Outlook

In the present thesis, several fundamental and previously unknown properties of molecular friction and dynamics have been revealed by new theoretical approaches, which combine molecular dynamics simulations with stochastic and analytical models. The experimental relevance of dichroic infrared continuum bands to determine the orientation of non-spherical protonated water clusters has been identified. We have demonstrated for the first time that the friction constant of a small molecule in water depends on the confinement strength, and the mass dependence of molecular aqueous friction has been characterized including the massless and infinite mass limits. The long-known insensitivity of the dihedral angle isomerization rate, a crucial reaction in polymer dynamics and protein folding, has been shown to be due to internal friction of the dihedral angle itself, in contrast to speculations from the literature. Furthermore, we have found that the velocity distributions of transition paths deviate significantly from the equilibrium distribution.

In Chapter 2, infrared spectra for protonated and unprotonated water chains, discs and droplets have been calculated from ab initio molecular dynamics trajectories. In the presence of an excess proton, we have obtained a pronounced infrared continuum band over a broad frequency range for all three water cluster geometries. This continuum band exhibits significant anisotropy for chains and discs with the infrared absorption being maximal when the infrared light is polarized along the direction of maximal extension of the water cluster. The local spectral analysis of the protonated water chain has shown that the continuum band arises from polarization fluctuations of the excess proton, which is predominantly observed in a Zundel complex as it moves axially along the chain, whereas the electronic polarizability gives rise to a moderate, but long-ranged amplification of the polarization fluctuations. These results have been used to conclude from experimental polarization-resolved infrared spectra (recorded by Mattia Saita under supervision of Prof. Dr. Joachim Heberle at the Freie Unversität Berlin) that the protonated water cluster responsible for the continuum band of the proton-pumping protein bacteriorhodopsin is oriented perpendicularly to the proton

pumping direction. This demonstrates the potential of polarization-resolved infrared absorption spectroscopy as a tool to probe the geometry and orientation of protonated water clusters in proteins.

These findings are particularly relevant, because proton transfer processes are a part of all essential biological metabolic pathways and many technological applications such as fuel cells and electrochemical devices [18–20]. Water is a crucial ingredient in such processes, since it solvates (and thus stabilizes) the proton and furthermore mediates fast proton transfer reactions. In fact, all proton-conducting proteins contain embedded water clusters and water chains [112, 125–127], which are therefore believed to play an active role. Owing to the small size of the proton and its highly dynamic nature, the precise mechanisms by which water clusters direct proton transport is still intensely debated. Since excess protons give rise to the characteristic broad infrared continuum bands [128, 132], infrared spectroscopy has been instrumental for our understanding of the protonation dynamics in proteins. Our findings show that polarization-resolved infrared spectroscopy in conjunction with ab initio simulations has the potential to unravel the proton transport mechanism in anisotropic systems. The only experimental condition is that oriented samples can be prepared, which however is possible for most proton-conducting proteins [165–169], for proton-conducting synthetic membranes [172] and also other meso-structured materials that contain protons, such as hexagonal and lamellar lipid phases [170, 171]. Therefore, we envision polarization-resolved infrared spectroscopy to become an important tool for the study of proton transport.

Using a novel method to extract the friction memory function from molecular dynamics simulations, we have shown in Chapter 3 that the solvent friction of a strongly, harmonically confined methane molecule in water increases by 60% compared to its free-solution value, which is caused by an amplification of the slowest component of the memory function. The friction enhancement occurs for potential strengths typical of physical and chemical bonds and is accompanied by a significant slowing down of the hydration water dynamics. Thus, the solvent friction acting on molecular solutes is not determined by solvent properties and solute-solvent interactions alone but results from the coupling between solute and solvent dynamics and thereby can be tuned by an external potential acting on the solute. The dynamic scaling arguments we have presented in this thesis suggest the existence of similar effects also for macromolecular solutes provided that the solution viscosity is sufficiently enhanced.

Our analysis shows that Stokes' prediction for the friction coefficient of a sphere, a cornerstone of hydrodynamics, is incomplete on the molecular scale since it neglects the coupling between solute and solvent motion, an effect that clearly goes beyond hydrodynamic theory. In all previous theoretical and experimental works it has been tacitly assumed that the friction coefficient of a molecule does not depend on whether the molecule is bound to a second molecule, in other words, whether its motion is confined in an external potential. We have shown that this assumption is wrong and that the friction coefficient of a methane molecule in water sensitively depends on the strength K of an external harmonic confining potential and that this dependence is

quite sizeable, and occurs in a range of K that is in between weak physical bonds (such as van-der-Waals bonds) and covalent bonds. It is thus relevant for many experimental molecular systems. Apart from the basic scientific interest, these results constitute a direct explanation of the experimental finding that the hydration shell dynamics around a protein depends on protein flexibility [215] as well as on its local structural rigidity [212]. The results also explain previous simulation results for the friction coefficient of frozen (i.e. infinite mass) ions in water, which have shown significant deviations from the friction of freely diffusing ions [199]. More generally, the coupling between the motion of molecular solutes and the dynamics of the hydration shell is a key question in biophysics and has been studied experimentally by various techniques [180, 181, 203, 210–216]. Clearly, our results may play a role for future interpretations of such experiments.

Motivated by these findings, we have shown in Chapter 4 that the friction constant of a freely diffusing methane molecule in explicit water depends on the mass of the molecule, ranging from 0.9 times the physical methane friction in the massless limit to about 1.6 times the physical value in the infinite mass limit. We have explained the molecular origin of this effect by employing a generalized Langevin model, and extracted the mass dependence of the solvent memory kernel. We have demonstrated that only with the mass-dependent memory kernels one obtains perfect agreement between simulation results and analytic predictions for both mean-square displacements and force autocorrelation functions. The memory kernels, which describe the solvent degrees of freedom, decay significantly slower with increasing solute mass. As a microscopic interpretation, we have shown that the mean escape time of water molecules from the first hydration shell increases monotonically with solute mass by up to a factor of three over the solute mass range considered. Our results allow a direct prediction of diffusion constants for physical methane isotopes, and our scaling analysis suggests that mass-dependent friction will be relevant also for larger solutes, in particular in highly viscous solvents.

Mass-dependent diffusion can be directly measured [209, 234] and the isotope ratios of noble gases play a role for the investigation of groundwater in geochemistry because of this effect [223–228]. And indeed, in a similar fashion, our predicted diffusion constant ratios for methane isotopes may help to better understand bacterial methane isotope fractionation [238–240]. However, our main result is the characterization of this effect over the complete relevant mass range including the limits of a massless and an infinitely heavy particle, with an additional discussion of scaling arguments for larger solutes. Therefore, our findings allow to estimate the relevance and magnitude of mass-dependent friction for a variety of systems.

The mass and confinement dependence of the friction share a common feature: the heavier and more confined particles respond less to the water molecules, which in both cases leads to an increase of the molecular friction. This suggests that a friction increase and a slowing down of hydration shell dynamics as a consequence of a reduced response to solvent motion is a universal, previously not recognized pattern on the molecular scale.

By analysis of the dihedral friction of water-solvated butane for varying water viscosity, we have demonstrated the existence of an internal friction contribution in Chapter 5. This has been made possible by a newly developed method to extract the friction memory function directly from simulations in the presence of an arbitrary free-energy landscape. At normal water viscosity the internal friction has turned out to be eight times larger than the solvent friction and it thus completely dominates the effective friction. By comparison with simulations of a constrained butane molecule that has the dihedral as the only degree of freedom, we have demonstrated that internal friction comes from the six additional degrees of freedom in unconstrained butane that are orthogonal to the dihedral angle reaction coordinate. While the insensitivity of butane's dihedral dynamics to the water viscosity is solely due to the presence of internal friction, inertial effects crucially influence the resultant dihedral barrier crossing rates. In contrast, non-Markovian effects due to the finite memory time are present but do not significantly influence the dihedral barrier crossing rate of butane. These results not only answer the question about the character of dihedral dynamics in small molecular systems such as butane, they also have important implications for the folding of polymers and proteins.

This is particularly relevant, since in the field of polymer dynamics and protein folding, the existence of internal friction is intensely and controversially discussed [8, 10, 11, 25–29, 52, 117, 119–122, 241, 243–246]. The dihedral angle dynamics of butane plays a paradigmatic role in this debate, because it is the minimal system that shows a conformational transition. The known insensitivity of the dihedral angle isomerization rate to the solvent viscosity has been argued to be related to internal friction in protein folding [25, 119, 121–124], but the microscopic mechanism behind the dihedral kinetics has remained unclear. All previous experimental and theoretical studies have estimated internal friction rather indirectly from reaction times [119–122, 241], which introduces substantial uncertainties since many factors besides friction influence reaction times. The new method used in this thesis allows to directly extract the friction memory kernel for a reaction coordinate in a free-energy landscape from simulation trajectories. This advancement has enabled us to quantify the internal friction contribution to the total friction, and thus, to settle this long-lasting question. Our results imply that internal friction will influence the folding dynamics whenever dihedral angle isomerizations constitute rate-limiting steps. Therefore, internal friction will arise naturally for almost all complex molecules in solvent. Furthermore, they demonstrate that the hydrodynamic estimate for the effective friction of conformational transitions fails even for the simplest possible case.

In the last part of this thesis, in Chapter 6, transition paths in a one-dimensional double-well potential have been studied by Brownian dynamics simulations. For large mass and high barrier the velocity distribution of transition paths has been found to deviate significantly from the equilibrium Maxwell distribution, and their effective temperature at the initial position in the potential well has been shown to reach many times the ambient temperature. The effective transition path temperature at the barrier

top is only slightly increased and has turned out to be maximal at intermediate values of the mass. An analytic expression for the temperature evolution along a transition path in the high-mass limit has been derived.

The result that transition paths are significantly hotter than ambient temperature, where the temperature increase depends on the ratio of particle mass and friction coefficient, constitutes a crucial step towards a complete theoretical understanding of transition paths. In particular, this result provides the link between stochastic and thermodynamic properties of the transition path ensemble. In addition to the importance of the transition path concept for any two-state reaction, the findings can be confronted with single-molecule experimental observations [258–263].

For these reasons, the present thesis constitutes an essential step towards a complete understanding of dynamic molecular processes in aqueous solutions, and it sheds light on the complex and subtle interplay of friction, inertial and non-Markovian effects on the molecular scale. In fact, several of the new findings have a very fundamental and basic character.

Thus, they motivate a variety of prospective projects, in particular, they raise the question how the revealed mechanisms influence more complex systems. Moreover, the successful application of the newly developed methods hints at their potential to understand additional dynamic processes. In the following, we present a list of research perspectives based on the results of the present thesis.

Stochastic description of proton motion. A promising follow-up project that combines several ideas from this thesis is the stochastic description of the center of charge motion in a linear protonated water chain, but also possibly in other protonated water clusters, via a generalized Langevin equation. The extraction method for the computation of memory kernels described in Chapter 5 is well suited for the analysis of the center of charge trajectory computed from the ab initio simulations. Such a model will provide a link between experimentally measurable spectra, memory friction and even transition paths, since the fast proton diffusion in water is only possible due to frequent barrier-crossing reactions [16, 17].

Infrared spectral signatures of OH^- defects. Despite the intuitive notion of an apparently similar transport mechanism compared to hydrated excess protons, the diffusion of OH^- defects in water is different and less well understood [277–279]. As expected due to the charge transfer, they show similar continuum absorption features in the infrared spectrum as observed for excess protons [277, 280]. Therefore, a study of the spectral signatures (and other properties) of OH^- defects in small water clusters may yield new important insights. A comparison to the spectra of protonated water clusters might be interesting for systems where it is unknown whether an observed continuum feature is due to an excess proton or due to a proton defect.

Infrared spectral signatures of other protonated donor-acceptor pairs. In the current study, we restricted the analysis to continuum bands caused by protonated water clusters. However, even for bacteriorhodopsin also an alternative mechanism that explains the continuum band by a shared proton between two glutamate residues has been proposed [137]. Based on our results, it appears likely that such a scenario corresponds to an increased infrared absorption along the axis connecting the two residues. Nonetheless, for a better interpretation of continuum bands, it will be interesting to compare the polarization-resolved spectral signatures of typical proton donor-acceptor combinations found in proton-conducting proteins.

Confinement-dependent friction. The confinement-dependence of the friction constant has been demonstrated using a spherical test particle. The fact that confinement-dependent friction is observed in this simple case suggests that the effect is universal, and the upscaling arguments described in Chapter 3 imply that it is expected to be relevant for larger particles in more viscous solvents, too. Thus, simulations and direct experimental investigation of larger and more complex confined solutes might yield fruitful results. In addition to the obvious variation of solute and solvents, it will be interesting to investigate the water dynamics in the presence of larger structures with varied flexibility. Indeed, a previous simulation study reported slowed-down water dynamics around a completely frozen protein [206]. With the findings from this thesis in mind, it might be possible to disentangle the contributions to the slowing down of hydration water that are due to the chemical properties like roughness, charge or hydrophobicity from dynamic effects near solvated molecular surfaces.

Parametrization of generalized Langevin models. The method for the parametrization of generalized Langevin equations developed in Chapter 5 works for arbitrary potential energy landscapes, without additional assumptions. Thus, it can be applied to a variety of systems. This is particularly interesting since the generalized Langevin equation holds universally for projected dynamics of Hamiltonian systems [60], but also because of the numerous applications from different fields, where generalized Langevin models have been employed [63–72]. One could, for example, apply this parametrization method to projected dynamics of larger polymers and proteins. For this, a crucial step will be to understand how the long-time tails of the memory kernels can be resolved if the short-time information is missing. Once that is understood, properly parametrized Langevin models might be suited to describe relevant non-Markovian aspects of protein folding.

Internal friction in proteins. For various proteins, internal friction contributions have been found experimentally [10, 25–29] or by simulations [8, 120, 241]. The result from this thesis that the dihedral angle isomerization reactions are dominated by internal friction themselves provides a different view onto this problem. It should be investigated how this effect affects the protein dynamics. Freezing internal protein de-

grees of freedom without altering the folding pathway is probably not possible. Instead, one approach could be to use the memory kernels computed for butane to parametrize empirical internal friction models [241], and then compare the results to simulations, or if possible, to experiments.

Transition paths in the presence of memory friction. The characterization of the transition path ensemble via effective temperatures and transition path shapes is based on an instantaneous friction model. In a straightforward extension, it would be interesting to investigate the influence of memory friction on the transition path ensemble, in particular, because even in one dimension, barrier-crossing in the presence of memory friction is quite complicated [281–283],[vi]. The simulations could be carried out for a single-exponential memory kernel using the method described in Appendix D.2, or with its straight-forward generalization to multi-exponential memory kernels.

Appendix A

Orientation of Non-Spherical Protonated Water Clusters Revealed by Infrared Absorption Dichroism

A.1. Calculation of Infrared Spectrum Contributions from the Nuclear Motion

The spectral contributions of nuclear motion neglecting electronic polarization effects (n) shown in Fig. 2.3 for the protonated narrow chain are calculated from the ab initio trajectories by assigning effective charges to the nuclei, but ignoring the electronic degrees of freedom. For protonated clusters, this is a crude approximation since the effective nuclei charges near the excess proton differ from the effective charges elsewhere. However, the total absorbance of unprotonated clusters is small in the frequency range of the continuum band between $2000\,\mathrm{cm}^{-1}$ and $3000\,\mathrm{cm}^{-1}$. This observation motivates our choice $q_\mathrm{H} = +e$ and $q_\mathrm{O} = -2e$. The total excess charge of the system is thus correct and localized near the excess proton. The contribution of neutral water molecules is overestimated, which explains why the vibrational peaks are too large compared to the n+e calculation including electronic degrees of freedom.

A.2. Zundel Occupation Probabilities

We identify Zundel states based on the asymmetric stretch coordinate $\delta = d_{\mathrm{O_1H}} - d_{\mathrm{O_2H}}$, where $d_{\mathrm{O_1H}}$ and $d_{\mathrm{O_2H}}$ denote the distances between a proton and the two nearest oxygen nuclei $\mathrm{O_1}$ and $\mathrm{O_2}$ [17], see Fig. A.4 for an illustration. We define a Zundel complex by the criterion $|\delta| < \delta_\mathrm{thr}$. In Fig. A.5, the Zundel occupation probability calculated from the ab initio trajectories is given as a function of the threshold δ_thr for all four protonated water cluster geometries. Despite the fact that there is no canonical choice for δ_thr, the curves clearly show that the Zundel state is occupied significantly more often in the linear geometries than in discs and droplets. Note that we observe the lowest

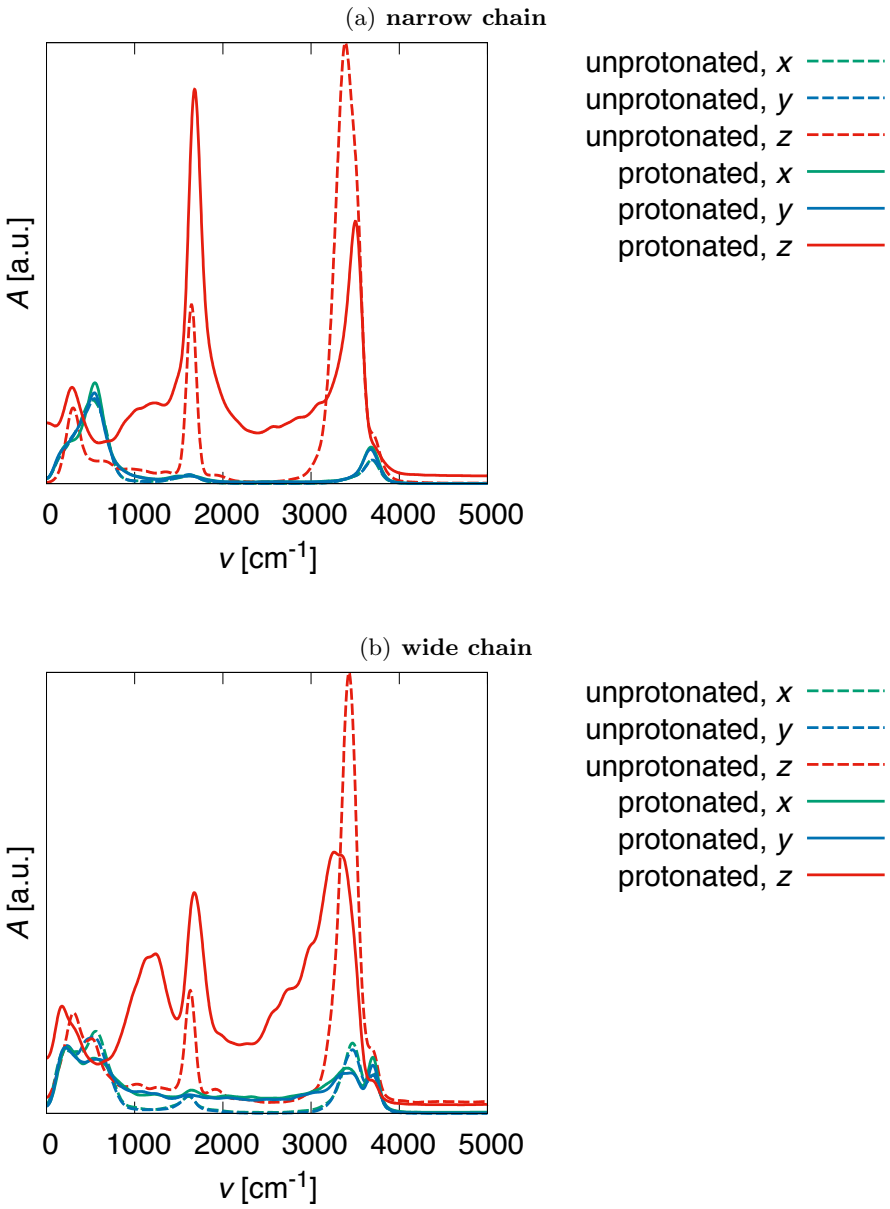

Figure A.1.: Individual x, y and z contributions to the infrared spectra computed from ab initio trajectories for (a) a narrow chain and (b) a wide chain with (solid lines) and without (dashed lines) an excess proton. The differences between the x and y contributions are an estimate of the magnitude of statistical errors.

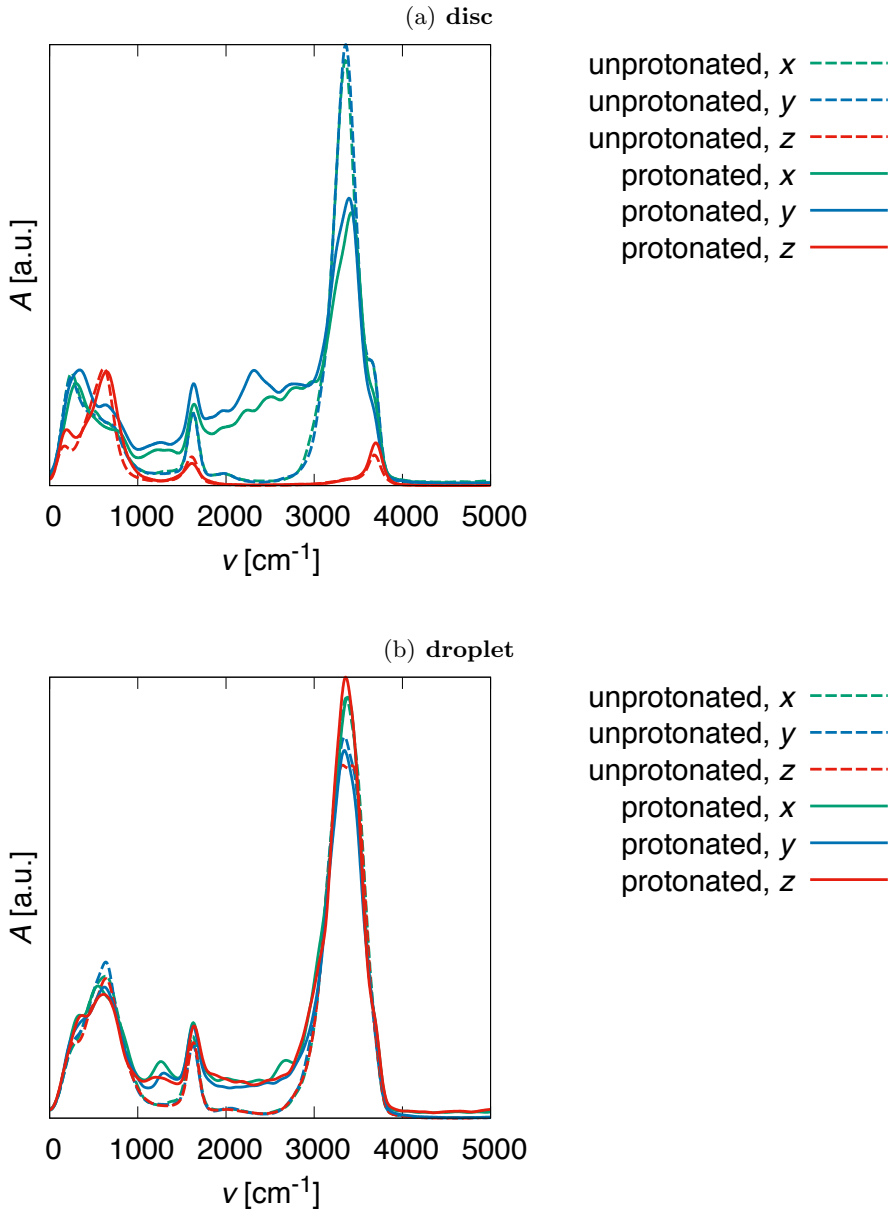

Figure A.2.: Individual x, y and z contributions to the infrared spectra computed from ab initio trajectories for (a) a disc and (b) a droplet with (solid lines) and without (dashed lines) an excess proton. The differences between the x, y (and z for the droplet) contributions are an estimate of the magnitude of statistical errors.

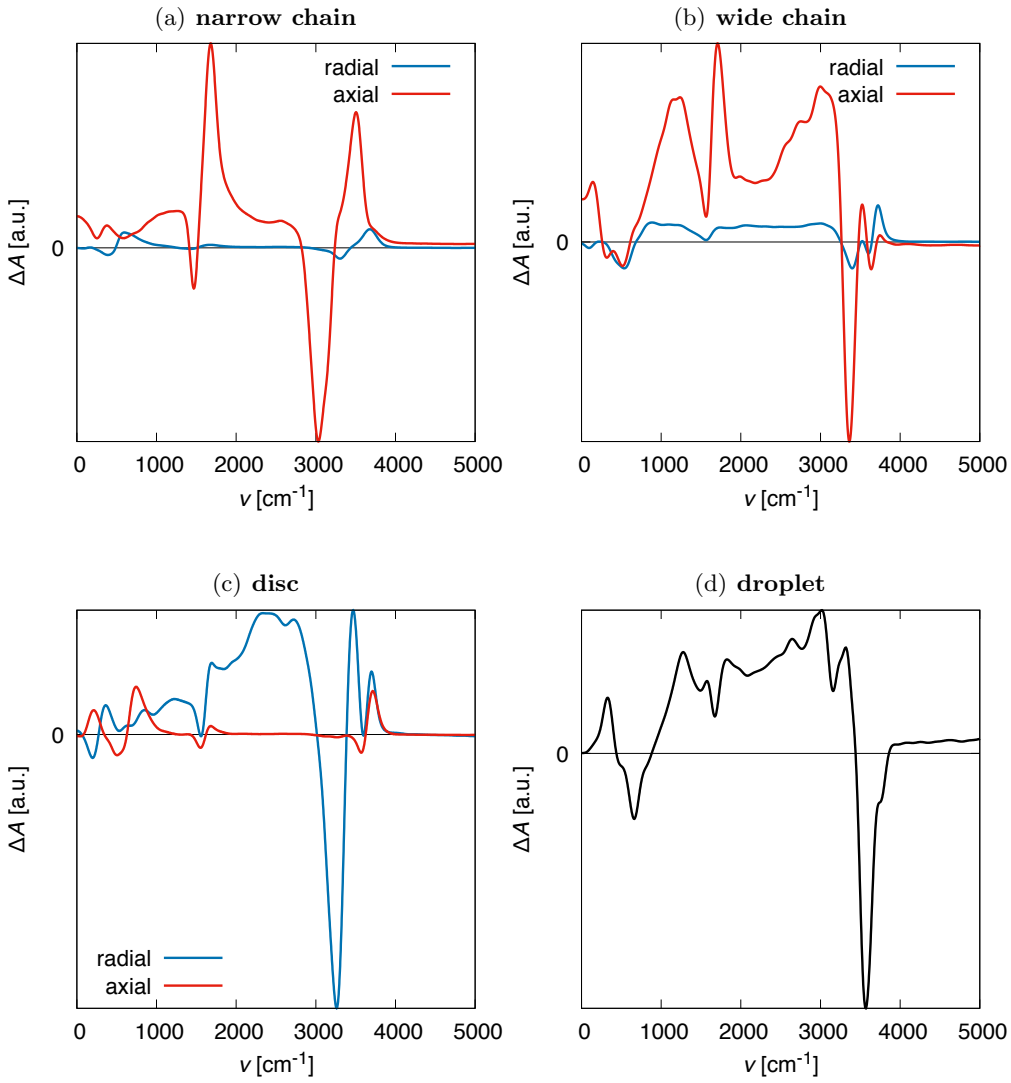

Figure A.3.: Polarization-dependent protonated-unprotonated difference spectra computed from the ab ab initio trajectories for (a) a narrow chain, (b) a wide chain, (c) a disc and (d) a droplet.

Zundel occupation number for the disc system, suggesting that the Eigen complex is stabilized in discs compared to bulk water.

For completeness, we show in Fig. A.6 the two-dimensional probability distributions $\rho(\delta, d_{O_1O_2})$ of the asymmetric stretch δ and the oxygen distance $d_{O_1O_2}$ [17]. The plots confirm the above conclusion that the Zundel state, which corresponds to small $|\delta|$ and small $d_{O_1O_2}$, is realized more frequently in chains than in discs and droplets.

A.3. Spectral Projection of Zundel Complex Contributions

For the projection of the spectrum on the Zundel ensemble, we define an instantaneous projection operator $P_Z^{inst}(t)$ that selects all nuclei belonging to a Zundel complex, based on the asymmetry coordinate δ as discussed in section A.2. Here we choose $|\delta| < \delta_{thr} = 0.05\,\text{Å}$ to identify a Zundel complex. The nuclei belonging to a Zundel state are the central excess proton, the two neighboring oxygen nuclei O_1 and O_2 as well as the four additional protons coordinated to the oxygen nuclei O_1 and O_2. When no Zundel complex is found, we define $P_Z^{inst}(t) = \emptyset$. Clearly, this definition of $P_Z^{inst}(t)$ depends on the choice of δ_{thr}. Furthermore, the resulting trajectory pieces are in general too short for a proper spectroscopic analysis. Motivated by the fact that in the trajectories rapid oscillations of the excess proton between two neighboring water molecules are often observed, we define a retarded Zundel operator $P_Z^{ret}(t)$ by keeping the nuclei identified by $P_Z^{inst}(t)$ until a new Zundel state is found, i.e.

$$P_Z^{ret}(t) = P_Z^{inst}(\max\{t' \,|\, t' \leq t \text{ and } P_Z^{inst}(t') \neq \emptyset\}). \tag{A.1}$$

From the resulting set of trajectories after projection by $P_Z^{ret}(t)$, we calculate the center-of-charge trajectory for the retarded Zundel ensemble from the trajectories of the nuclei and the coordinated Wannier centers. Since the nuclei indices change due to the proton hopping process, these trajectories are not continuous. To account for this, we make the trajectory continuous by subtracting the corresponding offsets. We use these trajectories to compute the spectra of the Zundel state (included in Fig. 2.3) for both the n+e and the n ensemble. We remark that in a recent publication a similar method has been used to calculate infrared spectral signatures of protonated water clusters in bulk water [162].

A.4. Determination of the Number of Water Molecules and Confinement Potential Strengths for the Disc and the Droplet Simulations

Disc. For the disc, the confinement potential strength is determined from two-dimensional classical water simulations using the GROMACS 4.6 [189] simulation package

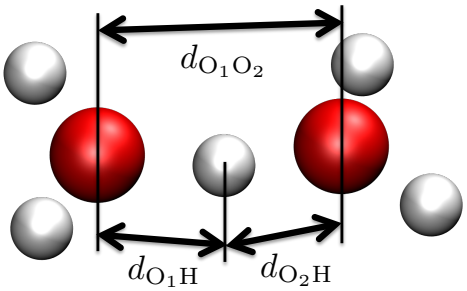

Figure A.4.: Illustration of a Zundel cation and the asymmetric stretch coordinate $\delta = d_{O_1H} - d_{O_2H}$.

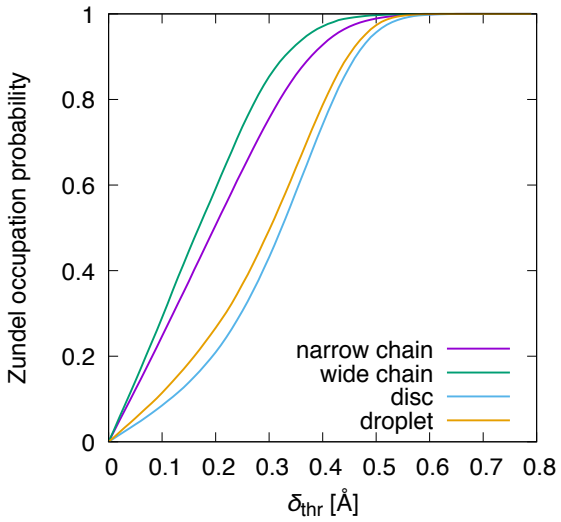

Figure A.5.: Occupation probability of the Zundel state as a function of the asymmetric stretch threshold δ_{thr} for the different protonated water cluster geometries.

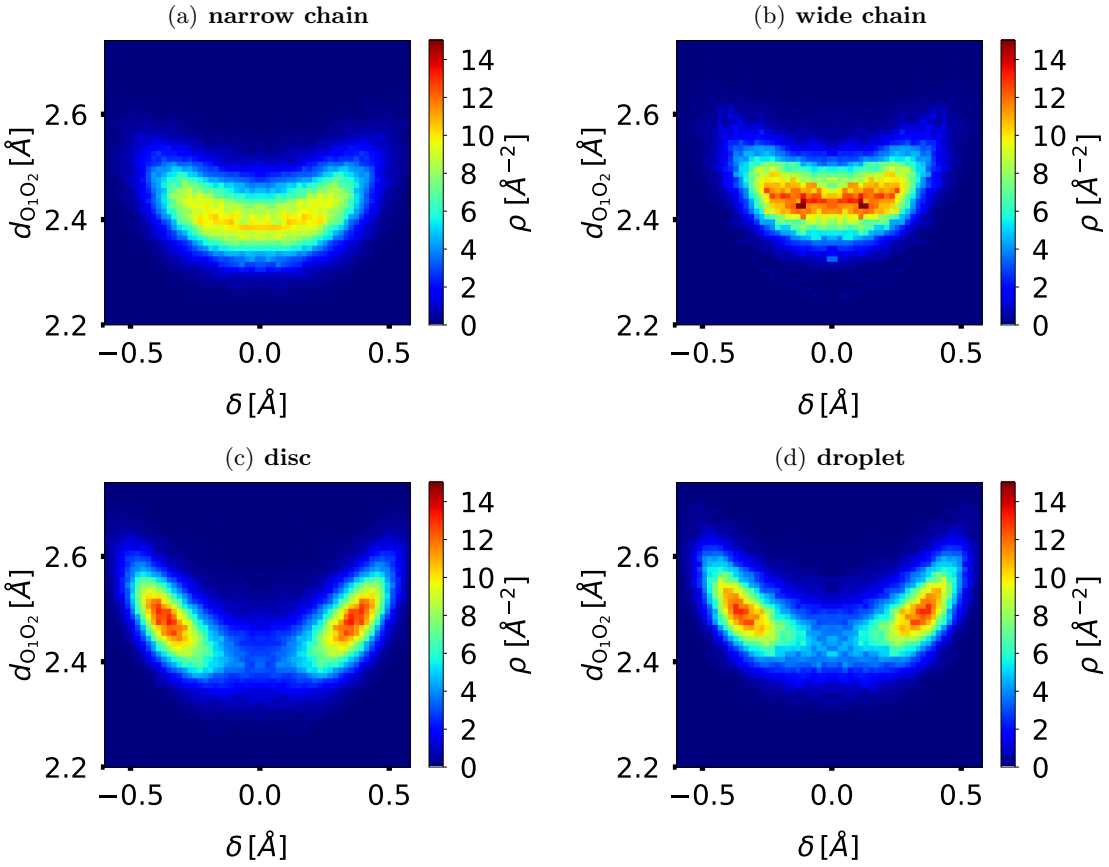

Figure A.6.: The probabilty distribution $\rho(\delta, d_{O_1O_2})$ for the proton with the smallest asymmetric stretch with respect to its two nearest oxygen nuclei. Small $|\delta|$ and small $d_{O_1O_2}$ correspond to Zundel states.

and the SPC/E [192] water model. The oxygen atoms are constrained to a two-dimensional, periodic plane along the x and y direction (the plane has dimensions of 3.5 nm × 3.5 nm and is embedded in a 3.5 nm × 3.5 nm × 4 nm box). We simulate an NPT ensemble for 5 ns using a v-rescale thermostat [193] at $T = 300\,\mathrm{K}$ and a Berendsen barostat [194] at $P = 1\,\mathrm{bar}$ coupled only to the x and y directions. In Fig. A.7(a), we show the unnormalized radial distribution function $dN(r)/dr$ obtained from the last 1.5 ns, where $N(r)$ denotes the number of oxygen atoms within radius r with respect to an oxygen atom. The peak structure implies that within $r_0 \approx 0.64\,\mathrm{nm}$, two circular shells of water around a central molecule are present. Integration of the data yields

$$\int_0^{r_0} dr\, \frac{dN(r)}{dr} \approx 15, \tag{A.2}$$

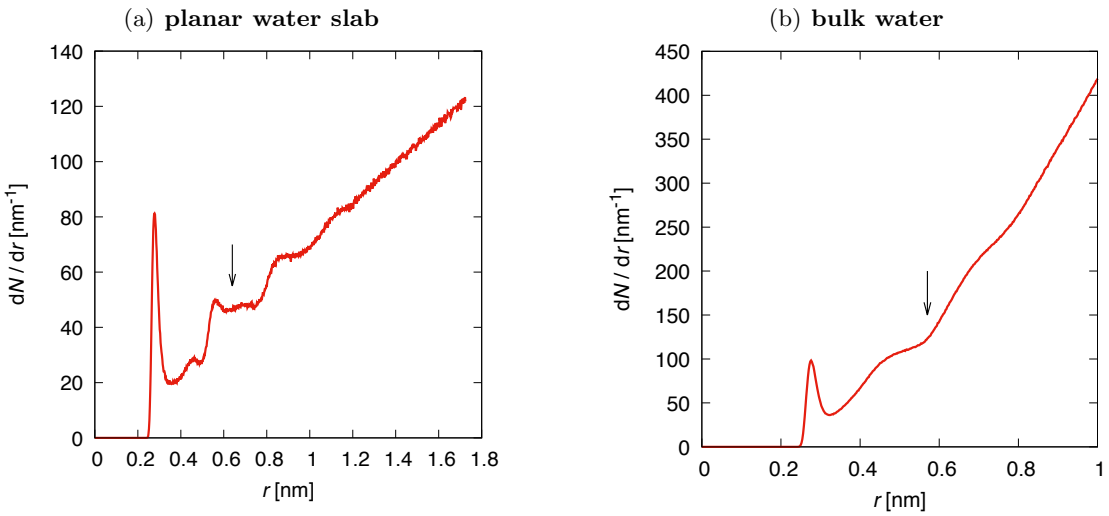

Figure A.7.: Unnormalized radial distribution functions $dN(r)/dr$ for (a) a two-dimensional periodic SPC/E water plane and (b) three-dimensional bulk SPC/E water, where $N(r)$ denotes the number of oxygen atoms within radius r with respect to an oxygen atom. The radii r_0 are indicated by arrows.

i.e. on average 15 oxygen atoms are found within r_0. The confinement potential strength $K_{xy} = 30\,\mathrm{kJ\,mol^{-1}\,nm^{-2}}$ for the ab initio simulations is chosen so that the 15 water molecules typically stay within the radius $r_0 \approx 0.64\,\mathrm{nm}$, implying that the planar water density in the ab initio simulation roughly agrees with the value from the classical simulation with periodic boundary conditions.

Droplet. For the droplet, we simulate a cubic water box of volume $(3\,\mathrm{nm})^3$, with isotropic pressure [194] and temperature [193] coupling. We show $dN(r)/dr$ in Fig. A.7(b) and find that two hydration shells of water are found within a radius $r_0 \approx 0.57\,\mathrm{nm}$, corresponding to 26 water molecules. To confine the droplet in the ab initio simulations, we choose a force constant of $K_r = 40\,\mathrm{kJ\,mol^{-1}\,nm^{-2}}$, which yields the same density as in the classical simulation of bulk water.

Appendix B

External Potential Modifies Friction of Molecular Solutes in Water

B.1. Estimate of the Contribution of the Repulsive Interaction between Methane and Water to the Memory Kernel

Here we show that repulsive methane-water interactions give rise to a relaxation time that matches the shortest memory timescale τ_1. The force autocorrelation function of an undamped harmonic oscillator is

$$\langle F(0)F(t)\rangle \propto \cos\left(\omega_{\mathrm{rel}} t\right), \tag{B.1}$$

where the characteristic frequency is

$$\omega_{\mathrm{rel}} = \sqrt{K_{\mathrm{rel}}/m_{\mathrm{rel}}}, \tag{B.2}$$

and

$$m_{\mathrm{rel}} = \frac{m_{\mathrm{H_2O}} m_{\mathrm{CH_4}}}{m_{\mathrm{H_2O}} + m_{\mathrm{CH_4}}} \tag{B.3}$$

denotes the relative mass of the molecule pair. We determine the force constant K_{rel} from the free energy $\mathcal{F}(r)$ as a function of the methane-water distance r, shown by a black line in Fig. B.1, which is obtained from the radial distribution function $g(r)$ shown in Fig. 3.1(b) via

$$\mathcal{F}(r) = -k_{\mathrm{B}} T \log g(r). \tag{B.4}$$

Note that $\mathcal{F}(r)$ is very anharmonic even on energy scales of the order of the thermal energy $k_B T$, so a harmonic fit to the entire function $\mathcal{F}(r)$ is not useful. To extract the fastest timescale of particle motion in this free energy profile, we fit a harmonic potential

$$U(r) = \frac{1}{2} K_{\mathrm{rel}} (r - r_0)^2 \tag{B.5}$$

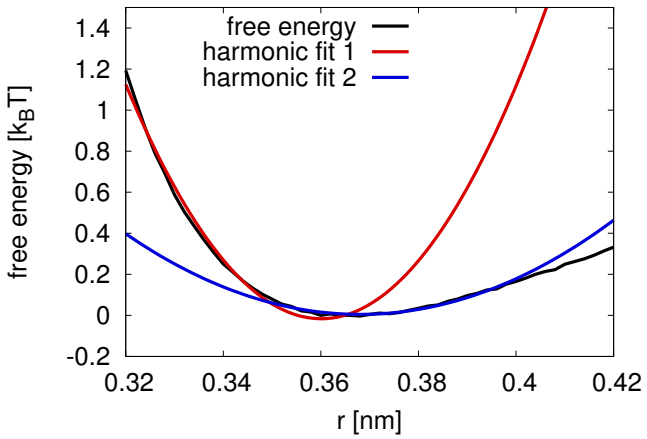

Figure B.1.: The free energy $\mathcal{F}(r)$ associated with the distance r between the methane and surrounding water molecules together with a harmonic fit to the repulsive part (red line) and a harmonic fit around the free energy minimum (blue line).

to the repulsive part in the range $0.32\,\mathrm{nm} < r < 0.36\,\mathrm{nm}$ only, which is denoted by the red line in Fig. B.1. The result is $K_{\mathrm{rel}} = 3,548\,\mathrm{kJ/(mol\,nm^2)}$. To obtain the fastest timescale τ_1 of the memory kernel defined in Eq. (3.7), we demand that the stretched exponential function in Eq. (3.7) and the oscillatory function in Eq. (B.1) have both decayed to $1/e$, which is equivalent to

$$\cos\left(\omega_{\mathrm{rel}}\tau_1\right) = \frac{1}{e}, \tag{B.6}$$

from which we obtain with our estimate for K_{rel} and m_{rel} given by Eq. (B.3) the timescale

$$\tau_1 = \frac{1}{\omega_{\mathrm{rel}}} \cos^{-1}\left(e^{-1}\right) = 58\,\mathrm{fs}, \tag{B.7}$$

which holds for unconfined methane. If the methane molecule is frozen, which corresponds to $m_{\mathrm{CH_4}} \to \infty$, we use $m_{\mathrm{rel}} = m_{\mathrm{H_2O}}$ and obtain

$$\tau_1 = 85\,\mathrm{fs}. \tag{B.8}$$

These times are included in Fig. 3.3(b) as red arrows and match the simulated times quite nicely.

For comparison, if we repeat the analysis but use instead of the fit to the repulsive part of the free energy a harmonic fit around the minimum of the free energy $\mathcal{F}(r)$, denoted by the blue line in Fig. B.1, we obtain the timescales $\tau_1 = 119\,\mathrm{fs}$ for free methane and $\tau_1 = 174\,\mathrm{fs}$ for frozen methane. These timescales are significantly larger than the fastest timescale of the memory function. We conclude that the fast initial decay of the memory function is indeed caused by repulsive interactions between the solute and the solvent molecules.

B.2. Confinement-Dependent Friction for a Hydrated Water Molecule

To demonstrate that the confinement dependence of the friction coefficient is not limited to hydrophobic solutes, we simulate a confined SPC/E [192] water molecule solvated in a cubic SPC/E water box with $L = 4.5\,\mathrm{nm}$ for 250 ns for each K. We present in Fig. B.2 the solvent force autocorrelation functions $C_{FF}^{\mathrm{sol}}(t)$ and the running integrals $I_{FF}^{\mathrm{sol}}(t)$ of the confined water molecule for different potential strengths K between $25\,\mathrm{kJ/(mol\,nm^2)}$ and $250,000\,\mathrm{kJ/(mol\,nm^2)}$. As shown in section 3.1, the height of the plateau of $I_{FF}^{\mathrm{sol}}(t)$ corresponds to the friction constant, i.e.

$$\gamma = \frac{1}{k_{\mathrm{B}}T} \lim_{t\to\infty} I_{FF}^{\mathrm{sol}}(t). \tag{B.9}$$

We conclude from the K-dependence of the heights of the plateaus of $I_{FF}^{\mathrm{sol}}(t)$ shown in Fig. B.2(b) that also the friction coefficient of water increases significantly with rising confinement potential strength.

B.3. Decomposition of the Friction Coefficient

Here, we decompose the methane friction coefficient into contributions from different terms in the memory kernel according to $\gamma = \sum_i \gamma_i$ with the definition

$$\gamma_i = A_i \int_0^\infty dt \exp\left(-\left|\frac{t}{\tau_i}\right|^{\alpha_i}\right), \tag{B.10}$$

where A_i, α_i and τ_i are the parameters of the memory kernels defined in Eq. (3.7). The contributions γ_i are shown as a function of K for the system with $L = 4.5\,\mathrm{nm}$ in Fig. B.3 together with the total friction γ and the sum of the short time contributions $\gamma_1 + \gamma_2$. The results demonstrate that the total friction coefficient is dominated by the long time contribution γ_3, whereas the sum of the short time contributions $\gamma_1 + \gamma_2$ is constant. Since the timescale τ_3 is rather constant as a function of K as shown in Fig. 3.3(b), we conclude that the change of γ with K is solely due to an increase of the amplitude A_3 with increasing K.

B.4. Correlation Functions and Alternative Methods

B.4.1. Correlation Functions for Methane

In Fig. B.4 the (normalized) autocorrelation functions $C_{FF}(t) = \langle F(0)F(t)\rangle$, $C_{\dot{x}\dot{x}}(t) = \langle \dot{x}(0)\dot{x}(t)\rangle$ and $C_{xx}(t) = \langle x(0)x(t)\rangle$ are presented for the medium system size ($L = 4.5\,\mathrm{nm}$) and five different harmonic spring constants K. We observe that with larger spring constant all functions are subject to pronounced oscillatory behavior with a frequency close to $\omega_0 = \sqrt{K/m}$. The amplitude of these oscillations decays on timescales

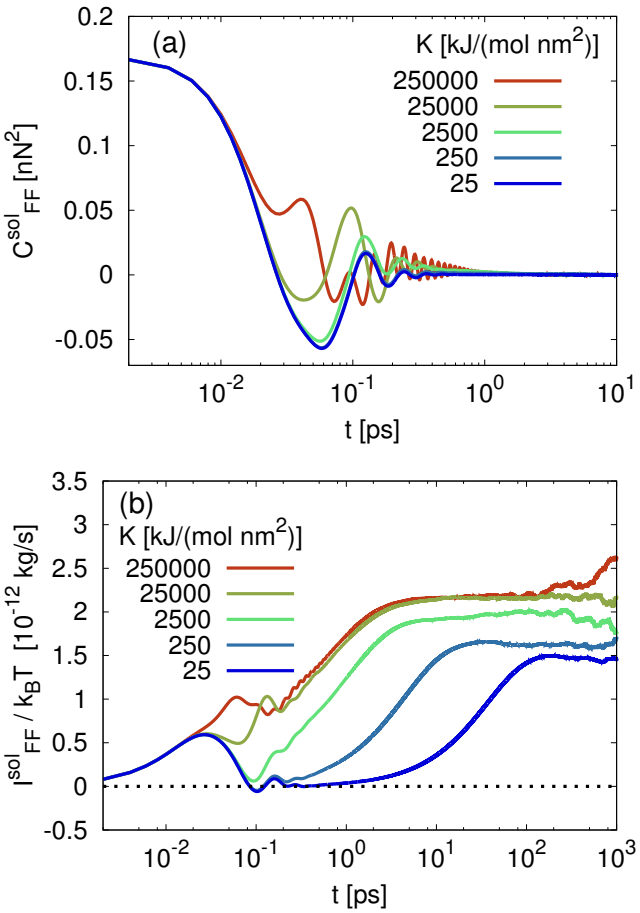

Figure B.2.: Simulated autocorrelations for water in water. (a) Solvent force autocorrelation functions $C^{\mathrm{sol}}_{FF}(t)$ and (b) integrals $I^{\mathrm{sol}}_{FF}(t)$ for a confined water molecule for different potential strengths K.

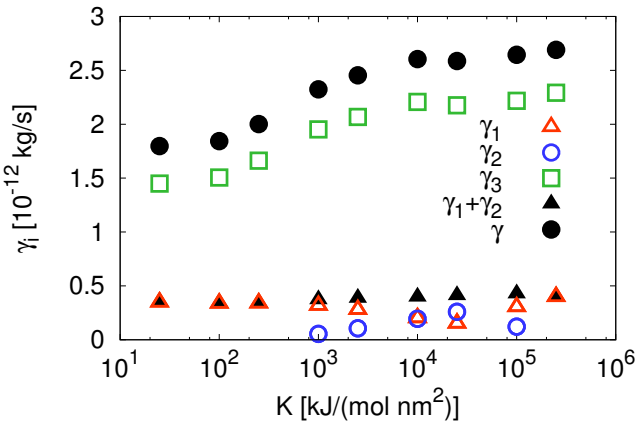

Figure B.3.: Comparison of the methane friction coefficient $\gamma = \gamma_1 + \gamma_2 + \gamma_3$ with its contributions γ_i defined by Eq. (B.10) as a function of K. We also show the sum of the short time contributions $\gamma_1 + \gamma_2$.

between 0.5 ps and 5 ps, force and velocity autocorrelation functions with small spring constants decay the fastest. Note that these oscillations are much more pronounced than the oscillations in $C^{\mathrm{sol}}_{FF}(t)$ presented in Fig. 3.2(a).

B.4.2. Analytic Expressions for Correlation Functions

Here, we give analytic expressions for the correlation functions $C_{xx}(t) = \langle x(0)x(t)\rangle$, $C_{\dot{x}\dot{x}}(t) = \langle \dot{x}(0)\dot{x}(t)\rangle$ and $C_{FF}(t) = \langle F(0)F(t)\rangle$, which can be derived analogously to Eq. (3.4) from the GLE Eq. (3.1):

$$\tilde{C}_{xx}(\omega) = \frac{k_{\mathrm{B}}T\tilde{\Gamma}(\omega)}{\left|m\omega^2 - K - i\omega\tilde{\Gamma}_+(\omega)\right|^2}\,, \tag{B.11}$$

$$\tilde{C}_{\dot{x}\dot{x}}(\omega) = \frac{\omega^2 k_{\mathrm{B}}T\tilde{\Gamma}(\omega)}{\left|m\omega^2 - K - i\omega\tilde{\Gamma}_+(\omega)\right|^2}\,, \tag{B.12}$$

$$\tilde{C}_{FF}(\omega) = \frac{m^2\omega^4 k_{\mathrm{B}}T\tilde{\Gamma}(\omega)}{\left|m\omega^2 - K - i\omega\tilde{\Gamma}_+(\omega)\right|^2}\,. \tag{B.13}$$

As we have $\tilde{C}_{\dot{x}\dot{x}}(0) = 0$ and $\tilde{C}_{FF}(0) = 0$ for $K \neq 0$, clearly, the integrals of these two correlation functions will not be suited to extract the friction constant. Only the position autocorrelation function is non-zero at zero frequency, i.e. $\tilde{C}_{xx}(0) = k_{\mathrm{B}}T\tilde{\Gamma}(0)/K^2 = 2k_{\mathrm{B}}T\gamma/K^2$ for $K \neq 0$, and thus in principle allows to extract the friction coefficient.

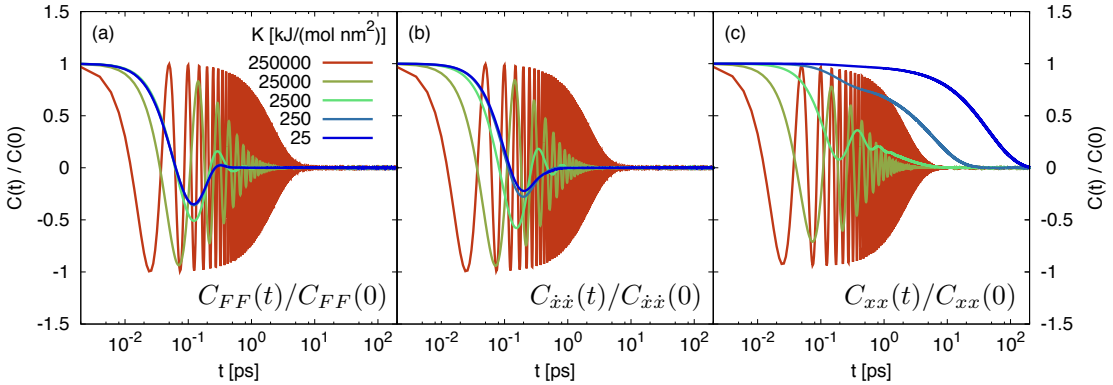

Figure B.4.: The normalized autocorrelation functions $C_{FF}(t)/C_{FF}(0)$, $C_{\dot{x}\dot{x}}(t)/C_{\dot{x}\dot{x}}(0)$ and $C_{xx}(t)/C_{xx}(0)$ for the system with the size $L = 4.5\,\mathrm{nm}$ and five different spring constants K of the harmonic potential.

We remark that for vanishing confinement, $K = 0$, the velocity autocorrelation fulfills

$$\tilde{C}_{\dot{x}\dot{x}}(0) = \frac{k_\mathrm{B}T\tilde{\Gamma}(0)}{\left|\tilde{\Gamma}_+(0)\right|^2} = \frac{2k_\mathrm{B}T}{\gamma}, \tag{B.14}$$

and thus allows to extract γ. Note however that all given correlation functions are subject to large amplitude oscillations for sufficiently high values of K, which limits the practical usefulness, as is demonstrated in Fig. B.4.

B.4.3. Comparison to an Extraction Method Based on the Position Autocorrelation Function

Hummer et al. developed a method to calculate the friction coefficient from the position autocorrelation function in systems with a biasing potential [284]. Starting from the work of Woolf and Roux [285], they showed that the diffusion coefficient D of a particle in a harmonic potential $U(x) = Kx^2/2$ can be written as

$$D = \frac{\left\langle x^2 \right\rangle^2}{\int_0^\infty dt\, \left\langle x(0)x(t) \right\rangle}, \tag{B.15}$$

or, in terms of the friction coefficient,

$$\gamma = \frac{K^2}{k_B T} \int_0^\infty dt\, \left\langle x(0)x(t) \right\rangle . \tag{B.16}$$

We note that this result can be directly derived from Eq. (B.11) according to

$$\int_0^\infty dt\, C_{xx}(t) = \frac{1}{2}\tilde{C}_{xx}(0) = \frac{k_\mathrm{B}T\gamma}{K^2}, \tag{B.17}$$

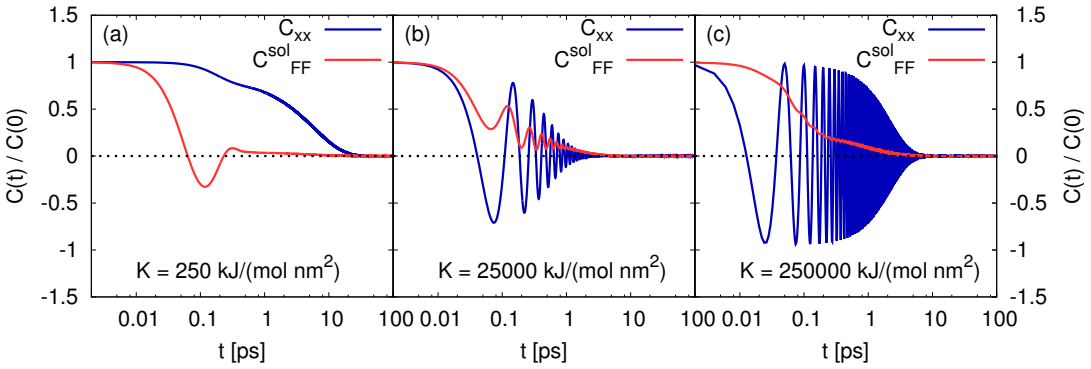

Figure B.5.: Normalized position autocorrelation function $C_{xx}(t)/C_{xx}(0)$ (blue) and normalized solvent force autocorrelation function $C^{\mathrm{sol}}_{FF}(t)/C^{\mathrm{sol}}_{FF}(0)$ (red) for spring constants (a) $250\,\mathrm{kJ/(mol\,nm^2)}$, (b) $25,000\,\mathrm{kJ/(mol\,nm^2)}$, and (c) $250,000\,\mathrm{kJ/(mol\,nm^2)}$.

which is equivalent to Eq. (B.16).

We compare the (normalized) position autocorrelation function $C_{xx}(t) = \langle x(0)x(t)\rangle$ with the (normalized) solvent force autocorrelation function $C^{\mathrm{sol}}_{FF}(t) = \langle F_{\mathrm{sol}}(0)F_{\mathrm{sol}}(t)\rangle$ in Fig. B.5. We conclude that for sufficiently small values of K, the two methods should work equally fine. However, as already pointed out in Ref. [284], the position autocorrelation function is dominated by oscillations, which render the integration numerically unstable for large values of K. Our method that is based on $C^{\mathrm{sol}}_{FF}(t)$ is suitable to extract the friction coefficient and the memory kernel for all values of the confinement strength K.

B.4.4. Parametrization-Free Methods to Extract the Memory Kernels

In principle, the memory functions can be extracted numerically in a parametrization-free way from correlation functions in the time domain [9, 61, 73], see also Chapter 5. Due to the instability of the inversion scheme [9], this approach is in practice quite unstable for systems with high values of K, which are subject to fast oscillatory behavior in the relevant correlation functions (see Fig. B.4). We remark that the parametrization of the memory kernel as it is used in Chapter 3 can be regarded as a regularization of the problem [9].

B.5. Detailed Derivation of the Analytic Expression for the Solvent Force Autocorrelation Function

In this section, we derive Eq. (3.4) based on the generalized Langevin equation (3.1). We define the autocorrelation function

$$C^{\mathrm{sol}}_{FF}(t) = \langle F_{\mathrm{sol}}(0)F_{\mathrm{sol}}(t)\rangle \tag{B.18}$$

of the solvent force

$$F_{\mathrm{sol}}(t) = F(t) + \nabla U(x(t)) = m\ddot{x}(t) + Kx\,, \tag{B.19}$$

where $F(t) = m\ddot{x}(t)$ denotes the total force. Starting from the Fourier transformed generalized Langevin equation

$$-m\omega^2\tilde{x}(\omega) = -i\omega\tilde{\Gamma}_+(\omega)\tilde{x}(\omega) - K\tilde{x}(\omega) + \tilde{F}_{\mathrm{R}}(\omega)\,, \tag{B.20}$$

with

$$\tilde{f}(\omega) = \int_{-\infty}^{\infty} dt\, e^{-i\omega t} f(t)\,, \tag{B.21}$$

we can solve for $\tilde{x}(\omega)$

$$\tilde{x}(\omega) = \frac{\tilde{F}_{\mathrm{R}}(\omega)}{-m\omega^2 + K + i\omega\tilde{\Gamma}_+(\omega)}\,. \tag{B.22}$$

Hence, the Fourier transformed solvent force obeys

$$\begin{aligned}
\tilde{F}_{\mathrm{sol}}(\omega) &= \tilde{F}(\omega) + K\tilde{x}(\omega) && \text{(B.23)}\\
&= (-m\omega^2 + K)\tilde{x}(\omega) && \text{(B.24)}\\
&= \frac{(-m\omega^2 + K)\tilde{F}_{\mathrm{R}}(\omega)}{-m\omega^2 + K + i\omega\tilde{\Gamma}_+(\omega)} && \text{(B.25)}\\
&= \tilde{Q}_{\mathrm{sol}}(\omega)\tilde{F}_{\mathrm{R}}(\omega), && \text{(B.26)}
\end{aligned}$$

where we defined

$$\tilde{Q}_{\mathrm{sol}}(\omega) = \frac{-m\omega^2 + K}{-m\omega^2 + K + i\omega\tilde{\Gamma}_+(\omega)}. \tag{B.27}$$

In the time domain Eq. (B.26) implies

$$F_{\mathrm{sol}}(t) = \int_{-\infty}^{\infty} dt' Q_{\mathrm{sol}}(t-t')F_{\mathrm{R}}(t'), \tag{B.28}$$

and hence we can write for the autocorrelation function

$$\begin{aligned}
C_{FF}^{\mathrm{sol}}(t) &= \langle F_{\mathrm{sol}}(t)F_{\mathrm{sol}}(0)\rangle && \text{(B.29)}\\
&= \left\langle \int_{-\infty}^{\infty} dt'\, Q_{\mathrm{sol}}(t-t')F_{\mathrm{R}}(t') \int_{-\infty}^{\infty} dt''\, Q_{\mathrm{sol}}(-t'')F_{\mathrm{R}}(t'') \right\rangle && \text{(B.30)}\\
&= \int_{-\infty}^{\infty} dt' \int_{-\infty}^{\infty} dt''\, Q_{\mathrm{sol}}(t-t')Q_{\mathrm{sol}}(-t'') \left\langle F_{\mathrm{R}}(t')F_{\mathrm{R}}(t'')\right\rangle && \text{(B.31)}\\
&= k_{\mathrm{B}}T \int_{-\infty}^{\infty} dt' \int_{-\infty}^{\infty} dt''\, Q_{\mathrm{sol}}(t-t')Q_{\mathrm{sol}}(-t'')\Gamma(t'-t'') && \text{(B.32)}\\
&= k_{\mathrm{B}}T \int_{-\infty}^{\infty} dt'\, Q_{\mathrm{sol}}(t-t') \int_{-\infty}^{\infty} dt'' Q_{\mathrm{sol}}(-t'')\Gamma(t'-t''), && \text{(B.33)}
\end{aligned}$$

where the average in Eq. (B.31) was evaluated using the fluctuation-dissipation theorem $\langle F_{\mathrm{R}}(0)F_{\mathrm{R}}(t)\rangle = k_{\mathrm{B}}T\Gamma(t)$. Thus, in Fourier space we obtain

$$\tilde{C}^{\mathrm{sol}}_{FF}(\omega) = k_{\mathrm{B}}T\tilde{Q}_{\mathrm{sol}}(\omega)\tilde{Q}_{\mathrm{sol}}(-\omega)\tilde{\Gamma}(\omega) = k_{\mathrm{B}}T\left|\tilde{Q}_{\mathrm{sol}}(\omega)\right|^2\tilde{\Gamma}(\omega), \tag{B.34}$$

which is equivalent to Eq. (3.4):

$$\tilde{C}^{\mathrm{sol}}_{FF}(\omega) = k_{\mathrm{B}}T\left|\tilde{Q}_{\mathrm{sol}}(\omega)\right|^2\tilde{\Gamma}(\omega) = \frac{k_{\mathrm{B}}T\,\tilde{\Gamma}(\omega)}{\left|1-\frac{i\omega}{m\omega^2-K}\tilde{\Gamma}_+(\omega)\right|^2}. \tag{B.35}$$

B.6. Integrated Solvent Force Autocorrelation Function

Since

$$\tilde{\Gamma}_+(0) = \int_0^\infty dt\,\Gamma(t) = \gamma, \tag{B.36}$$

where γ denotes the friction constant, is finite, we immediately see from Eq. (B.35) that $\tilde{C}^{\mathrm{sol}}_{FF}(0) = k_{\mathrm{B}}T\tilde{\Gamma}(0) = 2k_{\mathrm{B}}T\gamma$ for $K \neq 0$, because of $\Gamma(t) = \Gamma(-t)$. Using also the symmetry $C^{\mathrm{sol}}_{FF}(t) = C^{\mathrm{sol}}_{FF}(-t)$ we thus obtain Eq. (3.5):

$$\gamma = \frac{1}{k_{\mathrm{B}}T}\int_0^\infty dt\,C^{\mathrm{sol}}_{FF}(t). \tag{B.37}$$

B.7. Friction Constant for a Free Methane Molecule

We calculate the friction constant γ for the free case $K = 0$ from the mean-square displacement $\left\langle \Delta x^2(t)\right\rangle$ of the methane molecule via

$$\left\langle \Delta x^2(t)\right\rangle = 2D^{\mathrm{trans}}_{\mathrm{CH_4}}t = 2\frac{k_{\mathrm{B}}T}{\gamma}t, \tag{B.38}$$

where $D^{\mathrm{trans}}_{\mathrm{CH_4}}$ denotes the translational diffusion constant. The systems are simulated for $3\,\mu$s ($L = 3.0\,$nm), $1\,\mu$s ($L = 4.5\,$nm) and $0.7\,\mu$s ($L = 6.0\,$nm) in the NVT ensemble. The position of the methane molecule is saved every 0.2 ps. The resulting mean-square displacements are shown in Fig. B.6. Note that due to the low sampling rate, the ballistic regime is not resolved. The friction constants included in Fig. 3.4 as horizontal lines are extracted from fits to $\left\langle \Delta x^2(t)\right\rangle / t$ between 100 ps and 1,000 ps shown in Fig. B.6(b) as broken horizontal lines. We estimate the errors by comparing fits to the first and the second half of the interval and obtain $\Delta D^{\mathrm{trans}}_{\mathrm{CH_4}} = 0.018\cdot 10^{-5}\,\mathrm{cm^2/s}$ for $L = 3.0\,$nm, $\Delta D^{\mathrm{trans}}_{\mathrm{CH_4}} = 0.007\cdot 10^{-5}\,\mathrm{cm^2/s}$ for $L = 4.5\,$nm, and $\Delta D^{\mathrm{trans}}_{\mathrm{CH_4}} = 0.022\cdot 10^{-5}\,\mathrm{cm^2/s}$ for $L = 6.0\,$nm.

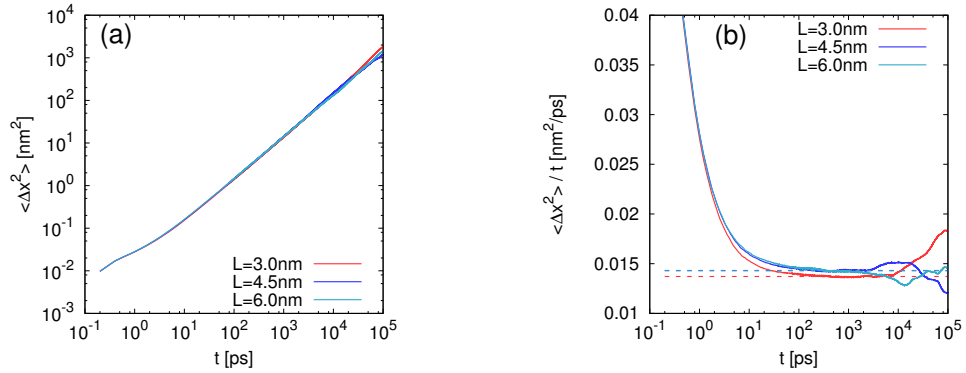

Figure B.6.: (a) The mean-square displacement $\langle \Delta x^2 \rangle$ as a function of t for a free methane molecule for three different system sizes. (b) $\langle \Delta x^2 \rangle / t$ as a function of t, fits between 100 ps and 1,000 ps are indicated by broken horizontal lines.

B.8. Estimation of Force Constants

Here we present the estimates of force constants K included in Fig. 3.4.

Van der Waals. We estimate the force constant of van der Waals interactions from the curvature in the minimum of the Lennard-Jones potential. Using typical values for the van der Waals parameters [286, 287] ($c_0 \approx 10^5\,\mathrm{m}^{-1}$, $R_e \approx 3.5 \cdot 10^{-10}\,\mathrm{m}$ according to the definitions of Refs. [286, 287]), we find

$$K = \frac{hc\,c_0}{2R_e} \approx 200\,\mathrm{kJ/(mol\,nm^2)}. \tag{B.39}$$

The following estimates are obtained from vibrational frequencies via

$$K = m_{\mathrm{rel}}\omega^2 = m_{\mathrm{rel}}\,(2\pi f)^2, \tag{B.40}$$

where f denotes the vibration frequency and $m_{\mathrm{rel}} = m_1 m_2/(m_1 + m_2)$ is the relative mass. For the estimates below, we assume $m_{\mathrm{rel}} = 10\,\mathrm{u}$, which is in the order of magnitude of the relative mass of a pair of methyl groups, typical hydrogen bond donor acceptor pairs and light monoatomic ion pairs. Here, u denotes the atomic mass unit. Note that this choice corresponds to examples of covalently or loosely bound objects with similar mass and size as the studied methane molecule.

Ion. The NaCl stretching frequency in solution is of the order $\nu \approx 100\,\mathrm{cm}^{-1}$ [288], thus we find

$$K \approx 2 \cdot 10^3\,\mathrm{kJ/(mol\,nm^2)}. \tag{B.41}$$

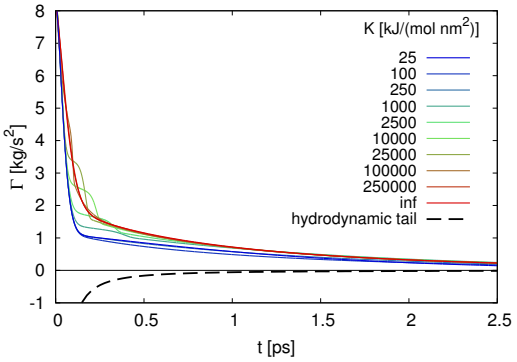

Figure B.7.: The memory kernels $\Gamma(t)$ (colored solid lines) shown in Fig. 3.3(a) are compared to the asymptotic hydrodynamic power-law contribution (broken line) Eq. (B.44).

Hydrogen bond. The hydrogen-bond stretch vibration in liquid water can be observed around $\nu \approx 200\,\mathrm{cm}^{-1}$ [289], which leads to an estimate of

$$K \approx 10^4\,\mathrm{kJ/(mol\,nm^2)}. \tag{B.42}$$

Covalent. Vibrational frequencies of covalent bonds between two carbon atoms are characterized by $\nu \approx 1500\,\mathrm{cm}^{-1}$[290], which corresponds to force constants of

$$K \approx 10^6\,\mathrm{kJ/(mol\,nm^2)}. \tag{B.43}$$

B.9. Hydrodynamic Contribution to the Memory Kernel

Here, we compare the memory kernels $\Gamma(t)$ to the negative asymptotic power-law contribution expected from hydrodynamics [71, 196]

$$\Gamma(t) \sim -\frac{2\gamma^2}{3\rho}\left[4\pi\left(D^{\mathrm{trans}}_{\mathrm{CH_4}} + \nu\right)t\right]^{-3/2}, \tag{B.44}$$

where $\rho = 1\,\mathrm{g/cm^3}$ denotes the water mass density, $\nu = \eta/\rho$ denotes the kinematic viscosity with $\eta = 0.85\,\mathrm{mPa\,s}$ being the water viscosity, and $D^{\mathrm{trans}}_{\mathrm{CH_4}} = k_{\mathrm{B}}T/\gamma = 2.38 \cdot 10^{-5}\,\mathrm{cm^2/s}$ is the diffusion constant of methane in water obtained from the fit shown in Fig. B.6(b) for the size $L = 4.5\,\mathrm{nm}$. This contribution is compared in Fig. B.7 to the memory kernels $\Gamma(t)$ extracted from the $L = 4.5\,\mathrm{nm}$ simulations. We confirm that its contribution is negligible in the ps timescale, since the memory kernel is positive with a significantly larger amplitude in this regime.

B.10. Fitting Procedure

For each spring constant K we use the parametrization Eq. (3.7)

$$\Gamma(t) = \sum_{i=1}^{n} A_i \exp\left(-\left|\frac{t}{\tau_i}\right|^{\alpha_i}\right) \tag{B.45}$$

with $n = 3$ stretched exponentials to fit the memory kernel. The full memory kernel $\Gamma(t)$ and the half-side kernel $\Gamma_+(t)$ are numerically Fourier transformed into $\tilde{\Gamma}(\omega)$ and $\tilde{\Gamma}_+(\omega)$. The solvent force autocorrelation function in Fourier space $\tilde{C}^{\mathrm{sol}}_{FF}(\omega)$ is then computed from the Fourier transformed memory kernels according to Eq. (3.4) and numerically back-transformed to $C^{\mathrm{sol}}_{FF}(t)$. The transformations in both ways are calculated via fast Fourier transform (FFT) with a resolution of 0.5 fs and an interval length of 2^{21} sampling points. The force autocorrelation function $C^{\mathrm{sol,sim}}_{FF}(t)$ is calculated from the trajectory $F_{\mathrm{sol,sim}}(t)$ extracted from the simulation data. Both functions $C^{\mathrm{sol}}_{FF}(t)$ and $C^{\mathrm{sol,sim}}_{FF}(t)$ are compared with each other and the squared deviation ΔC is defined as

$$\Delta C = \sum_{i=1}^{N} \left(C^{\mathrm{sol}}_{FF}(t_i) - C^{\mathrm{sol,sim}}_{FF}(t_i)\right)^2. \tag{B.46}$$

The same procedure is applied to the integrals $I^{\mathrm{sol}}_{FF}(t)$ and $I^{\mathrm{sol,sim}}_{FF}(t)$ over the functions $C^{\mathrm{sol}}_{FF}(t)$ and $C^{\mathrm{sol,sim}}_{FF}(t)$, which are in both cases computed via numerical integration using the trapezoidal rule. The resulting deviation ΔI is given by

$$\Delta I = \sum_{i=1}^{N} \left(I^{\mathrm{sol}}_{FF}(t_i) - I^{\mathrm{sol,sim}}_{FF}(t_i)\right)^2. \tag{B.47}$$

Both deviations ΔC and ΔI are combined to give the total deviation $\Delta_{\mathrm{tot}} = \Delta C + \alpha \Delta I$, where α is a weighting factor which is chosen so that ΔC and $\alpha \Delta I$ are approximately of the same size. Δ_{tot} is minimized via the Nelder-Mead algorithm. If the discrepancy between ΔC and $\alpha \Delta I$ becomes more than a factor of 2, then α is adjusted and the minimization procedure is continued with the new value of α until convergence is achieved. Statistical errors are estimated by bootstrapping with 24 trajectory segments per system, where the fits are repeated for each bootstrap sample. The parameters and errors for the $L = 4.5\,\mathrm{nm}$ system are collected in Table B.1.

In Chapter 3 it is mentioned that the sum of two stretched exponential functions is sufficient to fit the data for $K \leq 250\,\mathrm{kJ/(mol\,nm^2)}$ and $K \geq 250,000\,\mathrm{kJ/(mol\,nm^2)}$. Here, we compare the fits obtained for $n = 2$ and $n = 3$ stretched exponentials for $K = 250\,\mathrm{kJ/(mol\,nm^2)}$, $K = 25,000\,\mathrm{kJ/(mol\,nm^2)}$ and $K = 250,000\,\mathrm{kJ/(mol\,nm^2)}$. The comparison of the solvent force autocorrelation functions $C^{\mathrm{sol}}_{FF}(t)$ and the memory kernels $\Gamma(t)$ are shown in Fig. B.8(a) and (b) respectively. Clearly, the differences between $n = 2$ and $n = 3$ are negligible for $K = 250\,\mathrm{kJ/(mol\,nm^2)}$ and $K = 250,000\,\mathrm{kJ/(mol\,nm^2)}$. For $K = 25,000\,\mathrm{kJ/(mol\,nm^2)}$ the figure shows that two

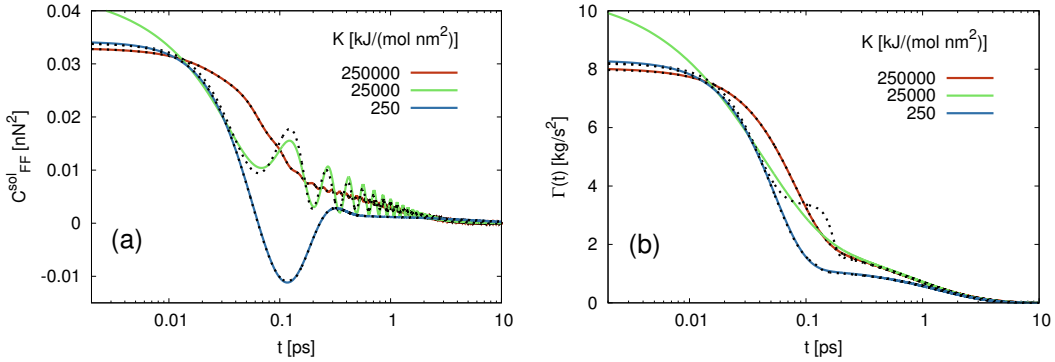

Figure B.8.: (a) Comparison of the solvent force autocorrelation functions $C^{\mathrm{sol}}_{FF}(t)$ computed from fit functions with $n = 2$ (solid colored lines) and $n = 3$ (dotted black lines) in a log-lin representation for $K = 250\,\mathrm{kJ/(mol\,nm^2)}$, $K = 25,000\,\mathrm{kJ/(mol\,nm^2)}$ and $K = 250,000\,\mathrm{kJ/(mol\,nm^2)}$. (b) Comparison of the respective memory kernels $\Gamma(t)$.

stretched exponentials are not sufficient to achieve agreement of the analytic predictions with the correlation functions from the simulation.

To demonstrate that the exponents α_i have significant influence on the quality of the fits, we compare in Fig. B.9 the solvent force autocorrelation functions $C^{\mathrm{sol}}_{FF}(t)$ and the respective running integrals $I^{\mathrm{sol}}_{FF}(t)$ for $K = 25,000\,\mathrm{kJ/(mol\,nm^2)}$ computed from the methane simulations in the $L = 4.5\,\mathrm{nm}$ box to the predictions obtained from fits with $n = 3$, but constrained exponents: (a) no contraints, (b) $\alpha_1 = 2$, $\alpha_3 = 1$ (α_2 free), (c) $\alpha_1 = 2$, $\alpha_2 = \alpha_3 = 1$, (d) $\alpha_1 = \alpha_3 = 1$ (α_2 free) and (e) $\alpha_1 = \alpha_2 = \alpha_3 = 1$. The obtained fit parameters and the resulting deviations ΔC and ΔI are shown in Table B.2. Clearly, the agreement is poor for (c), (d) and (e), which shows that the exponents α_i are important fit parameters. The best agreement for a constrained fit is achieved for (b) $\alpha_1 = 2$, $\alpha_3 = 1$ (α_2 free), but the deviation ΔC is still five times as large as for the unconstrained fit (a). The fit (b) yields the estimate $\alpha_2 = 7.7$, which is similar to the value $\alpha_2 = 9.8$ obtained from the unconstrained fit. Thus, we conclude that also the high value of α_2 is robust.

B.11. Comparison to an NVE Simulation

To exclude a systematic error introduced by the thermostat, we compare in Fig. B.10 the solvent force autocorrelation functions $C^{\mathrm{sol}}_{FF}(t)$ for $K = 25\,\mathrm{kJ/(mol\,nm^2)}$ and $K = 2,500\,\mathrm{kJ/(mol\,nm^2)}$ calculated from the NVT simulations to the respective correlation functions calculated from 32 NVE trajectories with a length of 2 ns each. For both values of K, they show perfect agreement.

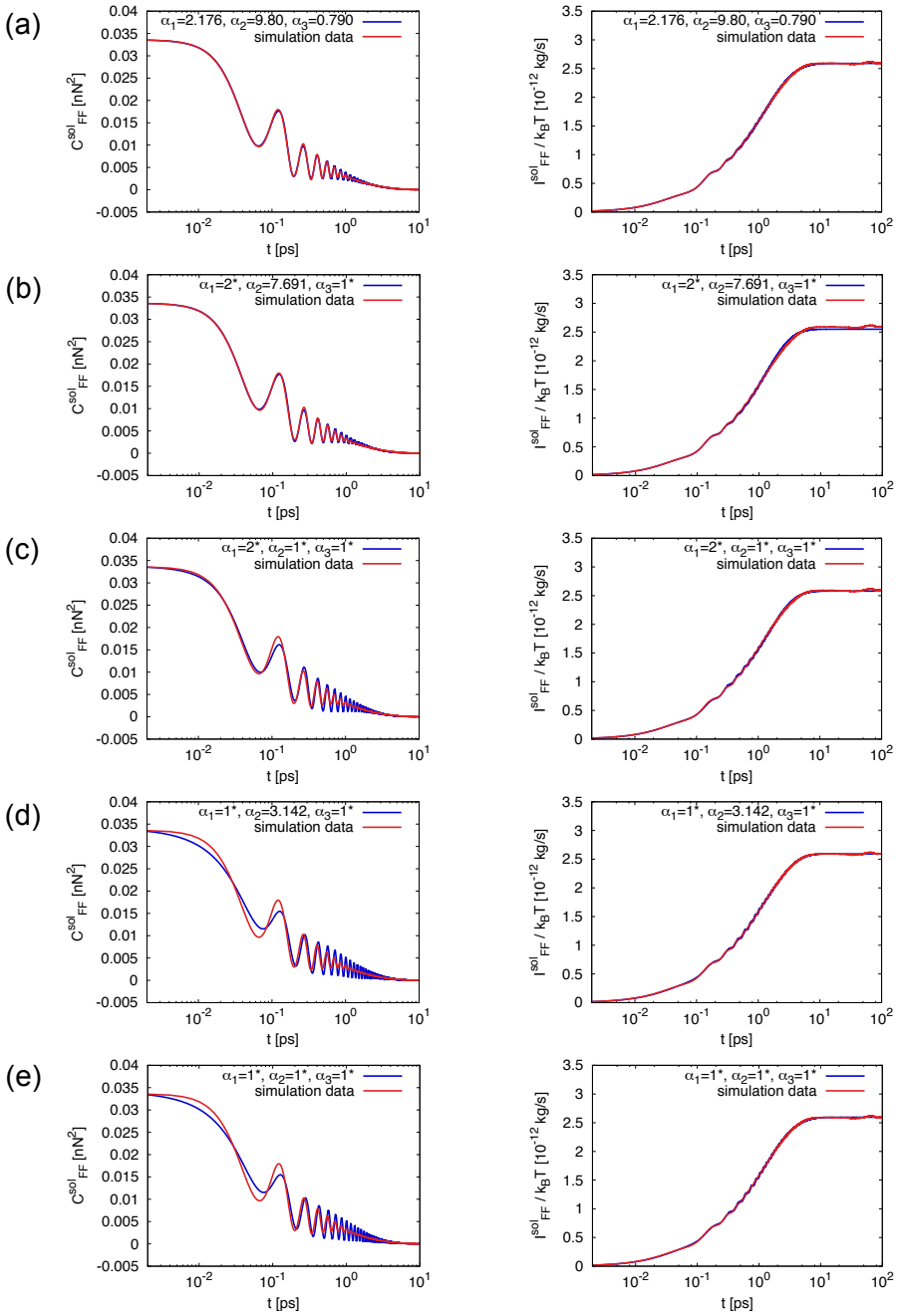

Figure B.9.: Comparison of the solvent force autocorrelation functions $C_{FF}^{\mathrm{sol}}(t)$ (left) and the integrals $I_{FF}^{\mathrm{sol}}(t)$ (right) for $K = 25,000\,\mathrm{kJ/(mol\,nm^2)}$ predicted from fits with $n = 3$, but constrained exponents, and the simulation results for methane in the $L = 4.5\,\mathrm{nm}$ box. All exponents α_i are given in the legends, the constrained values are indicated by stars (*). For reference, the unconstrained fit is shown in (a).

K	A_1	α_1	τ_1
∞	6.030 ± 0.046	1.446 ± 0.007	0.07489 ± 0.00007
250000	5.593 ± 0.095	1.583 ± 0.019	0.07974 ± 0.00023
100000	5.501 ± 0.208	0.8617 ± 0.015	0.05280 ± 0.00133
25000	4.489 ± 0.028	2.176 ± 0.010	0.03827 ± 0.00002
10000	5.252 ± 0.042	2.127 ± 0.014	0.04352 ± 0.00004
2500	6.345 ± 0.030	1.819 ± 0.007	0.04956 ± 0.00007
1000	6.855 ± 0.010	1.682 ± 0.002	0.05188 ± 0.00002
250	7.101 ± 0.017	1.608 ± 0.003	0.05330 ± 0.00003
100	7.029 ± 0.060	1.614 ± 0.008	0.05341 ± 0.00003
25	7.180 ± 0.005	1.590 ± 0.001	0.05364 ± 0.00002
K	A_2	α_2	τ_2
∞	–	–	–
250000	–	–	–
100000	1.269 ± 0.019	18.22 ± 0.41	0.0982 ± 0.0001
25000	1.589 ± 0.025	9.80 ± 0.16	0.1714 ± 0.0001
10000	0.861 ± 0.027	12.75 ± 0.48	0.2335 ± 0.0003
2500	0.3265 ± 0.011	13.34 ± 0.56	0.3367 ± 0.0006
1000	0.1418 ± 0.008	10.52 ± 0.62	0.3954 ± 0.0030
250	–	–	–
100	–	–	–
25	–	–	–
K	A_3	α_3	τ_3
∞	2.252 ± 0.046	0.770 ± 0.014	0.846 ± 0.025
250000	2.469 ± 0.110	0.696 ± 0.025	0.727 ± 0.48
100000	2.180 ± 0.176	0.756 ± 0.043	0.851 ± 0.088
25000	2.127 ± 0.062	0.790 ± 0.025	0.894 ± 0.036
10000	2.134 ± 0.080	0.756 ± 0.029	0.878 ± 0.051
2500	1.636 ± 0.045	0.902 ± 0.033	1.205 ± 0.044
1000	1.310 ± 0.015	1.050 ± 0.028	1.525 ± 0.021
250	1.202 ± 0.017	0.975 ± 0.050	1.371 ± 0.039
100	1.292 ± 0.061	0.792 ± 0.101	1.033 ± 0.117
25	1.129 ± 0.003	1.228 ± 0.663	1.390 ± 0.020

Table B.1.: Fit parameters for $\Gamma(t)$ for the system size $L = 4.5\,\mathrm{nm}$. A_i is given in $\mathrm{kg/s^2}$, τ_i in ps.

	(a)	(b)	(c)	(d)	(e)
A_1	4.489	4.579	3.434	6.828	6.595
α_1	2.176	2*	2*	1*	1*
τ_1	0.03827	0.03899	0.04179	0.07589	0.07281
A_2	1.589	1.868	3.396	0.3234	1.236
α_2	9.80	7.691	1*	3.142	1*
τ_2	0.1714	0.1713	0.1488	0.9677	0.9385
A_3	2.127	1.703	1.360	1.158	0.4826
α_3	0.790	1*	1*	1*	1*
τ_3	0.894	1.228	1.4364	1.549	1.979
ΔC	143.7	1845	2435	6124	6170
ΔI	287.4	232.8	7585	65943	68116

Table B.2.: Fit parameters for $\Gamma(t)$ with constrained exponents for $K = 25,000\,\mathrm{kJ/(mol\,nm^2)}$ and system size $L = 4.5\,\mathrm{nm}$. A_i is given in $\mathrm{kg/s^2}$, τ_i in ps. In addition, the deviations ΔC and ΔI are given in arbitrary units. Constrained values are indicated by a star (*). For reference, we show the fit parameters without constraints in the first column.

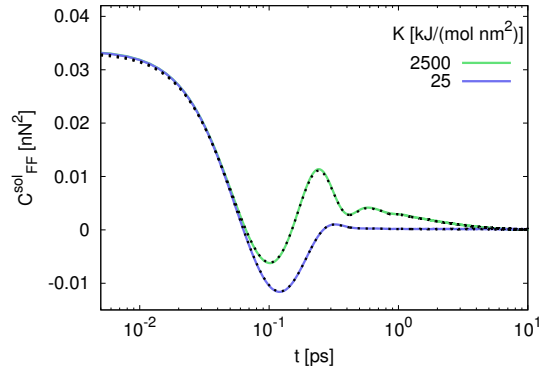

Figure B.10.: Comparison of the solvent force autocorrelation functions $C^{\mathrm{sol}}_{FF}(t)$ calculated in the NVT (solid lines) and in the NVE (dotted lines) ensemble for two selected values of K.

Appendix C

Mass-Dependent Solvent Friction of a Hydrophobic Molecule

C.1. Solvent Center-of-Mass Motion in Finite Simulation Boxes

For large solute masses m that reach the same order of magnitude than the *total* mass M_{sol} of the solvent, the mean-square displacement (MSD) relative to the solvent, which is used for the analysis in this project, differs from the absolute MSD: Conservation of momentum implies

$$m\dot{\boldsymbol{x}} + M_{\mathrm{sol}}\dot{\boldsymbol{x}}_{\mathrm{sol}} = \boldsymbol{p}_{\mathrm{total}} = \boldsymbol{0}, \tag{C.1}$$

where $\boldsymbol{x}$ denotes the solute position and $\boldsymbol{x}_{\mathrm{sol}}$ refers to the center of mass of the solvent. Eq. (C.1) is equivalent to

$$m\dot{\boldsymbol{x}} = -M_{\mathrm{sol}}\dot{\boldsymbol{x}}_{\mathrm{sol}}, \tag{C.2}$$

and integration yields

$$m(\boldsymbol{x}(t) - \boldsymbol{x}(0)) = -M_{\mathrm{sol}}(\boldsymbol{x}_{\mathrm{sol}}(t) - \boldsymbol{x}_{\mathrm{sol}}(0)). \tag{C.3}$$

Therefore, we have

$$\boldsymbol{x}_{\mathrm{sol}}(t) - \boldsymbol{x}_{\mathrm{sol}}(0) = -\frac{m}{M_{\mathrm{sol}}}(\boldsymbol{x}(t) - \boldsymbol{x}(0)), \tag{C.4}$$

which implies for the MSD relative to the solvent

$$\left\langle (\boldsymbol{x}(t) - \boldsymbol{x}(0))^2 \right\rangle_{\mathrm{rel}} \equiv \left\langle ((\boldsymbol{x}(t) - \boldsymbol{x}(0)) - (\boldsymbol{x}_{\mathrm{sol}}(t) - \boldsymbol{x}_{\mathrm{sol}}(0)))^2 \right\rangle \tag{C.5}$$

$$= \left\langle \left((\boldsymbol{x}(t) - \boldsymbol{x}(0)) + \frac{m}{M_{\mathrm{sol}}}(\boldsymbol{x}(t) - \boldsymbol{x}(0)) \right)^2 \right\rangle \tag{C.6}$$

$$= \left(1 + \frac{m}{M_{\mathrm{sol}}} \right)^2 \left\langle (\boldsymbol{x}(t) - \boldsymbol{x}(0))^2 \right\rangle. \tag{C.7}$$

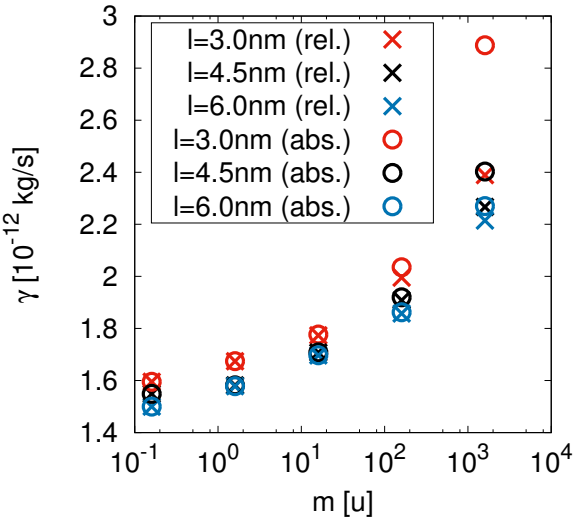

Figure C.1.: The friction coefficients γ obtained from the mean-square displacements (MSDs) relative to the solvent (crosses) are compared to to the friction coefficients determined from the absolute MSDs (circles) for the three system sizes.

In Fig. C.1, we compare the friction coefficients calculated from the MSDs relative to the solvent to the absolute MSDs. For the smallest system ($l = 3.0\,\mathrm{nm}$) and the largest mass ($m = 1600\,\mathrm{u}$) the difference is quite significant, in the other scenarios, which include all data points for the $l = 4.5\,\mathrm{nm}$ system on which most of the analysis in Chapter 4 is based, the correction to this finite-size effect is rather small.

C.2. Timescales and Fit Parameters

The fit parameters A_i and τ_i of the memory kernels

$$\Gamma(t) = \sum_{i=1}^{3} A_i \exp\left(-|t|/\tau_i\right) \tag{C.8}$$

are given in Table C.1, and the timescales τ_1 and τ_2, which correspond to positive amplitudes A_i, are shown in Fig. C.2 as a function of solute mass m. Whereas the timescale τ_1 significantly depends on m, the timescale τ_2 is rather constant. We remark that the arguments used in Chapter 3 to explain the shortest decay time of (free and frozen) methane in water suggest that the dependence of τ_1 on the solute mass m is caused by the change of the reduced mass

$$m_\mathrm{r} = \frac{m m_{\mathrm{H_2O}}}{m + m_{\mathrm{H_2O}}}, \tag{C.9}$$

where $m_{\mathrm{H_2O}}$ denotes the mass of a water molecule.

m [u]	A_1 [kg/s^2]	τ_1 [fs]	A_2 [kg/s^2]	τ_2 [fs]	A_3 [kg/s^2]	τ_3 [fs]
∞	9.8	57.6	1.7	1231	-3.2	18.5
1600	10.1	55.5	1.7	1044	-3.4	18.7
160	9.7	60.2	1.2	1138	-2.5	15.4
16	52.5	26.6	0.9	1425	-45.0	22.8
1.6	85.4	9.4	1.4	1057	-78.0	8.6
0.16	70.1	2.7	1.8	830	-62.3	2.4

Table C.1.: The parameters for the memory kernels for the $l = 4.5\,\mathrm{nm}$ system obtained by fitting the prediction Eq. (4.4) to the simulated force autocorrelation functions using the parametrization Eq. (C.8).

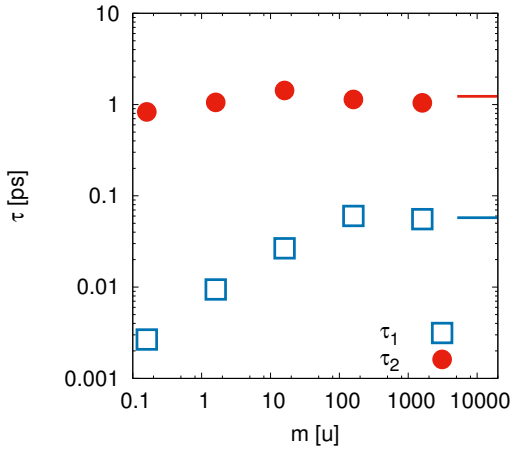

Figure C.2.: The timescales τ_1 and τ_2 given in Table C.1 as a function of solute mass m. The infinite mass limit is represented by horizontal lines.

Appendix D

Butane Dihedral Angle Dynamics in Water is Dominated by Internal Friction

D.1. Derivation of the Iteration Equation for the Memory Kernel

We start from the generalized Langevin equation (GLE)

$$m\ddot{x}(t) = -\int_0^t dt'\,\Gamma(t')\dot{x}(t-t') - \nabla U[x(t)] + F_R(t), \tag{D.1}$$

where $F_R(t)$ denotes the random force, which obeys

$$\left\langle F_R(t)F_R(t')\right\rangle = k_\mathrm{B}T\,\Gamma\left(t-t'\right). \tag{D.2}$$

Multiplication by $\dot{x}(0)$ and averaging yields

$$m\left\langle \dot{x}(0)\ddot{x}(t)\right\rangle = -\int_0^t dt'\,\Gamma(t')\left\langle \dot{x}(0)\dot{x}(t-t')\right\rangle - \left\langle \dot{x}(0)\nabla U[x(t)]\right\rangle, \tag{D.3}$$

where we use that the random force $F_R(t)$ at time t is not correlated with the initial velocity $\dot{x}(0)$ [60]. All correlation functions appearing in Eq. (D.3) can be obtained from trajectories. Clearly, this is straightforward for $\langle\dot{x}(0)\ddot{x}(t)\rangle$ and $\langle\dot{x}(0)\dot{x}(t)\rangle$. For the calculation of the correlation function $\langle\dot{x}(0)\nabla U[x(t)]\rangle$, we use that the GLE Eq. (D.1) implies that $U(x)$ is equal to the free energy, i.e. $U(x) = -k_\mathrm{B}T\log p(x)$, where $p(x)$ denotes the equilibrium probability distribution of the reaction coordinate x. We interpolate $U(x)$ with cubic splines and directly calculate the correlation function $\langle\dot{x}(0)\nabla U[x(t)]\rangle$ from the trajectory. Eq. (D.3) can now be discretized and solved numerically. Defining

$$\Gamma_i = \Gamma(i\Delta t), \tag{D.4}$$

$$C_i^{\dot{x}\dot{x}} = \left\langle \dot{x}(0)\dot{x}(i\Delta t)\right\rangle, \tag{D.5}$$

$$C_i^{\dot{x}\ddot{x}} = \left\langle \dot{x}(0)\ddot{x}(i\Delta t)\right\rangle, \tag{D.6}$$

$$C_i^{\dot{x}\nabla U} = \left\langle \dot{x}(0)\nabla U[x(i\Delta t)]\right\rangle, \tag{D.7}$$

the discretized version of Eq. (D.3) reads

$$mC_i^{\dot{x}\ddot{x}} = -\sum_{j=0}^{i} \omega_{i,j} \Delta t \Gamma_j C_{i-j}^{\dot{x}\dot{x}} - C_i^{\dot{x}\nabla U}, \tag{D.8}$$

where we discretized the integral using the integration weight $w_{i,j} = 1 - \delta_{i,0}/2 - \delta_{i,j}/2$ of the trapezoidal rule. Solving for Γ_i yields the iteration relation for the memory kernel Eq. (5.3):

$$\Gamma_i = -\frac{1}{\omega_{i,i} \Delta t C_0^{\dot{x}\dot{x}}} \left(\sum_{j=0}^{i-1} \omega_{i,j} \Delta t \Gamma_j C_{i-j}^{\dot{x}\dot{x}} + mC_i^{\dot{x}\ddot{x}} + C_i^{\dot{x}\nabla U} \right). \tag{D.9}$$

We note that for $U(x) = 0$ this result is equal to the previously derived equation [73].

D.2. Application to a Model System

To demonstrate that the iteration relation (D.9) is numerically robust, we reconstruct the memory kernel from simulated GLE trajectories in a doublewell potential (see Fig. D.1(a))

$$U(x) = U_0 \left((x/L)^2 - 1 \right)^2, \tag{D.10}$$

with $U_0 = 1\, k_\mathrm{B}T$. We use the single-exponential memory kernel

$$\Gamma(t) = \frac{\gamma}{\tau_\Gamma} \exp\left(-\frac{t}{\tau_\Gamma} \right), \tag{D.11}$$

where the memory time τ_Γ is set to $\tau_\Gamma = \tau_D = L^2\gamma/k_\mathrm{B}T$. For the mass, we use $\tau_m = \tau_D$, where $\tau_m = m/\gamma$. The simulation is carried out by introducing an additional variable $R(t)$ that obeys [291]

$$\dot{R}(t) = -\frac{1}{\tau_\Gamma} R(t) - \frac{\gamma}{\tau_\Gamma} \dot{x}(t) + \xi(t), \tag{D.12}$$

with δ-correlated noise

$$\left\langle \xi(t)\xi(t') \right\rangle = \frac{2k_\mathrm{B}T\gamma}{\tau_\Gamma^2} \delta(t - t'). \tag{D.13}$$

The GLE Eq. (D.1) can then be written as

$$m\ddot{x}(t) = R(t) - \nabla U(x(t)), \tag{D.14}$$

and the Eqs. (D.12)–(D.14) are numerically integrated using a standard integration scheme. We simulate a trajectory of length $10^6\, \tau_D$, where an initial equilibration time is omitted for the analysis. A typical trajectory is depicted in Fig. D.1(b). In Figs. D.1(c) and (d), we compare the memory kernel reconstructed from the trajectories using Eq. (D.9) to the analytic simulation input given by Eq. (D.11). Within statistical errors, they show perfect agreement on linear and logarithmic scales.

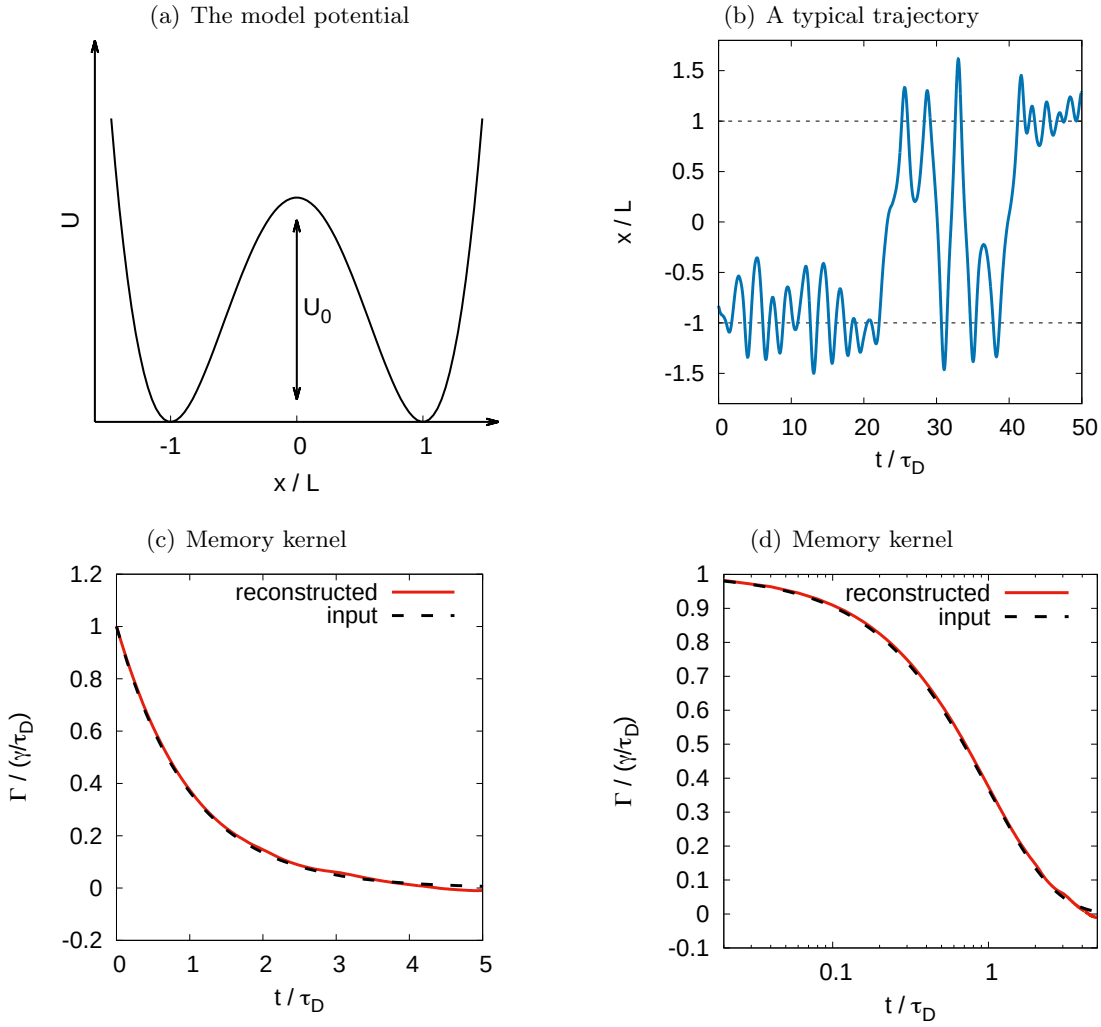

Figure D.1.: (a) The model potential. (b) A typical trajectory. (c) and (d) The reconstructed memory kernel (red line) compared to the analytic input used for the simulation (dashed black line).

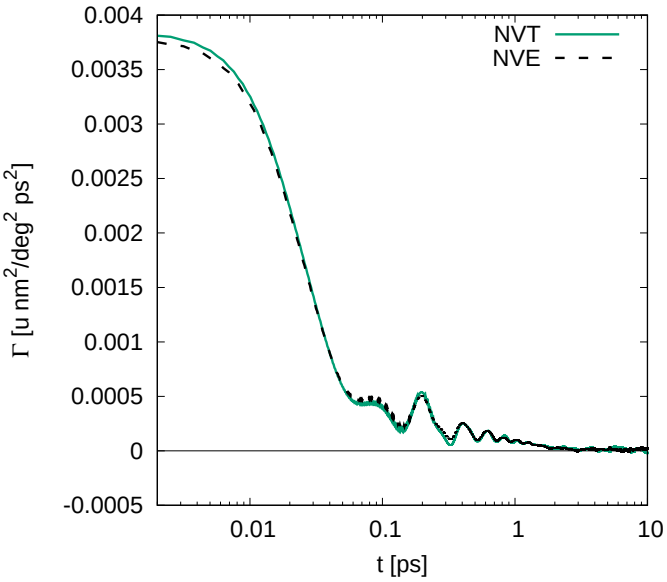

Figure D.2.: Comparison of the memory kernels for free butane calculated from an NVT (green line) and from an NVE (dashed black line) simulation at a solvent viscosity of $\eta/\eta_0 = 0.3$.

D.3. Influence of Ensemble and Thermostat

To show that the thermostat does not influence the memory kernel, we compare the memory kernel extracted from the NVT simulation of free water-solvated butane at a viscosity of $\eta/\eta_0 = 0.3$ to the memory kernel obtained from an NVE simulation with the same length. The comparison is shown in Fig. D.2. From the similarity of the two memory kernels we conclude that the influence of the ensemble and the thermostat is negligible.

D.4. Estimation of the Friction Constant γ

The inversion of the Volterra Eq. (D.3) using the iteration scheme (D.9) is subject to numerical and statistical errors, in particular for large t. For an estimate of the friction constant we thus fit the long time tail ($t > 2\,\text{ps}$ for free butane and $t > 2(\eta/\eta_0)\,\text{ps}$ for constrained butane) by an exponential function before integrating over the curve. In Figs. D.3–D.6 we show the memory kernels together with the exponential fits to the long-time tail for free (Figs. D.3 and D.4) and constrained (Figs. D.5 and D.6) butane, both in a lin-log (Figs. D.3 and D.5) and in a log-log (Figs. D.4 and D.6) representation. A small systematic error is introduced by this procedure, but the magnitude of the estimated friction constant is expected to be correct, since the differences are small.

The obtained friction constants

$$\gamma = \int_0^\infty dt\, \Gamma(t) \tag{D.15}$$

are shown as a function of solvent viscosity for both systems in Fig. 5.4.

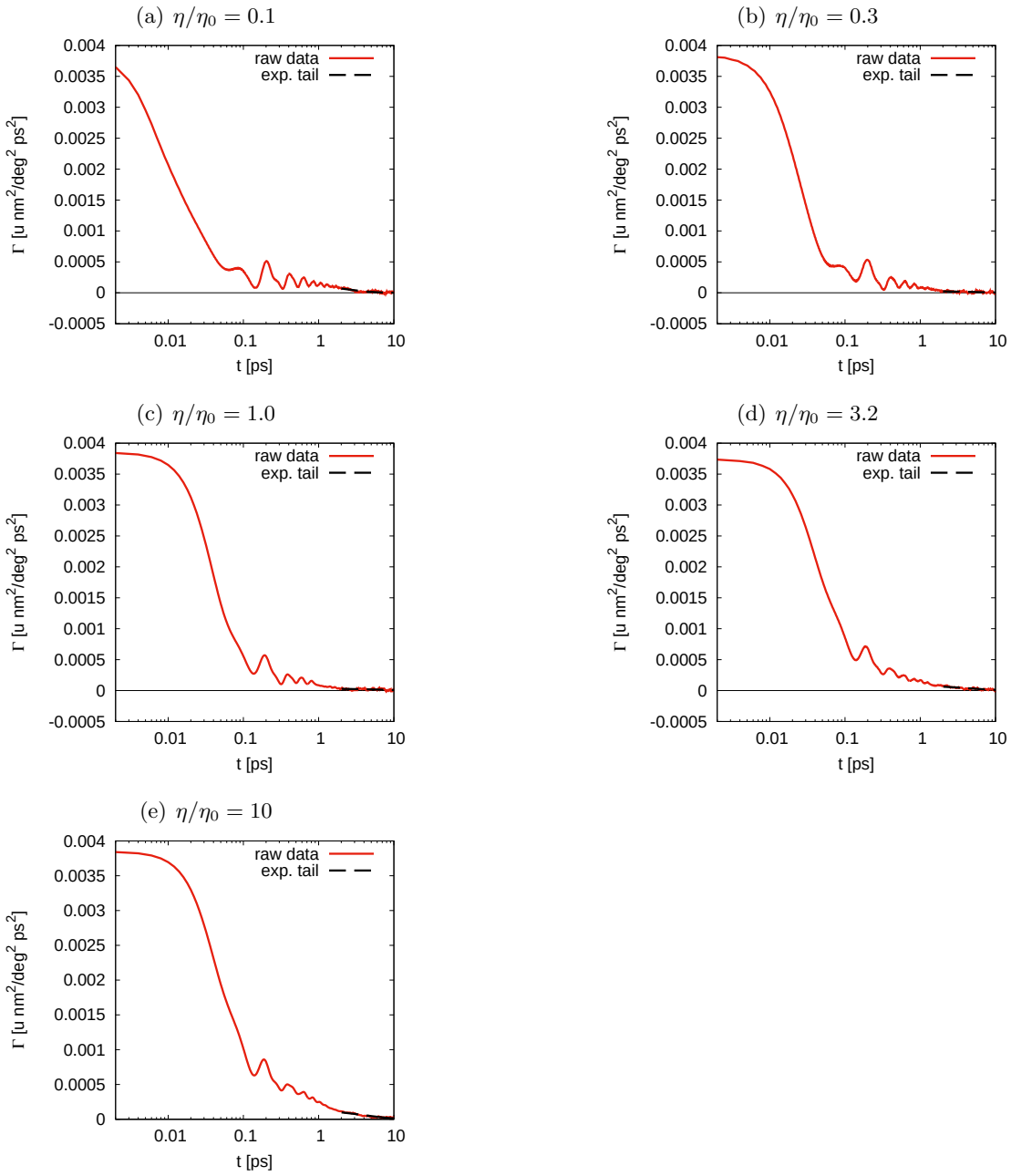

Figure D.3.: **Free butane, lin-log.** Comparison of the memory kernels computed using Eq. (D.9) (solid red lines) and the exponential fit to the long time tail $t > 2\,\mathrm{ps}$ (dashed black lines) shown in a lin-log representation.

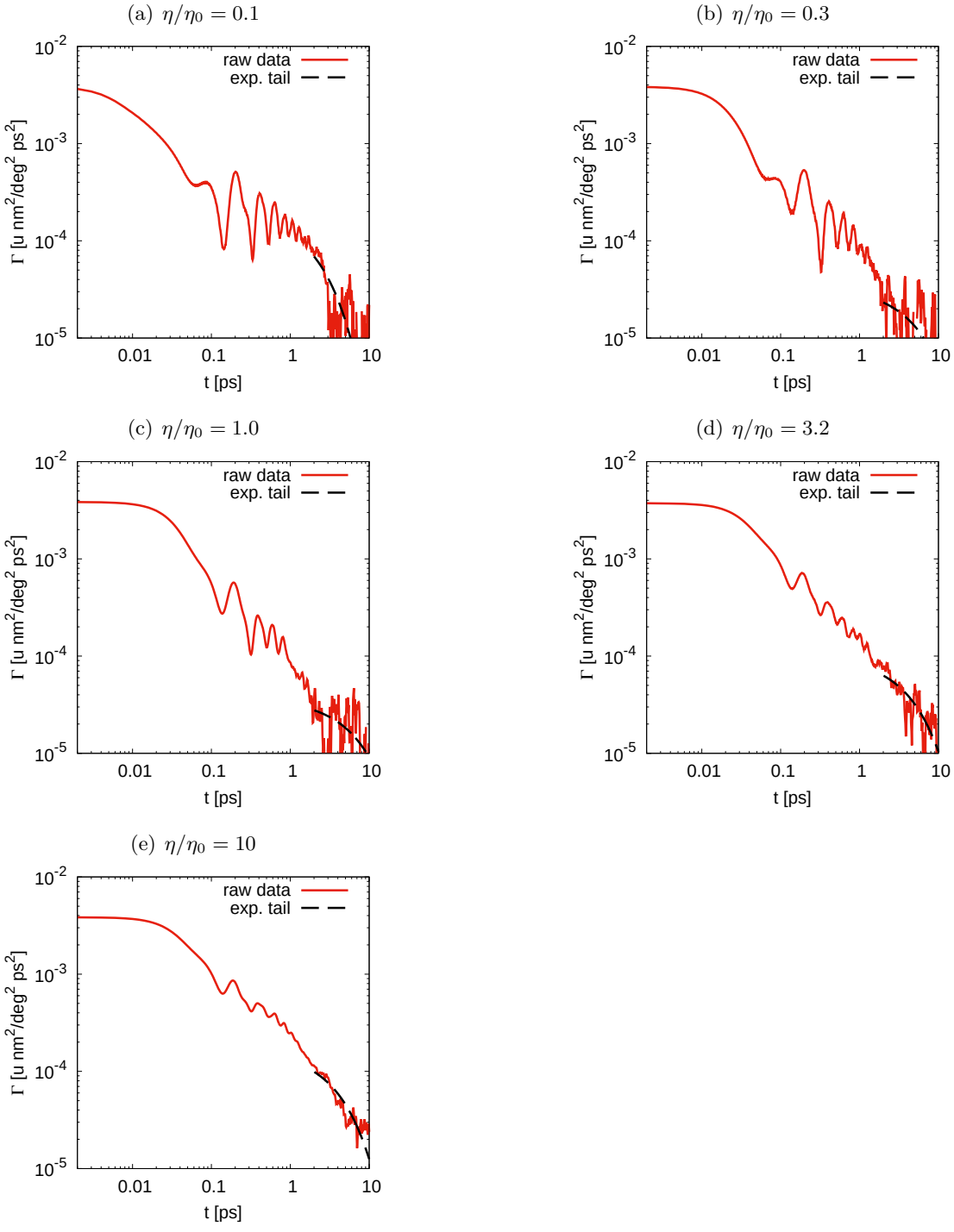

Figure D.4.: **Free butane, log-log.** Comparison of the memory kernels computed using Eq. (D.9) (solid red lines) and the exponential fit to the long time tail $t > 2\,\mathrm{ps}$ (dashed black lines) shown in a log-log representation.

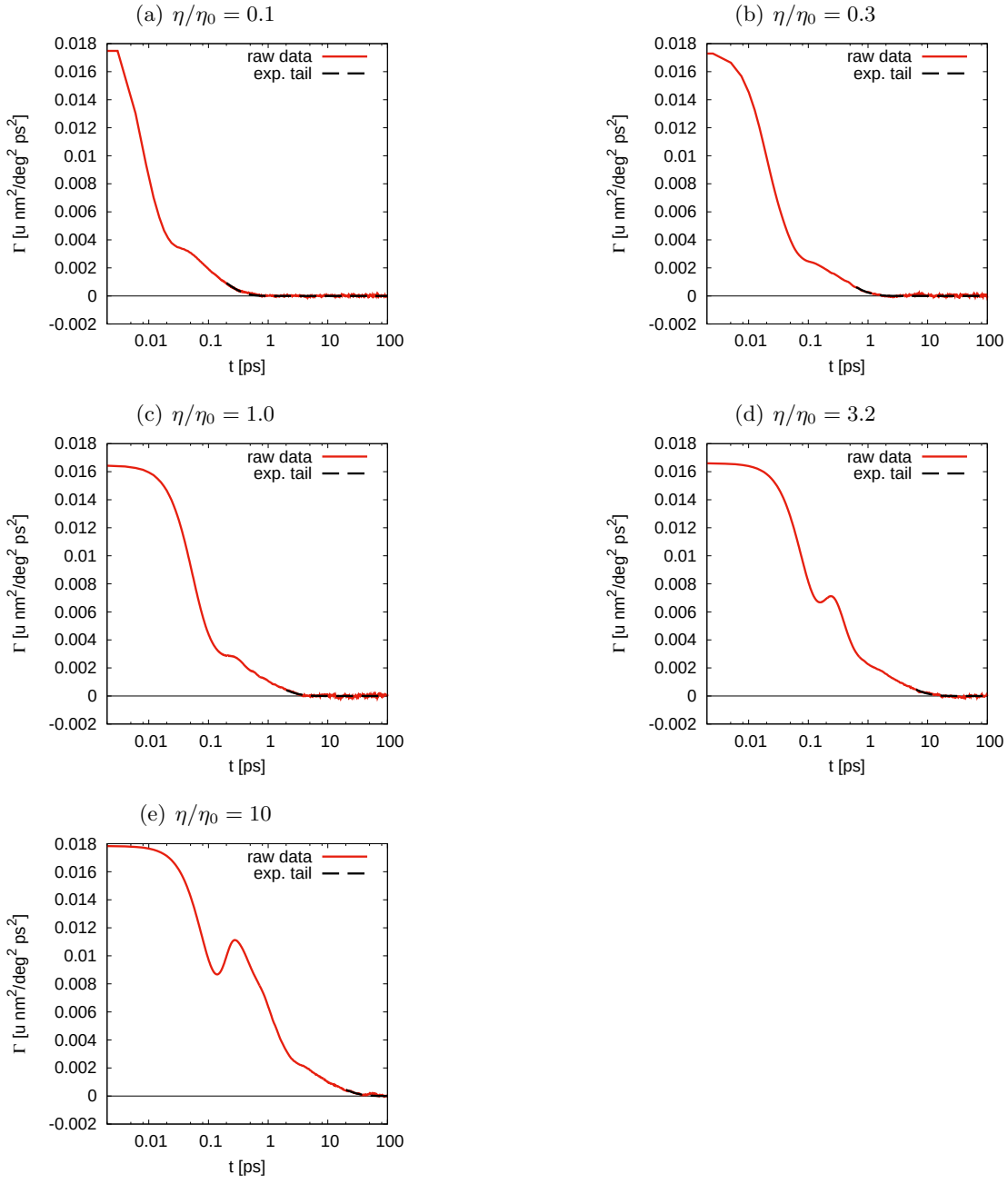

Figure D.5.: **Constrained butane, lin-log.** Comparison of the memory kernels computed using Eq. (D.9) (solid red lines) and the exponential fit to the long time tail $t > 2(\eta/\eta_0)$ ps (dashed black lines) shown in a lin-log representation.

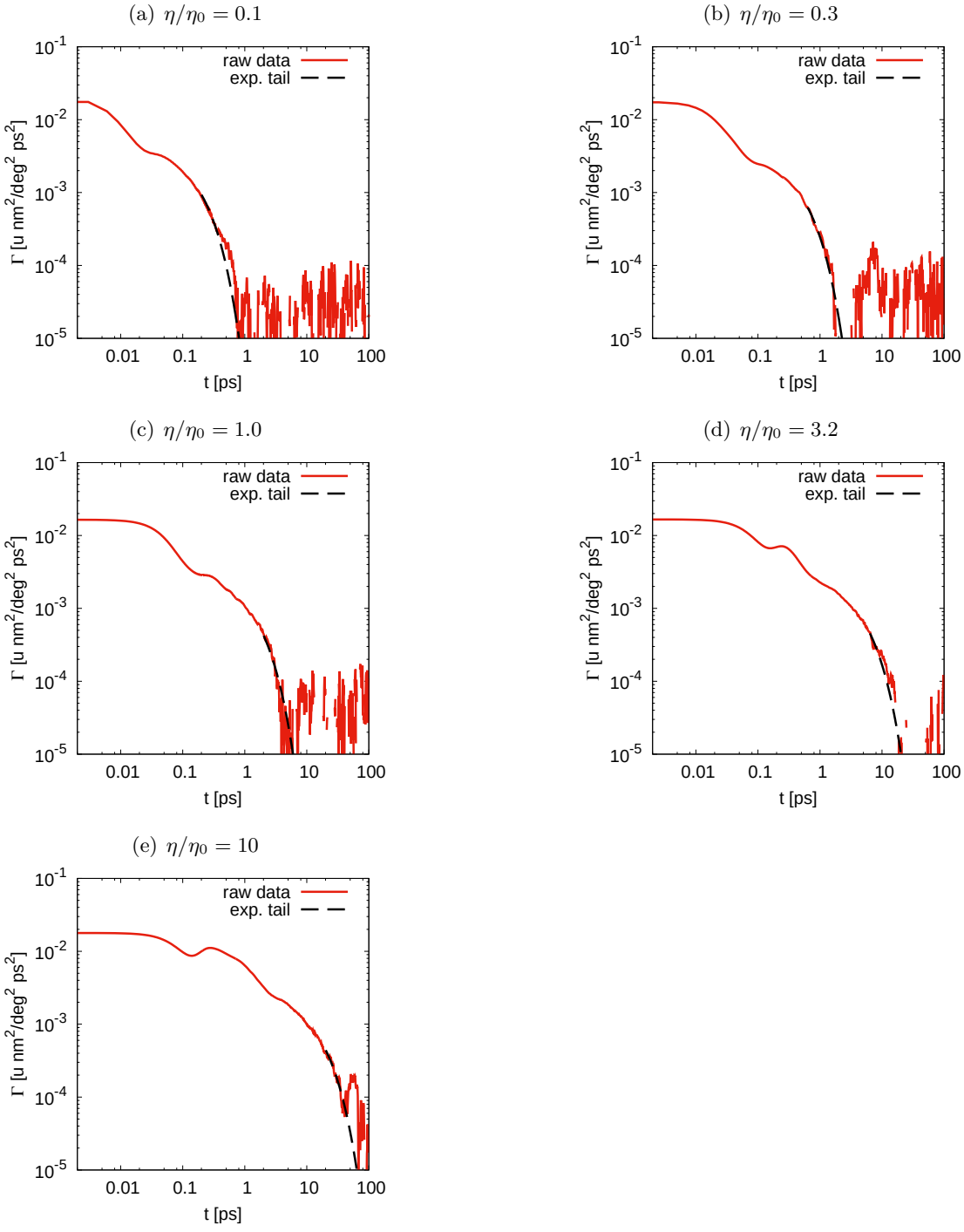

Figure D.6.: **Constrained butane, log-log.** Comparison of the memory kernels computed using Eq. (D.9) (solid red lines) and the exponential fit to the long time tail $t > 2(\eta/\eta_0)$ ps (dashed black lines) shown in a log-log representation.

Appendix E

Transition Paths Are Hot

E.1. Calculation of the Second Moment of Velocities

We evaluate the second moment of velocities explicitly for the equilibrium distribution, in order to illustrate our definition of an effective temperature. The calculation is straight-forward: based on the flux-weighted velocity distribution

$$P^{\mathrm{eq}}(v) \propto |v| \exp\left(-mv^2/2k_{\mathrm{B}}T\right), \tag{E.1}$$

we can write

$$\left\langle v^2(x_0)\right\rangle = \frac{\int_{-\infty}^{\infty} dv v^2 \, |v| \exp\left(-mv^2/2k_{\mathrm{B}}T\right)}{\int_{-\infty}^{\infty} dv \, |v| \exp\left(-mv^2/2k_{\mathrm{B}}T\right)} \tag{E.2}$$

$$= \frac{\int_{0}^{\infty} dv v^3 \exp\left(-mv^2/2k_{\mathrm{B}}T\right)}{\int_{0}^{\infty} dv v \exp\left(-mv^2/2k_{\mathrm{B}}T\right)} \tag{E.3}$$

$$= \frac{2(k_{\mathrm{B}}T/m)^2}{k_{\mathrm{B}}T/m} = 2k_{\mathrm{B}}T/m. \tag{E.4}$$

Thus,

$$k_{\mathrm{B}}T = \frac{1}{2} m \left\langle v^2(x_0)\right\rangle. \tag{E.5}$$

E.2. Estimation of the Effective Initial Transition Path Temperature for Small Masses

In this section, we present an approximative argument, supporting the numerical observation that also for small mass the initial effective temperature of transition paths is higher than the equilibrium temperature.

We estimate the effective temperature by assuming a flat potential $U = 0$, i.e. free diffusion. The solution $x(t)$ of the corresponding Langevin equation with an initial condition $v(0) = v_0$, $x(0) = x_\mathrm{A}$ obeys

$$\langle x(t)\rangle = x_\mathrm{A} + \frac{m}{\gamma}\left(1 - \exp\left\{-\frac{\gamma}{m}t\right\}\right)v_0, \tag{E.6}$$

$$\langle v(t)\rangle = \exp\left\{-\frac{\gamma}{m}t\right\}v_0. \tag{E.7}$$

Hence, for $t \gg \tau_m = m/\gamma$ we obtain

$$\langle x(t)\rangle = x_\mathrm{A} + \frac{m}{\gamma}v_0, \tag{E.8}$$

$$\langle v(t)\rangle = 0 \tag{E.9}$$

and the motion becomes purely diffusive.

Starting from this position, the probability to exit the interval at x_B is given by the splitting probability

$$\phi_\mathrm{B} = \frac{\langle x(t)\rangle - x_\mathrm{A}}{x_\mathrm{B} - x_\mathrm{A}} = \frac{mv_0}{\gamma\,(x_\mathrm{B} - x_\mathrm{A})} \equiv \phi_\mathrm{B}(v_0), \tag{E.10}$$

which obviously depends on the initial velocity v_0. Hence, in this approximation, the probability to be on a transition path is the product of the probability to enter the interval with a velocity v_0, which is given by the flux-weighted equilibrium distribution, times the probability to exit at x_B, i.e.

$$P^\mathrm{TP}(v_0) = P^\mathrm{eq}(v_0)\phi_\mathrm{B}(v_0). \tag{E.11}$$

Thus, we can directly compute the flux-weighted average of the squared velocity of transition paths at the initial position x_A

$$\left\langle v^2(x_\mathrm{A})\right\rangle^\mathrm{TP} = \frac{\int dv\, v^2 P^\mathrm{TP}(v)}{\int dv\, P^\mathrm{TP}(v)} = \frac{\int dv\, v^4 \exp\left\{-mv^2/2\right\}}{\int dv\, v^2 \exp\left\{-mv^2/2\right\}} = \frac{3k_\mathrm{B}T_\mathrm{eff}}{m} = \frac{3}{2}\left\langle v^2(x_\mathrm{A})\right\rangle, \tag{E.12}$$

where Eq. (E.5) was used in the last step. Therefore we conclude

$$T_\mathrm{eff}/T \approx \frac{3}{2}. \tag{E.13}$$

The result is somewhat larger than the actual value from the simulation $T_\mathrm{eff}/T \approx 1.3$, which is presumably caused by the drastic approximations employed in deriving Eq. (E.13). On the other hand, the calculation provides insight into how the distribution shifts even in the case of a small mass and suggests that the overdamped limit $m \to 0$ is singular.

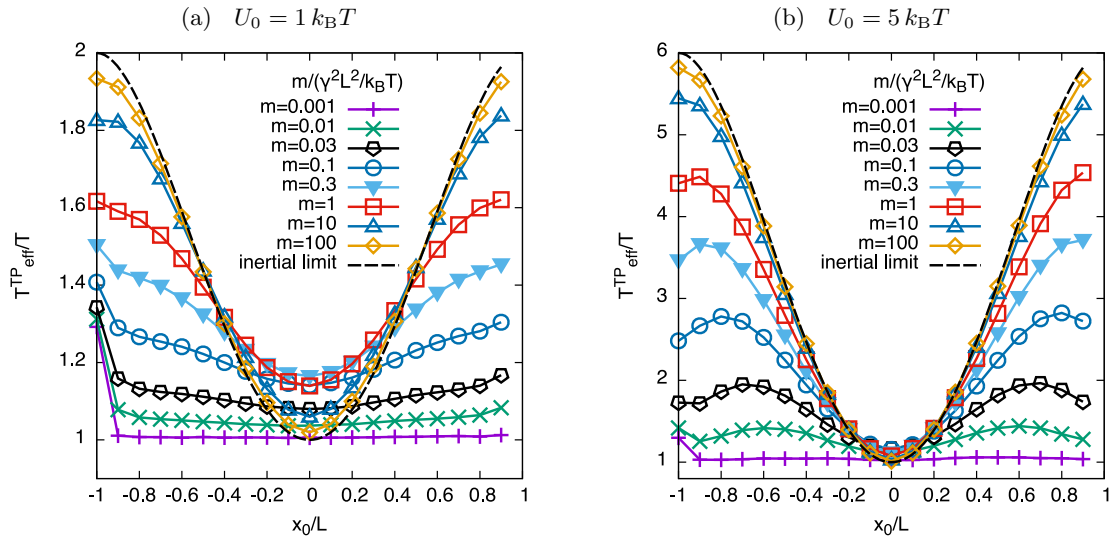

Figure E.1.: Effective transition path temperature $T^{\mathrm{TP}}_{\mathrm{eff}}$ as a function of position x_0 for different masses at fixed barrier heights of (a) $U_0 = 1\,k_{\mathrm{B}}T$ and (b) $U_0 = 5\,k_{\mathrm{B}}T$. The data points are connected by lines to guide the eye. The inertial limit is shown as a dashed line.

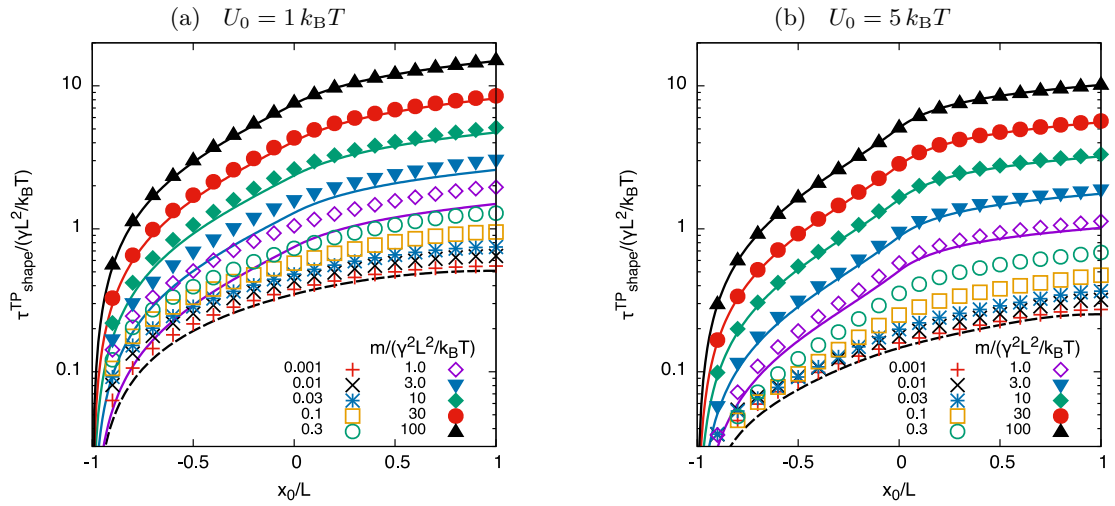

Figure E.2.: Mean transition path shapes $\tau^{\mathrm{TP}}_{\mathrm{shape}}(x_0|x_{\mathrm{A}})$ for the barrier heights (a) $U_0 = 1\,k_{\mathrm{B}}T$ and (b) $U_0 = 5\,k_{\mathrm{B}}T$ as a function of the position x_0 for different masses m. The overdamped limit is included as a dashed line, the inertial limit is shown as solid lines.

List of Publications

The present thesis is based on the following manuscripts, which have been published or are in preparation for publication in peer-reviewed journals:

[i] J. O. Daldrop, M. Saita, M. Heyden, V. A. Lorenz-Fonfria, J. Heberle, and R. R. Netz, *Orientation of non-spherical protonated water clusters revealed by infrared absorption dichroism*, Nature Communications **9**, 311 (2018). DOI: 10.1038/s41467-017-02669-9

[ii] J. O. Daldrop, B. G. Kowalik, and R. R. Netz, *External Potential Modifies Friction of Molecular Solutes in Water*, Physical Review X **7**, 041065 (2017). DOI: 10.1103/PhysRevX.7.041065

[iii] J. O. Daldrop and R. R. Netz, *Mass-Dependent Solvent Friction of a Hydrophobic Molecule*, in preparation (2018).

[iv] J. O. Daldrop, J. Kappler, F. N. Brünig, and R. R. Netz, *Butane dihedral angle dynamics in water is dominated by internal friction*, Proceedings of the National Academy of Sciences of the United States of America **115**, 5169 (2018). DOI: 10.1073/pnas.1722327115

[v] J. O. Daldrop, W. K. Kim, and R. R. Netz, *Transition paths are hot*, Europhysics Letters **113**, 18004 (2016). DOI: 10.1209/0295-5075/113/18004

The following publication is related to this thesis:

[vi] J. Kappler, J. O. Daldrop, F. N. Brünig, M. D. Boehle, and R. R. Netz, *Memory-induced acceleration and slowdown of barrier crossing*, The Journal of Chemical Physics **148**, 014903 (2018). DOI: 10.1063/1.4998239

The following publications are unrelated to this thesis:

[vii] J. Mortier, E. K. Nyakatura, O. Reimann, S. Huhmann, J. O. Daldrop, C. Baldauf, G. Wolber, M. S. Miettinen, and B. Koksch, *Coiled-Coils in Phage Display Screening: Insight into Exceptional Selectivity Provided by Molecular Dynamics*, Journal of Chemical Information and Modeling **55**, 495 (2015). DOI: 10.1021/ci500689c

[viii] C. Alexandrou, J. O. Daldrop, M. Dalla Brida, M. Gravina, L. Scorzato, C. Urbach, and M. Wagner (ETM Collaboration), *Lattice investigation of the scalar mesons $a_0(980)$ and κ using four-quark operators*, Journal of High Energy Physics **2013.4**, 137 (2013). DOI: 10.1007/JHEP04(2013)137

[ix] R. J. Dowdall, B. Colquhoun, J. O. Daldrop, C. T. H. Davies, I. D. Kendall, E. Follana, T. C. Hammant, R. R. Horgan, G. P. Lepage, C. J. Monahan, and E. H. Müller (HPQCD Collaboration), *The Upsilon spectrum and the determination of the lattice spacing from lattice QCD including charm quarks in the sea*, Physical Review D **85**, 054509 (2012). DOI: 10.1103/PhysRevD.85.054509

[x] J. O. Daldrop, C. T. H. Davies, and R. J. Dowdall (HPQCD Collaboration), *Prediction of the Bottomonium D-Wave Spectrum from Full Lattice QCD*, Physical Review Letters **108**, 102003 (2012). DOI: 10.1103/PhysRevLett.108.102003

Bibliography

[1] Y. Levy and J. N. Onuchic, *Water Mediation in Protein Folding and Molecular Recognition,* Annu. Rev. Biophys. Biomol. Struct. **35**, 389 (2006).

[2] B. Bagchi, *Water Dynamics in the Hydration Layer around Proteins and Micelles,* Chem. Rev. **105**, 3197 (2005).

[3] S. Ebbinghaus, S. J. Kim, M. Heyden, X. Yu, U. Heugen, M. Gruebele, D. M. Leitner, and M. Havenith, *An extended dynamical hydration shell around proteins,* Proc. Natl. Acad. Sci. U. S. A. **104**, 20749 (2007).

[4] F. Despa, A. Fernández, and R. S. Berry, *Dielectric Modulation of Biological Water,* Phys. Rev. Lett. **93**, 228104 (2004).

[5] P. W. Fenimore, H. Frauenfelder, B. H. McMahon, and R. D. Young, *Bulk-solvent and hydration-shell fluctuations, similar to α- and β-fluctuations in glasses, control protein motions and functions,* Proc. Natl. Acad. Sci. U. S. A. **101**, 14408 (2004).

[6] J. E. Straub, M. Borkovec, and B. J. Berne, *Calculation of dynamic friction on intramolecular degrees of freedom,* J. Phys. Chem. **91**, 4995 (1987).

[7] R. Zwanzig and A. K. Harrison, *Modifications of the Stokes–Einstein formula,* J. Chem. Phys. **83**, 5861 (1985).

[8] A. Soranno, B. Buchli, D. Nettels, R. R. Cheng, S. Müller-Späth, S. H. Pfeil, A. Hoffmann, E. A. Lipman, D. E. Makarov, and B. Schuler, *Quantifying internal friction in unfolded and intrinsically disordered proteins with single-molecule spectroscopy,* Proc. Natl. Acad. Sci. U. S. A. **109**, 17800 (2012).

[9] O. F. Lange and H. Grubmüller, *Collective Langevin dynamics of conformational motions in proteins,* J. Chem. Phys. **124**, 214903 (2006).

[10] A. Ansari, C. M. Jones, E. R. Henry, J. Hofrichter, and W. A. Eaton, *The role of solvent viscosity in the dynamics of protein conformational changes,* Science **256**, 1796 (1992).

[11] K. W. Plaxco and D. Baker, *Limited internal friction in the rate-limiting step of a two-state protein folding reaction,* Proc. Natl. Acad. Sci. U. S. A. **95**, 13591 (1998).

[12] B. Alberts, D. Bray, K. Hopkin, A. D. Johnson, K. Roberts, and J. Lewis, *Essential Cell Biology*, 4th ed. (Taylor & Francis Ltd., New York, 2013).

[13] F. H. Stillinger, *Water Revisited,* Science **209**, 451 (1980).

[14] D. Laage and J. T. Hynes, *A Molecular Jump Mechanism of Water Reorientation,* Science **311**, 832 (2006).

[15] D. Laage, G. Stirnemann, F. Sterpone, R. Rey, and J. T. Hynes, *Reorientation and Allied Dynamics in Water and Aqueous Solutions,* Annu. Rev. Phys. Chem. **62**, 395 (2011).

[16] D. Marx, M. E. Tuckerman, J. Hutter, and M. Parrinello, *The nature of the hydrated excess proton in water,* Nature **397**, 601 (1999).

[17] D. Marx, *Proton Transfer 200 Years after von Grotthuss: Insights from Ab Initio Simulations,* ChemPhysChem **7**, 1848 (2006).

[18] T. Norby, *Solid-state protonic conductors: principles, properties, progress and prospects,* Solid State Ionics **125**, 1 (1999).

[19] S. C. Sahoo, T. Kundu, and R. Banerjee, *Helical Water Chain Mediated Proton Conductivity in Homochiral Metal–Organic Frameworks with Unprecedented Zeolitic unh-Topology,* J. Am. Chem. Soc. **133**, 17950 (2011).

[20] C. Dreßler, G. Kabbe, and D. Sebastiani, *Insight from Atomistic Simulations of Protonation Dynamics at the Nanoscale,* Fuel Cells **16**, 682 (2016).

[21] K. A. Dill and J. L. MacCallum, *The Protein-Folding Problem, 50 Years On,* Science **338**, 1042 (2012).

[22] W. Kuhn and H. Kuhn, *Bedeutung beschränkt freier Drehbarkeit für die Viskosität und Strömungsdoppelbrechung von Fadenmolekellösungen I,* Helv. Chim. Acta **28**, 1533 (1945).

[23] W. Kuhn and H. Kuhn, *Bedeutung beschränkt freier Drehbarkeit für die Viskosität und Strömungsdoppelbrechung von Fadenmolekellösungen II,* Helv. Chim. Acta **29**, 71 (1946).

[24] P.-G. de Gennes, *Scaling Concepts in Polymer Physics* (Cornell University Press, Ithaca, 1979).

[25] G. S. Jas, W. A. Eaton, and J. Hofrichter, *Effect of Viscosity on the Kinetics of α-Helix and β-Hairpin Formation,* J. Phys. Chem. B **105**, 261 (2001).

[26] S. A. Pabit, H. Roder, and S. J. Hagen, *Internal Friction Controls the Speed of Protein Folding from a Compact Configuration,* Biochemistry **43**, 12532 (2004).

[27] L. Qiu and S. J. Hagen, *A Limiting Speed for Protein Folding at Low Solvent Viscosity,* J. Am. Chem. Soc. **126**, 3398 (2004).

[28] T. Cellmer, E. R. Henry, J. Hofrichter, and W. A. Eaton, *Measuring internal friction of an ultrafast-folding protein,* Proc. Natl. Acad. Sci. U. S. A. **105**, 18320 (2008).

[29] B. G. Wensley, S. Batey, F. A. C. Bone, Z. M. Chan, N. R. Tumelty, A. Steward, L. G. Kwa, A. Borgia, and J. Clarke, *Experimental evidence for a frustrated energy landscape in a three-helix-bundle protein family,* Nature **463**, 685 (2010).

[30] C. J. Jameson, *Understanding NMR Chemical Shifts,* Annu. Rev. Phys. Chem. **47**, 135 (1996).

[31] D. Marion, *An introduction to biological NMR spectroscopy,* Mol. Cell Proteomics **12**, 3006 (2013).

[32] E. J. Ambrose and A. Elliott, *Infra-red spectra and structure of fibrous proteins,* Proc. R. Soc. Lond. A **206**, 206 (1951).

[33] J. M. Chalmers and P. R. Griffiths, eds., *Handbook of Vibrational Spectroscopy*, 1st ed. (Wiley, New York, 2002).

[34] N. Jalili and K. Laxminarayana, *A review of atomic force microscopy imaging systems: application to molecular metrology and biological sciences,* Mechatronics **14**, 907 (2004).

[35] T. Ha, T. Enderle, D. F. Ogletree, D. S. Chemla, P. R. Selvin, and S. Weiss, *Probing the interaction between two single molecules: fluorescence resonance energy transfer between a single donor and a single acceptor,* Proc. Natl. Acad. Sci. U. S. A. **93**, 6264 (1996).

[36] T. Ha, *Single-Molecule Fluorescence Resonance Energy Transfer,* Methods **25**, 78 (2001).

[37] M. S. Smyth and J. H. J. Martin, *x Ray crystallography,* Mol. Pathol. **53**, 8 (2000).

[38] J. T. Edward, *Molecular volumes and the Stokes-Einstein equation,* J. Chem. Educ. **47**, 261 (1970).

[39] G. G. Stokes, *On the effect of the internal friction of fluids on the motion of pendulums.* (Pitt. Press, Cambridge, 1851).

[40] A. Einstein, *Über die von der molekularkinetischen Theorie der Wärme geforderte Bewegung von in ruhenden Flüssigkeiten suspendierten Teilchen,* Ann. Phys. **322**, 549 (1905).

[41] H. Nyquist, *Thermal Agitation of Electric Charge in Conductors,* Phys. Rev. **32**, 110 (1928).

[42] H. B. Callen and T. A. Welton, *Irreversibility and Generalized Noise,* Phys. Rev. **83**, 34 (1951).

[43] M. S. Green, *Markoff Random Processes and the Statistical Mechanics of Time-Dependent Phenomena. II. Irreversible Processes in Fluids,* J. Chem. Phys. **22**, 398 (1954).

[44] R. Kubo, *Statistical-Mechanical Theory of Irreversible Processes. I. General Theory and Simple Applications to Magnetic and Conduction Problems,* J. Phys. Soc. Jpn. **12**, 570 (1957).

[45] J. D. Bryngelson and P. G. Wolynes, *Intermediates and barrier crossing in a random energy model (with applications to protein folding),* J. Phys. Chem. **93**, 6902 (1989).

[46] J. D. Bryngelson, J. N. Onuchic, N. D. Socci, and P. G. Wolynes, *Funnels, pathways, and the energy landscape of protein folding: A synthesis,* Proteins **21**, 167 (1995).

[47] N. D. Socci, J. N. Onuchic, and P. G. Wolynes, *Diffusive dynamics of the reaction coordinate for protein folding funnels,* J. Chem. Phys. **104**, 5860 (1996).

[48] K. A. Dill and H. S. Chan, *From Levinthal to pathways to funnels,* Nat. Struct. Biol. **4**, 10 (1997).

[49] P. G. Bolhuis, D. Chandler, C. Dellago, and P. L. Geissler, *Transition Path Sampling: Throwing Ropes Over Rough Mountain Passes, in the Dark,* Annu. Rev. Phys. Chem. **53**, 291 (2002).

[50] A. Berezhkovskii and A. Szabo, *One-dimensional reaction coordinates for diffusive activated rate processes in many dimensions,* J. Chem. Phys. **122**, 014503 (2004).

[51] O. K. Dudko, G. Hummer, and A. Szabo, *Intrinsic Rates and Activation Free Energies from Single-Molecule Pulling Experiments,* Phys. Rev. Lett. **96**, 108101 (2006).

[52] H. S. Chung, S. Piana-Agostinetti, D. E. Shaw, and W. A. Eaton, *Structural origin of slow diffusion in protein folding,* Science **349**, 1504 (2015).

[53] K. Neupane, A. P. Manuel, and M. T. Woodside, *Protein folding trajectories can be described quantitatively by one-dimensional diffusion over measured energy landscapes,* Nat. Phys. **12**, 700703 (2016).

[54] P. Langevin, *Sur la théorie du mouvement brownien,* C. R. Acad. Sci. **146**, 530 (1908).

[55] H. Risken, *The Fokker-Planck Equation* (Springer, Berlin, New York, 1984).

[56] R. Zwanzig, *Nonequilibrium Statistical Mechanics*, new. ed. (Oxford Univ. Pr., Oxford, New York, 2001).

[57] A. D. Fokker, *Die mittlere Energie rotierender elektrischer Dipole im Strahlungsfeld,* Ann. Phys. **348**, 810 (1914).

[58] M. Planck, in *Sitzber. K. Preuss. Aka.* (1917) pp. 323–341.

[59] W. T. Coffey, *The Langevin Equation: With Applications to Stochastic Problems in Physics, Chemistry and Electrical Engineering (World Scientific Series in Contemporary Chemical Physics Vol. 14) - Second Edition*, 2nd ed. (World Scientific Publishing Company, River Edge, 2004).

[60] H. Mori, *Transport, Collective Motion, and Brownian Motion,* Prog. Theor. Phys. **33**, 423 (1965).

[61] H. K. Shin, C. Kim, P. Talkner, and E. K. Lee, *Brownian motion from molecular dynamics,* Chem. Phys. **375**, 316 (2010).

[62] S. A. Adelman and J. D. Doll, *Generalized Langevin equation approach for atom/solid-surface scattering: General formulation for classical scattering off harmonic solids,* J. Chem. Phys. **64**, 2375 (1976).

[63] P. Debnath, W. Min, X. S. Xie, and B. J. Cherayil, *Multiple time scale dynamics of distance fluctuations in a semiflexible polymer: A one-dimensional generalized Langevin equation treatment,* J. Chem. Phys. **123**, 204903 (2005).

[64] A. Dhar, *Heat transport in low-dimensional systems,* Adv. Phys. **57**, 457 (2008).

[65] J. Fricks, L. Yao, T. Elston, and M. Forest, *Time-Domain Methods for Diffusive Transport in Soft Matter,* SIAM J. Appl. Math. **69**, 1277 (2009).

[66] D. Panja, *Generalized Langevin equation formulation for anomalous polymer dynamics,* J. Stat. Mech. **2010**, L02001 (2010).

[67] T. Franosch, M. Grimm, M. Belushkin, F. M. Mor, G. Foffi, L. Forró, and S. Jeney, *Resonances arising from hydrodynamic memory in Brownian motion,* Nature **478**, 85 (2011).

[68] T. Saito and T. Sakaue, *Driven anomalous diffusion: An example from polymer stretching,* Phys. Rev. E **92**, 012601 (2015).

[69] M. Ernst, T. John, M. Guenther, C. Wagner, U. F. Schaefer, and C.-M. Lehr, *A Model for the Transient Subdiffusive Behavior of Particles in Mucus,* Biophys. J. **112**, 172 (2017).

[70] A. Carof, V. Marry, M. Salanne, J.-P. Hansen, P. Turq, and B. Rotenberg, *Coarse graining the dynamics of nano-confined solutes: the case of ions in clays,* Mol. Simul. **40**, 237 (2014).

[71] D. Lesnicki, R. Vuilleumier, A. Carof, and B. Rotenberg, *Molecular Hydrodynamics from Memory Kernels,* Phys. Rev. Lett. **116**, 147804 (2016).

[72] F. Gottwald, S. Karsten, S. D. Ivanov, and O. Kühn, *Parametrizing linear generalized Langevin dynamics from explicit molecular dynamics simulations,* J. Chem. Phys. **142**, 244110 (2015).

[73] B. J. Berne and G. D. Harp, in *Advances in Chemical Physics*, Vol. 17, edited by I. Prigogine and S. A. Rice (John Wiley & Sons, Inc., 1970) pp. 63–227.

[74] B. J. Berne, M. E. Tuckerman, J. E. Straub, and A. L. R. Bug, *Dynamic friction on rigid and flexible bonds,* J. Chem. Phys. **93**, 5084 (1990).

[75] G. R. Kneller and K. Hinsen, *Computing memory functions from molecular dynamics simulations,* J. Chem. Phys. **115**, 11097 (2001).

[76] L. Bocquet, J.-P. Hansen, and J. Piasecki, *Friction tensor for a pair of Brownian particles: Spurious finite-size effects and molecular dynamics estimates,* J. Stat. Phys. **89**, 321 (1997).

[77] E. Fermi, J. R. Pasta, and S. M. Ulam, *Studies of nonlinear problems*, Tech. Rep. LA-1940 (Los Alamos Nat. Lab., Los Alamos, 1955).

[78] B. J. Alder and T. E. Wainwright, *Studies in Molecular Dynamics. I. General Method,* J. Chem. Phys. **31**, 459 (1959).

[79] M. Tuckerman, K. Laasonen, M. Sprik, and M. Parrinello, *Ab initio molecular dynamics simulation of the solvation and transport of hydronium and hydroxyl ions in water,* J. Chem. Phys. **103**, 150 (1995).

[80] K. Lindorff-Larsen, S. Piana, R. O. Dror, and D. E. Shaw, *How Fast-Folding Proteins Fold,* Science **334**, 517 (2011).

[81] D. E. Shaw, M. M. Deneroff, R. O. Dror, J. S. Kuskin, R. H. Larson, J. K. Salmon, C. Young, B. Batson, K. J. Bowers, J. C. Chao, M. P. Eastwood, J. Gagliardo, J. P. Grossman, C. R. Ho, D. J. Ierardi, I. Kolossváry, J. L. Klepeis, T. Layman, C. McLeavey, M. A. Moraes, R. Mueller, E. C. Priest, Y. Shan, J. Spengler, M. Theobald, B. Towles, and S. C. Wang, *Anton, a Special-purpose Machine for Molecular Dynamics Simulation,* Commun. ACM **51**, 91 (2008).

[82] D. E. Shaw, R. O. Dror, J. K. Salmon, J. P. Grossman, K. M. Mackenzie, J. A. Bank, C. Young, M. M. Deneroff, B. Batson, K. J. Bowers, E. Chow, M. P. Eastwood, D. J. Ierardi, J. L. Klepeis, J. S. Kuskin, R. H. Larson, K. Lindorff-Larsen,

P. Maragakis, M. A. Moraes, S. Piana, Y. Shan, and B. Towles, in *Proceedings of the Conference on High Performance Computing Networking, Storage and Analysis*, SC09 (ACM, New York, 2009) pp. 39:1–39:11.

[83] D. E. Shaw, J. P. Grossman, J. A. Bank, B. Batson, J. A. Butts, J. C. Chao, M. M. Deneroff, R. O. Dror, A. Even, C. H. Fenton, A. Forte, J. Gagliardo, G. Gill, B. Greskamp, C. R. Ho, D. J. Ierardi, L. Iserovich, J. S. Kuskin, R. H. Larson, T. Layman, L. S. Lee, A. K. Lerer, C. Li, D. Killebrew, K. M. Mackenzie, S. Y. H. Mok, M. A. Moraes, R. Mueller, L. J. Nociolo, J. L. Peticolas, T. Quan, D. Ramot, J. K. Salmon, D. P. Scarpazza, U. B. Schafer, N. Siddique, C. W. Snyder, J. Spengler, P. T. P. Tang, M. Theobald, H. Toma, B. Towles, B. Vitale, S. C. Wang, and C. Young, in *SC14: International Conference for High Performance Computing, Networking, Storage and Analysis* (2014) pp. 41–53.

[84] D. Frenkel and B. Smit, *Understanding Molecular Simulation*, 2nd ed. (Academic Press, Inc., Orlando, 2001).

[85] D. L. Ensign, P. M. Kasson, and V. S. Pande, *Heterogeneity Even at the Speed Limit of Folding: Large-scale Molecular Dynamics Study of a Fast-folding Variant of the Villin Headpiece,* ChemPhysChem **374**, 806 (2007).

[86] P. L. Freddolino and K. Schulten, *Common Structural Transitions in Explicit-Solvent Simulations of Villin Headpiece Folding,* Biophys. J. **97**, 2338 (2009).

[87] H. Lei, C. Wu, H. Liu, and Y. Duan, *Folding free-energy landscape of villin headpiece subdomain from molecular dynamics simulations,* Proc. Natl. Acad. Sci. U. S. A. **104**, 4925 (2007).

[88] D. E. Shaw, P. Maragakis, K. Lindorff-Larsen, S. Piana, R. O. Dror, M. P. Eastwood, J. A. Bank, J. M. Jumper, J. K. Salmon, Y. Shan, and W. Wriggers, *Atomic-Level Characterization of the Structural Dynamics of Proteins,* Science **330**, 341 (2010).

[89] V. A. Voelz, G. R. Bowman, K. Beauchamp, and V. S. Pande, *Molecular Simulation of ab Initio Protein Folding for a Millisecond Folder NTL9(1-39),* J. Am. Chem. Soc. **132**, 1526 (2010).

[90] R. O. Dror, R. M. Dirks, J. P. Grossman, H. Xu, and D. E. Shaw, *Biomolecular Simulation: A Computational Microscope for Molecular Biology,* Annu. Rev. Biophys. **41**, 429 (2012).

[91] R. O. Dror, A. C. Pan, D. H. Arlow, D. W. Borhani, P. Maragakis, Y. Shan, H. Xu, and D. E. Shaw, *Pathway and mechanism of drug binding to G-protein-coupled receptors,* Proc. Natl. Acad. Sci. U. S. A. **108**, 13118 (2011).

[92] D. P. Hurst, A. Grossfield, D. L. Lynch, S. Feller, T. D. Romo, K. Gawrisch, M. C. Pitman, and P. H. Reggio, *A Lipid Pathway for Ligand Binding Is Necessary for a Cannabinoid G Protein-coupled Receptor,* J. Biol. Chem. **285**, 17954 (2010).

[93] Y. Shan, E. T. Kim, M. P. Eastwood, R. O. Dror, M. A. Seeliger, and D. E. Shaw, *How Does a Drug Molecule Find Its Target Binding Site?* J. Am. Chem. Soc. **133**, 9181 (2011).

[94] B. Roux, S. Y. Noskov, and S. Bernèche, *Control of ion selectivity in potassium channels by electrostatic and dynamic properties of carbonyl ligands,* Nature **431**, 830 (2004).

[95] M. Ø. Jensen, R. O. Dror, H. Xu, D. W. Borhani, I. T. Arkin, M. P. Eastwood, and D. E. Shaw, *Dynamic control of slow water transport by aquaporin 0: Implications for hydration and junction stability in the eye lens,* Proc. Natl. Acad. Sci. U. S. A. **105**, 14430 (2008).

[96] D. L. Bostick and C. L. Brooks, *Selectivity in K+ channels is due to topological control of the permeant ion's coordinated state,* Proc. Natl. Acad. Sci. U. S. A. **104**, 9260 (2007).

[97] M. Ø. Jensen, D. W. Borhani, K. Lindorff-Larsen, P. Maragakis, V. Jogini, M. P. Eastwood, R. O. Dror, and D. E. Shaw, *Principles of conduction and hydrophobic gating in K+ channels,* Proc. Natl. Acad. Sci. U. S. A. **107**, 5833 (2010).

[98] P. L. Freddolino, A. S. Arkhipov, S. B. Larson, A. McPherson, and K. Schulten, *Molecular Dynamics Simulations of the Complete Satellite Tobacco Mosaic Virus,* Structure **14**, 437 (2006).

[99] W. Kohn and L. J. Sham, *Self-Consistent Equations Including Exchange and Correlation Effects,* Phys. Rev. **140**, A1133 (1965).

[100] D. Marx and J. Hutter, in *Modern Methods and Algorithms of Quantum Chemistry, John Von Neumann Institute for Computing, Forschungszentrum Jülich, 2000* (2000) pp. 329–477.

[101] J. Hutter, M. Iannuzzi, F. Schiffmann, and J. VandeVondele, *cp2k: atomistic simulations of condensed matter systems,* Wiley Interdiscip. Rev.: Comput. Mol. Sci. **4**, 15 (2014).

[102] C. Michel, A. Laio, F. Mohamed, M. Krack, M. Parrinello, and A. Milet, *Free Energy ab Initio Metadynamics: A New Tool for the Theoretical Study of Organometallic Reactivity? Example of the C-C and C-H Reductive Eliminations from Platinum(IV) Complexes,* Organometallics **26**, 1241 (2007).

[103] F. Masson, T. Laino, I. Tavernelli, U. Rothlisberger, and J. Hutter, *Computational Study of Thymine Dimer Radical Anion Splitting in the Self-Repair Process of Duplex DNA,* J. Am. Chem. Soc. **130**, 3443 (2008).

[104] F. Masson, T. Laino, U. Rothlisberger, and J. Hutter, *A QM/MM Investigation of Thymine Dimer Radical Anion Splitting Catalyzed by DNA Photolyase,* ChemPhysChem **10**, 400 (2009).

[105] S. S. Xantheas and T. H. Dunning, *Ab initio studies of cyclic water clusters $(H_2O)_n$, n=1–6. I. Optimal structures and vibrational spectra,* J. Chem. Phys. **99**, 8774 (1993).

[106] P. J. Stephens, F. J. Devlin, C. F. Chabalowski, and M. J. Frisch, *Ab Initio Calculation of Vibrational Absorption and Circular Dichroism Spectra Using Density Functional Force Fields,* J. Phys. Chem. **98**, 11623 (1994).

[107] P. L. Silvestrelli, M. Bernasconi, and M. Parrinello, *Ab initio infrared spectrum of liquid water,* Chem. Phys. Lett. **277**, 478 (1997).

[108] R. Rousseau, V. Kleinschmidt, U. W. Schmitt, and D. Marx, *Modeling protonated water networks in bacteriorhodopsin,* Phys. Chem. Chem. Phys. **6**, 1848 (2004).

[109] G. Mathias and D. Marx, *Structures and spectral signatures of protonated water networks in bacteriorhodopsin,* Proc. Natl. Acad. Sci. U. S. A. **104**, 6980 (2007).

[110] K. Gerwert, E. Freier, and S. Wolf, *The role of protein-bound water molecules in microbial rhodopsins,* Biochim. Biophys. Acta, Bioenerg. **1837**, 606 (2014).

[111] J. Heberle, *Proton transfer reactions across bacteriorhodopsin and along the membrane,* Biochim. Biophys. Acta, Bioenerg. **1458**, 135 (2000).

[112] N. A. Dencher, H. J. Sass, and G. Büldt, *Water and bacteriorhodopsin: structure, dynamics, and function,* Biochim. Biophys. Acta, Bioenerg. **1460**, 192 (2000).

[113] F. Garczarek and K. Gerwert, *Functional waters in intraprotein proton transfer monitored by FTIR difference spectroscopy,* Nature **439**, 109 (2006).

[114] A.-N. Bondar, J. Baudry, S. Suhai, S. Fischer, and J. C. Smith, *Key Role of Active-Site Water Molecules in Bacteriorhodopsin Proton-Transfer Reactions,* J. Phys. Chem. B **112**, 14729 (2008).

[115] Y. Furutani and H. Kandori, *Hydrogen-bonding changes of internal water molecules upon the actions of microbial rhodopsins studied by FTIR spectroscopy,* Biochim. Biophys. Acta, Bioenerg. **1837**, 598 (2014).

[116] W. Kuhn and H. Kuhn, *Modellmässige Deutung der inneren Viskosität (der Formzähigkeitskonstante) von Fadenmolekeln I,* Helv. Chim. Acta **29**, 609 (1946).

[117] J. J. Portman, S. Takada, and P. G. Wolynes, *Microscopic theory of protein folding rates. II. Local reaction coordinates and chain dynamics,* J. Chem. Phys. **114**, 5082 (2001).

[118] B. S. Khatri and T. C. B. McLeish, *Rouse Model with Internal Friction: A Coarse Grained Framework for Single Biopolymer Dynamics,* Macromolecules **40**, 6770 (2007).

[119] I. Echeverria, D. E. Makarov, and G. A. Papoian, *Concerted Dihedral Rotations Give Rise to Internal Friction in Unfolded Proteins,* J. Am. Chem. Soc. **136**, 8708 (2014).

[120] D. de Sancho, A. Sirur, and R. B. Best, *Molecular origins of internal friction effects on protein-folding rates,* Nat. Commun. **5**, 5307 (2014).

[121] W. Zheng, D. de Sancho, T. Hoppe, and R. B. Best, *Dependence of Internal Friction on Folding Mechanism,* J. Am. Chem. Soc. **137**, 3283 (2015).

[122] W. Zheng, D. de Sancho, and R. B. Best, *Modulation of Folding Internal Friction by Local and Global Barrier Heights,* J. Phys. Chem. Lett. **7**, 1028 (2016).

[123] A. Soranno, A. Holla, F. Dingfelder, D. Nettels, D. E. Makarov, and B. Schuler, *Integrated view of internal friction in unfolded proteins from single-molecule FRET, contact quenching, theory, and simulations,* Proc. Natl. Acad. Sci. U. S. A. **114**, E1833 (2017).

[124] S. M. Avdoshenko, A. Das, R. Satija, G. A. Papoian, and D. E. Makarov, *Theoretical and computational validation of the Kuhn barrier friction mechanism in unfolded proteins,* Sci. Rep. **7** (2017).

[125] S. Iwata, C. Ostermeier, B. Ludwig, and H. Michel, *Structure at 2.8 Å resolution of cytochrome c oxidase from Paracoccus denitrificans,* Nature **376**, 660 (1995).

[126] Y. Umena, K. Kawakami, J.-R. Shen, and N. Kamiya, *Crystal structure of oxygen-evolving photosystem II at a resolution of 1.9 Å,* Nature **473**, 55 (2011).

[127] H. E. Kato, F. Zhang, O. Yizhar, C. Ramakrishnan, T. Nishizawa, K. Hirata, J. Ito, Y. Aita, T. Tsukazaki, S. Hayashi, P. Hegemann, A. D. Maturana, R. Ishitani, K. Deisseroth, and O. Nureki, *Crystal structure of the channelrhodopsin light-gated cation channel,* Nature **482**, 369 (2012).

[128] G. Zundel, in *Advances in Chemical Physics*, edited by I. Prigogine and S. A. Rice (John Wiley & Sons, Inc., Chicago, 1999) pp. 1–217.

[129] R. Vuilleumier and D. Borgis, *Transport and spectroscopy of the hydrated proton: A molecular dynamics study,* J. Chem. Phys. **111**, 4251 (1999).

[130] R. Iftimie and M. E. Tuckerman, *The Molecular Origin of the "Continuous" Infrared Absorption in Aqueous Solutions of Acids: A Computational Approach,* Angew. Chem., Int. Ed. **45**, 1144 (2006).

[131] J. Lobaugh and G. A. Voth, *The quantum dynamics of an excess proton in water,* J. Chem. Phys. **104**, 2056 (1996).

[132] T. Ackermann, *Das Absorptionsspektrum wäßriger Säure- und Alkalihydroxydlösungen im Wellenlängenbereich von 2,5 bis 9 μ*,* Z. Phys. Chem. (N. F.) **27**, 253 (1961).

[133] J. le Coutre, J. Tittor, D. Oesterhelt, and K. Gerwert, *Experimental evidence for hydrogen-bonded network proton transfer in bacteriorhodopsin shown by Fourier-transform infrared spectroscopy using azide as catalyst,* Proc. Natl. Acad. Sci. U. S. A. **92**, 4962 (1995).

[134] F. Garczarek, J. Wang, M. A. El-Sayed, and K. Gerwert, *The Assignment of the Different Infrared Continuum Absorbance Changes Observed in the 3000–1800 cm^{-1} Region during the Bacteriorhodopsin Photocycle,* Biophys. J. **87**, 2676 (2004).

[135] E. Freier, S. Wolf, and K. Gerwert, *Proton transfer via a transient linear water-molecule chain in a membrane protein,* Proc. Natl. Acad. Sci. U. S. A. **108**, 11435 (2011).

[136] S. Wolf, E. Freier, Q. Cui, and K. Gerwert, *Infrared spectral marker bands characterizing a transient water wire inside a hydrophobic membrane protein,* J. Chem. Phys. **141**, 22D524 (2014).

[137] P. Goyal, N. Ghosh, P. Phatak, M. Clemens, M. Gaus, M. Elstner, and Q. Cui, *Proton Storage Site in Bacteriorhodopsin: New Insights from Quantum Mechanics/Molecular Mechanics Simulations of Microscopic pKa and Infrared Spectra,* J. Am. Chem. Soc. **133**, 14981 (2011).

[138] M. Heyden, J. Sun, S. Funkner, G. Mathias, H. Forbert, M. Havenith, and D. Marx, *Dissecting the THz spectrum of liquid water from first principles via correlations in time and space,* Proc. Natl. Acad. Sci. U. S. A. **107**, 12068 (2010).

[139] J. E. Bertie and Z. Lan, *Infrared Intensities of Liquids XX: The Intensity of the OH Stretching Band of Liquid Water Revisited, and the Best Current Values of the Optical Constants of H_2O(l) at 25°C between 15,000 and 1 cm^{-1},* Appl. Spectrosc. **50**, 1047 (1996).

[140] Z. Cao, Y. Peng, T. Yan, S. Li, A. Li, and G. A. Voth, *Mechanism of Fast Proton Transport along One-Dimensional Water Chains Confined in Carbon Nanotubes,* J. Am. Chem. Soc. **132**, 11395 (2010).

[141] V. R. I. Kaila and G. Hummer, *Energetics and dynamics of proton transfer reactions along short water wires,* Phys. Chem. Chem. Phys. **13**, 13207 (2011).

[142] J. E. Bertie, M. K. Ahmed, and H. H. Eysel, *Infrared intensities of liquids. 5. Optical and dielectric constants, integrated intensities, and dipole moment derivatives of H_2O and D_2O at 22°C,* J. Phys. Chem. **93**, 2210 (1989).

[143] R. Ramírez, T. López-Ciudad, P. Kumar P, and D. Marx, *Quantum corrections to classical time-correlation functions: Hydrogen bonding and anharmonic floppy modes,* J. Chem. Phys. **121**, 3973 (2004).

[144] Q. Du, E. Freysz, and Y. R. Shen, *Surface Vibrational Spectroscopic Studies of Hydrogen Bonding and Hydrophobicity,* Science **264**, 826 (1994).

[145] L. F. Scatena, M. G. Brown, and G. L. Richmond, *Water at Hydrophobic Surfaces: Weak Hydrogen Bonding and Strong Orientation Effects,* Science **292**, 908 (2001).

[146] P. Nogly, V. Panneels, G. Nelson, C. Gati, T. Kimura, C. Milne, D. Milathianaki, M. Kubo, W. Wu, C. Conrad, J. Coe, R. Bean, Y. Zhao, P. Båth, R. Dods, R. Harimoorthy, K. R. Beyerlein, J. Rheinberger, D. James, D. DePonte, C. Li, L. Sala, G. J. Williams, M. S. Hunter, J. E. Koglin, P. Berntsen, E. Nango, S. Iwata, H. N. Chapman, P. Fromme, M. Frank, R. Abela, S. Boutet, A. Barty, T. A. White, U. Weierstall, J. Spence, R. Neutze, G. Schertler, and J. Standfuss, *Lipidic cubic phase injector is a viable crystal delivery system for time-resolved serial crystallography,* Nat. Commun. **7**, 12314 (2016).

[147] R. M. Nyquist, K. Ataka, and J. Heberle, *The Molecular Mechanism of Membrane Proteins Probed by Evanescent Infrared Waves,* ChemBioChem **5**, 431 (2004).

[148] K. J. Rothschild and N. A. Clark, *Polarized infrared spectroscopy of oriented purple membrane,* Biophys. J. **25**, 473 (1979).

[149] G. Papadopoulos, N. A. Dencher, G. Zaccai, and G. Büldt, *Water molecules and exchangeable hydrogen ions at the active centre of bacteriorhodopsin localized by neutron diffraction,* J. Mol. Biol. **214**, 15 (1990).

[150] G. Thiedemann, J. Heberle, and N. A. Dencher, in *Structures and Functions of Retinal Proteins*, Vol. 221 (Colloque INSERM/John Libbey Eurotext Ltd., Montrogue, 1992) pp. 217–220.

[151] R. H. Lozier, R. A. Bogomolni, and W. Stoeckenius, *Bacteriorhodopsin: a light-driven proton pump in Halobacterium Halobium,* Biophys. J. **15**, 955 (1975).

[152] R. Korenstein and B. Hess, *Hydration effects on the photocycle of bacteriorhodopsin in thin layers of purple membrane,* Nature **270**, 184 (1977).

[153] V. A. Lórenz-Fonfría, Y. Furutani, and H. Kandori, *Active Internal Waters in the Bacteriorhodopsin Photocycle. A Comparative Study of the L and M Intermediates at Room and Cryogenic Temperatures by Infrared Spectroscopy,* Biochemistry **47**, 4071 (2008).

[154] D. Marsh, *Quantitation of Secondary Structure in ATR Infrared Spectroscopy,* Biophys. J. **77**, 2630 (1999).

[155] E. Goormaghtigh, V. Raussens, and J.-M. Ruysschaert, *Attenuated total reflection infrared spectroscopy of proteins and lipids in biological membranes,* Biochim. Biophys. Acta, Bioenerg. **1422**, 105 (1999).

[156] V. A. Lórenz-Fonfría, M. Granell, X. León, G. Leblanc, and E. Padrós, *In-Plane and Out-of-Plane Infrared Difference Spectroscopy Unravels Tilting of Helices and Structural Changes in a Membrane Protein upon Substrate Binding,* J. Am. Chem. Soc. **131**, 15094 (2009).

[157] M. S. Braiman, T. Mogi, T. Marti, L. J. Stern, H. G. Khorana, and K. J. Rothschild, *Vibrational spectroscopy of bacteriorhodopsin mutants: light-driven proton transport involves protonation changes of aspartic acid residues 85, 96, and 212,* Biochemistry **27**, 8516 (1988).

[158] J. Heberle, J. Riesle, G. Thiedemann, D. Oesterhelt, and N. A. Dencher, *Proton migration along the membrane surface and retarded surface to bulk transfer,* Nature **370**, 379 (1994).

[159] F. Garczarek, L. S. Brown, J. K. Lanyi, and K. Gerwert, *Proton binding within a membrane protein by a protonated water cluster,* Proc. Natl. Acad. Sci. U. S. A. **102**, 3633 (2005).

[160] J. Heberle and N. A. Dencher, *Surface-bound optical probes monitor protein translocation and surface potential changes during the bacteriorhodopsin photocycle,* Proc. Natl. Acad. Sci. U. S. A. **89**, 5996 (1992).

[161] M. G. Wolf, H. Grubmüller, and G. Groenhof, *Anomalous Surface Diffusion of Protons on Lipid Membranes,* Biophys. J. **107**, 76 (2014).

[162] W. Kulig and N. Agmon, *A 'clusters-in-liquid' method for calculating infrared spectra identifies the proton-transfer mode in acidic aqueous solutions,* Nat. Chem. **5**, 29 (2013).

[163] J. Riesle, D. Oesterhelt, N. A. Dencher, and J. Heberle, *D38 Is an Essential Part of the Proton Translocation Pathway in Bacteriorhodopsin,* Biochemistry **35**, 6635 (1996).

[164] L. Kelemen and P. Ormos, *Structural Changes in Bacteriorhodopsin during the Photocycle Measured by Time-Resolved Polarized Fourier Transform Infrared Spectroscopy,* Biophys. J. **81**, 3577 (2001).

[165] B. C. Polander and B. A. Barry, *Detection of an intermediary, protonated water cluster in photosynthetic oxygen evolution,* Proc. Natl. Acad. Sci. U. S. A. **110**, 10634 (2013).

[166] S. Hermes, J. M. Stachnik, D. Onidas, A. Remy, E. Hofmann, and K. Gerwert, *Proton Uptake in the Reaction Center Mutant L210DN from Rhodobacter sphaeroides via Protonated Water Molecules,* Biochemistry **45**, 13741 (2006).

[167] J. Breton and E. Nabedryk, *Proton uptake upon quinone reduction in bacterial reaction centers: IR signature and possible participation of a highly polarizable hydrogen bond network,* Photosynth. Res. **55**, 301 (1998).

[168] E. C. S. Clair, J. I. Ogren, S. Mamaev, J. M. Kralj, and K. J. Rothschild, *Conformational changes in the archaerhodopsin-3 proton pump: detection of conserved strongly hydrogen bonded water networks,* J. Biol. Phys. **38**, 153 (2012).

[169] J. Xu, M. A. Sharpe, L. Qin, S. Ferguson-Miller, and G. A. Voth, *Storage of an Excess Proton in the Hydrogen-Bonded Network of the D-Pathway of Cytochrome c Oxidase: Identification of a Protonated Water Cluster,* J. Am. Chem. Soc. **129**, 2910 (2007).

[170] K. Gawrisch, V. A. Parsegian, D. A. Hajduk, M. W. Tate, S. M. Gruner, N. L. Fuller, and R. P. Rand, *Energetics of a hexagonal-lamellar-hexagonal-phase transition sequence in dioleoylphosphatidylethanolamine membranes,* Biochemistry **31**, 2856 (1992).

[171] U. Mennicke and T. Salditt, *Preparation of Solid-Supported Lipid Bilayers by Spin-Coating,* Langmuir **18**, 8172 (2002).

[172] R. H. Tunuguntla, F. I. Allen, K. Kim, A. Belliveau, and A. Noy, *Ultrafast proton transport in sub-1-nm diameter carbon nanotube porins,* Nat. Nanotechnol. **11**, 639 (2016).

[173] The CP2K Developers Group, http://www.cp2k.org/ (2014), accessed: July 2017.

[174] J. VandeVondele and J. Hutter, *Gaussian basis sets for accurate calculations on molecular systems in gas and condensed phases,* J. Chem. Phys. **127**, 114105 (2007).

[175] A. D. Becke, *Density-functional exchange-energy approximation with correct asymptotic behavior,* Phys. Rev. A **38**, 3098 (1988).

[176] G. J. Martyna and M. E. Tuckerman, *A reciprocal space based method for treating long range interactions in ab initio and force-field-based calculations in clusters,* J. Chem. Phys. **110**, 2810 (1999).

[177] S. Nosé, *A unified formulation of the constant temperature molecular dynamics methods,* J. Chem. Phys. **81**, 511 (1984).

[178] W. G. Hoover, *Canonical dynamics: Equilibrium phase-space distributions,* Phys. Rev. A **31**, 1695 (1985).

[179] C. Dellago, M. M. Naor, and G. Hummer, *Proton Transport through Water-Filled Carbon Nanotubes,* Phys. Rev. Lett. **90**, 105902 (2003).

[180] B. Halle and M. Davidovic, *Biomolecular hydration: From water dynamics to hydrodynamics,* Proc. Natl. Acad. Sci. U. S. A. **100**, 12135 (2003).

[181] L. R. Winther, J. Qvist, and B. Halle, *Hydration and Mobility of Trehalose in Aqueous Solution,* J. Phys. Chem. B **116**, 9196 (2012).

[182] S.-J. Marrink and H. J. C. Berendsen, *Simulation of water transport through a lipid membrane,* J. Phys. Chem. **98**, 4155 (1994).

[183] M. Hinczewski, Y. von Hansen, J. Dzubiella, and R. R. Netz, *How the diffusivity profile reduces the arbitrariness of protein folding free energies,* J. Chem. Phys. **132**, 245103 (2010).

[184] R. Schulz, K. Yamamoto, A. Klossek, R. Flesch, S. Hönzke, F. Rancan, A. Vogt, U. Blume-Peytavi, S. Hedtrich, M. Schäfer-Korting, E. Rühl, and R. R. Netz, *Data-based modeling of drug penetration relates human skin barrier function to the interplay of diffusivity and free-energy profiles,* Proc. Natl. Acad. Sci. U. S. A. **114**, 3631 (2017).

[185] P. M. Hansen, V. K. Bhatia, N. Harrit, and L. Oddershede, *Expanding the Optical Trapping Range of Gold Nanoparticles,* Nano Lett. **5**, 1937 (2005).

[186] A. P. Fields and A. E. Cohen, *Electrokinetic trapping at the one nanometer limit,* Proc. Natl. Acad. Sci. U. S. A. **108**, 8937 (2011).

[187] P. Español and I. Zúñiga, *Force autocorrelation function in Brownian motion theory,* J. Chem. Phys. **98**, 574 (1993).

[188] L. Bocquet, J. Piasecki, and J.-P. Hansen, *On the Brownian motion of a massive sphere suspended in a hard-sphere fluid. I. Multiple-time-scale analysis and microscopic expression for the friction coefficient,* J. Stat. Phys. **76**, 505 (1994).

[189] B. Hess, C. Kutzner, D. van der Spoel, and E. Lindahl, *GROMACS 4: Algorithms for Highly Efficient, Load-Balanced, and Scalable Molecular Simulation,* J. Chem. Theory Comput. **4**, 435 (2008).

[190] M. J. Abraham, T. Murtola, R. Schulz, S. Páll, J. C. Smith, B. Hess, and E. Lindahl, *GROMACS: High performance molecular simulations through multi-level parallelism from laptops to supercomputers,* SoftwareX **1–2**, 19 (2015).

[191] C. Oostenbrink, A. Villa, A. E. Mark, and W. F. Van Gunsteren, *A biomolecular force field based on the free enthalpy of hydration and solvation: The GROMOS force-field parameter sets 53A5 and 53A6,* J. Comput. Chem. **25**, 1656 (2004).

[192] H. J. C. Berendsen, J. R. Grigera, and T. P. Straatsma, *The missing term in effective pair potentials,* J. Phys. Chem. **91**, 6269 (1987).

[193] G. Bussi, D. Donadio, and M. Parrinello, *Canonical sampling through velocity rescaling,* J. Chem. Phys. **126**, 014101 (2007).

[194] H. J. C. Berendsen, J. P. M. Postma, W. F. van Gunsteren, A. DiNola, and J. R. Haak, *Molecular dynamics with coupling to an external bath,* J. Chem. Phys. **81**, 3684 (1984).

[195] A. Luzar and D. Chandler, *Hydrogen-bond kinetics in liquid water,* Nature **379**, 55 (1996).

[196] R. Zwanzig and M. Bixon, *Hydrodynamic Theory of the Velocity Correlation Function,* Phys. Rev. A **2**, 2005 (1970).

[197] P. A. Witherspoon and D. N. Saraf, *Diffusion of Methane, Ethane, Propane, and n-Butane in Water from 25 to 43°,* J. Phys. Chem. **69**, 3752 (1965).

[198] I.-C. Yeh and G. Hummer, *System-Size Dependence of Diffusion Coefficients and Viscosities from Molecular Dynamics Simulations with Periodic Boundary Conditions,* J. Phys. Chem. B **108**, 15873 (2004).

[199] S. Koneshan, R. M. Lynden-Bell, and J. C. Rasaiah, *Friction Coefficients of Ions in Aqueous Solution at 25 °C,* J. Am. Chem. Soc. **120**, 12041 (1998).

[200] M. A. Wilson, A. Pohorille, and L. R. Pratt, *Molecular dynamics test of the Brownian description of Na+ motion in water,* J. Chem. Phys. **83**, 5832 (1985).

[201] M. Berkowitz and W. Wan, *The limiting ionic conductivity of Na+ and Cl- ions in aqueous solutions: Molecular dynamics simulation,* J. Chem. Phys. **86**, 376 (1987).

[202] R. W. Impey, P. A. Madden, and I. R. McDonald, *Hydration and mobility of ions in solution,* J. Phys. Chem. **87**, 5071 (1983).

[203] J. M. Franck, A. Pavlova, J. A. Scott, and S. Han, *Quantitative cw Overhauser effect dynamic nuclear polarization for the analysis of local water dynamics,* Prog. Nucl. Magn. Reson. Spectrosc. **74**, 33 (2013).

[204] J. M. Franck, Y. Ding, K. Stone, P. Z. Qin, and S. Han, *Anomalously Rapid Hydration Water Diffusion Dynamics Near DNA Surfaces,* J. Am. Chem. Soc. **137**, 12013 (2015).

[205] Y. von Hansen, F. Sedlmeier, M. Hinczewski, and R. R. Netz, *Friction contribution to water-bond breakage kinetics,* Phys. Rev. E **84**, 051501 (2011).

[206] F. Sterpone, G. Stirnemann, and D. Laage, *Magnitude and Molecular Origin of Water Slowdown Next to a Protein,* J. Am. Chem. Soc. **134**, 4116 (2012).

[207] P. G. Wolynes, *Molecular theory of solvated ion dynamics,* J. Chem. Phys. **68**, 473 (1978).

[208] F. Sedlmeier, Y. von Hansen, L. Mengyu, D. Horinek, and R. R. Netz, *Water Dynamics at Interfaces and Solutes: Disentangling Free Energy and Diffusivity Contributions,* J. Stat. Phys. **145**, 240 (2011).

[209] B. Jähne, G. Heinz, and W. Dietrich, *Measurement of the diffusion coefficients of sparingly soluble gases in water,* J. Geophys. Res. **92**, 10767 (1987).

[210] G. Otting, E. Liepinsh, and K. Wuthrich, *Protein hydration in aqueous solution,* Science **254**, 974 (1991).

[211] D. Zhong, S. K. Pal, and A. H. Zewail, *Biological water: A critique,* Chem. Phys. Lett. **503**, 1 (2011).

[212] L. Zhang, L. Wang, Y.-T. Kao, W. Qiu, Y. Yang, O. Okobiah, and D. Zhong, *Mapping hydration dynamics around a protein surface,* Proc. Natl. Acad. Sci. U. S. A. **104**, 18461 (2007).

[213] J. T. King and K. J. Kubarych, *Site-specific coupling of hydration water and protein flexibility studied in solution with ultrafast 2D-IR spectroscopy,* J. Am. Chem. Soc. **134**, 18705 (2012).

[214] D. Russo, G. Hura, and T. Head-Gordon, *Hydration Dynamics Near a Model Protein Surface,* Biophys. J. **86**, 1852 (2004).

[215] B. Born, S. Joong Kim, S. Ebbinghaus, M. Gruebele, and M. Havenith, *The terahertz dance of water with the proteins : the effect of protein flexibility on the dynamical hydration shell of ubiquitin,* Faraday Discuss. **141**, 161 (2009).

[216] J. W. Bye, S. Meliga, D. Ferachou, G. Cinque, J. A. Zeitler, and R. J. Falconer, *Analysis of the Hydration Water around Bovine Serum Albumin Using Terahertz Coherent Synchrotron Radiation,* J. Phys. Chem. A **118**, 83 (2014).

[217] P. J. Rossky and M. Karplus, *Solvation. A molecular dynamics study of a dipeptide in water,* J. Am. Chem. Soc. **101**, 1913 (1979).

[218] M. W. Hodges, D. S. Cafiso, C. F. Polnaszek, C. C. Lester, and R. G. Bryant, *Water translational motion at the bilayer interface: an NMR relaxation dispersion measurement,* Biophys. J. **73**, 2575 (1997).

[219] C. Mattea, J. Qvist, and B. Halle, *Dynamics at the Protein-Water Interface from* ^{17}*O Spin Relaxation in Deeply Supercooled Solutions,* Biophys. J. **95**, 2951 (2008).

[220] D. Laage, G. Stirnemann, and J. T. Hynes, *Why Water Reorientation Slows without Iceberg Formation around Hydrophobic Solutes,* J. Phys. Chem. B **113**, 2428 (2009).

[221] F. Sterpone, G. Stirnemann, J. T. Hynes, and D. Laage, *Water Hydrogen-Bond Dynamics around Amino Acids: The Key Role of Hydrophilic Hydrogen-Bond Acceptor Groups,* J. Phys. Chem. B **114**, 2083 (2010).

[222] F. Pizzitutti, M. Marchi, F. Sterpone, and P. J. Rossky, *How Protein Surfaces Induce Anomalous Dynamics of Hydration Water,* J. Phys. Chem. B **111**, 7584 (2007).

[223] R. Kipfer, W. Aeschbach-Hertig, F. Peeters, and M. Stute, *Noble Gases in Lakes and Ground Waters,* Rev. Mineral. Geochem. **47**, 615 (2002).

[224] F. Peeters, U. Beyerle, W. Aeschbach-Hertig, J. Holocher, M. S. Brennwald, and R. Kipfer, *Improving noble gas based paleoclimate reconstruction and groundwater dating using $^{20}Ne/^{22}Ne$ ratios,* Geochim. Cosmochim. Acta **67**, 587 (2003).

[225] M. S. Brennwald, M. Hofer, F. Peeters, W. Aeschbach-Hertig, K. Strassmann, R. Kipfer, and D. M. Imboden, *Analysis of dissolved noble gases in the porewater of lacustrine sediments,* Limnol. Oceanogr.: Methods **1**, 51 (2003).

[226] M. S. Brennwald, R. Kipfer, and D. M. Imboden, *Release of gas bubbles from lake sediment traced by noble gas isotopes in the sediment pore water,* Earth Planet. Sci. Lett. **235**, 31 (2005).

[227] W. Aeschbach-Hertig and D. K. Solomon, in *The Noble Gases as Geochemical Tracers*, Advances in Isotope Geochemistry (Springer, Berlin, Heidelberg, 2013) pp. 81–122.

[228] J. M. Eiler, B. Bergquist, I. Bourg, P. Cartigny, J. Farquhar, A. Gagnon, W. Guo, I. Halevy, A. Hofmann, T. E. Larson, N. Levin, E. A. Schauble, and D. Stolper, *Frontiers of stable isotope geoscience,* Chem. Geol. **372**, 119 (2014).

[229] S. Bhattacharyya and B. Bagchi, *Power law mass dependence of diffusion: A mode coupling theory analysis,* Phys. Rev. E **61**, 3850 (2000).

[230] M. Willeke, *Limits of the validity of the mass ratio independence of the Stokes—Einstein relation: molecular dynamics calculations and comparison with the Enskog theory,* Mol. Phys. **101**, 1123 (2003).

[231] I. C. Bourg and G. Sposito, *Molecular dynamics simulations of kinetic isotope fractionation during the diffusion of ionic species in liquid water,* Geochim. Cosmochim. Acta **71**, 5583 (2007).

[232] I. C. Bourg and G. Sposito, *Isotopic fractionation of noble gases by diffusion in liquid water: Molecular dynamics simulations and hydrologic applications,* Geochim. Cosmochim. Acta **72**, 2237 (2008).

[233] I. C. Bourg, F. M. Richter, J. N. Christensen, and G. Sposito, *Isotopic mass dependence of metal cation diffusion coefficients in liquid water,* Geochim. Cosmochim. Acta **74**, 2249 (2010).

[234] L. Tyroller, M. S. Brennwald, L. Mächler, D. M. Livingstone, and R. Kipfer, *Fractionation of Ne and Ar isotopes by molecular diffusion in water,* Geochim. Cosmochim. Acta **136**, 60 (2014).

[235] A. E. Hofmann, I. C. Bourg, and D. J. DePaolo, *Ion desolvation as a mechanism for kinetic isotope fractionation in aqueous systems,* Proc. Natl. Acad. Sci. U. S. A. **109**, 18689 (2012).

[236] G. D. Harp and B. J. Berne, *Time-Correlation Functions, Memory Functions, and Molecular Dynamics,* Phys. Rev. A **2**, 975 (1970).

[237] F. M. Richter, R. A. Mendybaev, J. N. Christensen, I. D. Hutcheon, R. W. Williams, N. C. Sturchio, and A. D. Beloso, *Kinetic isotopic fractionation during diffusion of ionic species in water,* Geochim. Cosmochim. Acta **70**, 277 (2006).

[238] J. F. Barker and P. Fritz, *Carbon isotope fractionation during microbial methane oxidation,* Nature **293**, 289 (1981).

[239] M. J. Whiticar, *Carbon and hydrogen isotope systematics of bacterial formation and oxidation of methane,* Chem. Geol. **161**, 291 (1999).

[240] D. T. Wang, D. S. Gruen, B. S. Lollar, K.-U. Hinrichs, L. C. Stewart, J. F. Holden, A. N. Hristov, J. W. Pohlman, P. L. Morrill, M. Könneke, K. B. Delwiche, E. P. Reeves, C. N. Sutcliffe, D. J. Ritter, J. S. Seewald, J. C. McIntosh, H. F. Hemond, M. D. Kubo, D. Cardace, T. M. Hoehler, and S. Ono, *Nonequilibrium clumped isotope signals in microbial methane,* Science **348**, 428 (2015).

[241] J. C. F. Schulz, L. Schmidt, R. B. Best, J. Dzubiella, and R. R. Netz, *Peptide Chain Dynamics in Light and Heavy Water: Zooming in on Internal Friction,* J. Am. Chem. Soc. **134**, 6273 (2012).

[242] H. A. Kramers, *Brownian motion in a field of force and the diffusion model of chemical reactions,* Physica **7**, 284 (1940).

[243] O. Bieri, J. Wirz, B. Hellrung, M. Schutkowski, M. Drewello, and T. Kiefhaber, *The speed limit for protein folding measured by triplet–triplet energy transfer,* Proc. Natl. Acad. Sci. U. S. A. **96**, 9597 (1999).

[244] A. Borgia, B. G. Wensley, A. Soranno, D. Nettels, M. B. Borgia, A. Hoffmann, S. H. Pfeil, E. A. Lipman, J. Clarke, and B. Schuler, *Localizing internal friction along the reaction coordinate of protein folding by combining ensemble and single-molecule fluorescence spectroscopy,* Nat. Commun. **3**, 1195 (2012).

[245] D. K. Klimov and D. Thirumalai, *Viscosity Dependence of the Folding Rates of Proteins,* Phys. Rev. Lett. **79**, 317 (1997).

[246] R. B. Best and G. Hummer, *Diffusive Model of Protein Folding Dynamics with Kramers Turnover in Rate,* Phys. Rev. Lett. **96**, 228104 (2006).

[247] D. Chandler, *Statistical mechanics of isomerization dynamics in liquids and the transition state approximation,* J. Chem. Phys. **68**, 2959 (1978).

[248] R. O. Rosenberg, B. J. Berne, and D. Chandler, *Isomerization dynamics in liquids by molecular dynamics,* Chem. Phys. Lett. **75**, 162 (1980).

[249] D. C. Knauss and G. T. Evans, *Liquid state torsional dynamics of butane: The Kramers rate and the torsion angle correlation times,* J. Chem. Phys. **73**, 3423 (1980).

[250] G. T. Evans, *Momentum space diffusion equations for chain molecules,* J. Chem. Phys. **72**, 3849 (1980).

[251] J. Zheng, K. Kwak, J. Xie, and M. D. Fayer, *Ultrafast Carbon-Carbon Single-Bond Rotational Isomerization in Room-Temperature Solution,* Science **313**, 1951 (2006).

[252] R. W. Pastor and M. Karplus, *Inertial effects in butane stochastic dynamics,* J. Chem. Phys. **91**, 211 (1989).

[253] D. M. Zuckerman and T. B. Woolf, *Transition events in butane simulations: Similarities across models,* J. Chem. Phys. **116**, 2586 (2002).

[254] Z. Guo and D. Thirumalai, *Kinetics of protein folding: Nucleation mechanism, time scales, and pathways,* Biopolymers **36**, 83 (1995).

[255] J.-P. Ryckaert, G. Ciccotti, and H. J. C. Berendsen, *Numerical integration of the cartesian equations of motion of a system with constraints: molecular dynamics of n-alkanes,* J. Comput. Phys. **23**, 327 (1977).

[256] G. Hummer, *From transition paths to transition states and rate coefficients,* J. Chem. Phys. **120**, 516 (2004).

[257] P. Metzner, C. Schütte, and E. Vanden-Eijnden, *On the calculation of reaction rate constants in the transition path ensemble,* J. Chem. Phys. **125**, 084110 (2006).

[258] E. Rhoades, M. Cohen, B. Schuler, and G. Haran, *Two-state folding observed in individual protein molecules,* J. Am. Chem. Soc. **126**, 14686 (2004).

[259] H. S. Chung, J. M. Louis, and W. A. Eaton, *Experimental determination of upper bound for transition path times in protein folding from single-molecule photon-by-photon trajectories,* Proc. Natl. Acad. Sci. **106**, 11837 (2009).

[260] H. S. Chung, K. McHale, J. M. Louis, and W. A. Eaton, *Single-molecule fluorescence experiments determine protein folding transition path times,* Science **335**, 981 (2012).

[261] H. S. Chung and W. A. Eaton, *Single-molecule fluorescence probes dynamics of barrier crossing,* Nature **502**, 685 (2013).

[262] T.-H. Lee, L. J. Lapidus, W. Zhao, K. J. Travers, D. Herschlag, and S. Chu, *Measuring the folding transition time of single RNA molecules,* Biophys. J. **92**, 3275 (2007).

[263] K. Truex, H. S. Chung, J. M. Louis, and W. A. Eaton, *Testing Landscape Theory for Biomolecular Processes with Single Molecule Fluorescence Spectroscopy,* Phys. Rev. Lett. **115**, 018101 (2015).

[264] H. S. Chung and I. V. Gopich, *Fast single-molecule FRET spectroscopy: theory and experiment,* Phys. Chem. Chem. Phys. **16**, 18644 (2014).

[265] K. Neupane, D. B. Ritchie, H. Yu, D. A. N. Foster, F. Wang, and M. T. Woodside, *Transition path times for nucleic acid folding determined from energy-landscape analysis of single-molecule trajectories,* Phys. Rev. Lett. **109**, 068102 (2012).

[266] H. Yu, A. N. Gupta, X. Liu, K. Neupane, A. M. Brigley, I. Sosova, and M. T. Woodside, *Energy landscape analysis of native folding of the prion protein yields the diffusion constant, transition path time, and rates,* Proc. Natl. Acad. Sci. **109**, 14452 (2012).

[267] J. M. Sancho, A. H. Romero, and K. Lindenberg, *The Kramers problem in the energy-diffusion limited regime,* J. Chem. Phys. **109**, 9888 (1998).

[268] D. L. Hasha, T. Eguchi, and J. Jonas, *High-pressure NMR study of dynamical effects on conformational isomerization of cyclohexane,* J. Am. Chem. Soc. **104**, 2290 (1982).

[269] J. Schroeder and J. Troe, *Elementary Reactions in the Gas-Liquid Transition Range,* Annu. Rev. Phys. Chem. **38**, 163 (1987).

[270] S. Chaudhury and D. E. Makarov, *A harmonic transition state approximation for the duration of reactive events in complex molecular rearrangements,* J. Chem. Phys. **133**, 034118 (2010).

[271] A. F. Voter and J. D. Doll, *Dynamical corrections to transition state theory for multistate systems: Surface self-diffusion in the rare-event regime,* J. Chem. Phys. **82**, 80 (1985).

[272] W. K. Kim and R. R. Netz, *The mean shape of transition and first-passage paths,* J. Chem. Phys. **143**, 224108 (2015).

[273] M. Evstigneev, O. Zvyagolskaya, S. Bleil, R. Eichhorn, C. Bechinger, and P. Reimann, *Diffusion of colloidal particles in a tilted periodic potential: Theory versus experiment,* Phys. Rev. E **77**, 041107 (2008).

[274] R. D. Hanes, C. Dalle-Ferrier, M. Schmiedeberg, M. C. Jenkins, and S. U. Egelhaaf, *Colloids in one dimensional random energy landscapes,* Soft Matter **8**, 2714 (2012).

[275] X.-g. Ma, P.-Y. Lai, B. J. Ackerson, and P. Tong, *Colloidal transport and diffusion over a tilted periodic potential: dynamics of individual particles,* Soft Matter **11**, 1182 (2015).

[276] C. Dellago, P. G. Bolhuis, F. S. Csajka, and D. Chandler, *Transition path sampling and the calculation of rate constants,* J. Chem. Phys. **108**, 1964 (1998).

[277] D. Marx, A. Chandra, and M. E. Tuckerman, *Aqueous Basic Solutions: Hydroxide Solvation, Structural Diffusion, and Comparison to the Hydrated Proton,* Chem. Rev. **110**, 2174 (2010).

[278] M. E. Tuckerman, D. Marx, and M. Parrinello, *The nature and transport mechanism of hydrated hydroxide ions in aqueous solution,* Nature **417**, 925 (2002).

[279] M. E. Tuckerman, A. Chandra, and D. Marx, *Structure and Dynamics of OH-(aq),* Acc. Chem. Res. **39**, 151 (2006).

[280] Z. Zhu and M. E. Tuckerman, *Ab Initio Molecular Dynamics Investigation of the Concentration Dependence of Charged Defect Transport in Basic Solutions via Calculation of the Infrared Spectrum,* J. Phys. Chem. B **106**, 8009 (2002).

[281] R. F. Grote and J. T. Hynes, *The stable states picture of chemical reactions. II. Rate constants for condensed and gas phase reaction models,* J. Chem. Phys. **73**, 2715 (1980).

[282] E. Pollak, H. Grabert, and P. Hänggi, *Theory of activated rate processes for arbitrary frequency dependent friction: Solution of the turnover problem,* J. Chem. Phys. **91**, 4073 (1989).

[283] R. Ianconescu and E. Pollak, *A study of Kramers' turnover theory in the presence of exponential memory friction,* J. Chem. Phys. **143**, 104104 (2015).

[284] G. Hummer, *Position-dependent diffusion coefficients and free energies from Bayesian analysis of equilibrium and replica molecular dynamics simulations,* New J. Phys. **7**, 34 (2005).

[285] T. B. Woolf and B. Roux, *Conformational Flexibility of o-Phosphorylcholine and o-Phosphorylethanolamine: A Molecular Dynamics Study of Solvation Effects,* J. Am. Chem. Soc. **116**, 5916 (1994).

[286] J. F. Ogilvie and F. Y. H. Wang, *Potential-energy functions of diatomic molecules of the noble gases I. Like nuclear species,* J. Mol. Struct. **273**, 277 (1992).

[287] J. F. Ogilvie and F. Y. H. Wang, *Potential-energy functions of diatomic molecules of the noble gases,* J. Mol. Struct. **291**, 313 (1993).

[288] C. P. Petersen and M. S. Gordon, *Solvation of Sodium Chloride: An Effective Fragment Study of $NaCl(H_2O)_n$,* J. Phys. Chem. A **103**, 4162 (1999).

[289] J.-B. Brubach, A. Mermet, A. Filabozzi, A. Gerschel, and P. Roy, *Signatures of the hydrogen bonding in the infrared bands of water,* J. Chem. Phys. **122**, 184509 (2005).

[290] D. Lin-Vien, N. B. Colthup, W. G. Fateley, and J. G. Grasselli, *The Handbook of Infrared and Raman Characteristic Frequencies of Organic Molecules* (Elsevier, San Diego, London, 1991).

[291] F. Marchesoni and P. Grigolini, *On the extension of the Kramers theory of chemical relaxation to the case of nonwhite noise,* J. Chem. Phys. **78**, 6287 (1983).

Abstract

Dynamic molecular processes in aqueous solutions are essential for biological life, and their fundamental timescale is determined by molecular friction. In this thesis, several basic dynamic phenomena relevant for aqueous biological systems are studied by a combination of molecular dynamics simulations and stochastic models.

First, we show by ab initio molecular dynamics simulations that the polarization of continuum bands in infrared spectra of small protonated water clusters allows us to deduce their shape and orientation. The molecular origin of continuum bands of protonated water wires is elucidated. Based on these results and recently recorded, experimental polarization-resolved infrared spectra, we reveal the orientation of a protonated water cluster in the transmembrane protein bacteriorhodopsin.

Secondly, the friction of an externally confined, water-solvated methane molecule is extracted from molecular dynamics simulations using a newly developed method to parametrize a generalized Langevin equation. We show that the friction increases by up to 60% with increasing confinement strength, which is accompanied by a slowing down of the translational and rotational water dynamics in the hydration shell. This previously unknown effect is relevant for the interpretation of spectroscopy experiments as well as for trapped particles in viscous solvents.

Thirdly, the mass dependence of the methane friction in water is studied by a similar method. We demonstrate that the friction increases with solute mass by up to 70%, which goes along with a slowing down of the hydration shell dynamics by a factor of three. We characterize the scaling behavior of mass-dependent friction and show that the often applied power-law relation holds only for an intermediate regime.

Next, we compute the friction memory kernel of the dihedral angle of water-solvated butane by another newly developed method for the parametrization of generalized Langevin equations in the presence of arbitrary, non-linear potentials. This method is applied to a free butane molecule as well as to a constrained butane with the dihedral angle as the only positional degree of freedom, in both cases for different solvent viscosities. The results allow us to answer a long-lasting question by showing that dihedral angle isomerization reactions are dominated by internal friction.

Finally, we show that the ensemble properties of so-called transition paths, which connect an initial starting position without return to a target state, deviate significantly from equilibrium. The deviation can be quantified by an effective temperature, which reaches several times the ambient temperature for systems with low friction.

All of these results constitute significant advancements to the respective subfields, and together they shed light on the complex and subtle interplay of friction, inertial and non-Markovian effects on the molecular scale.

Kurzfassung

Dynamische molekulare Prozesse in wässrigen Lösungen sind essenziell für jede Form biologischen Lebens, und ihre fundamentale Zeitskala ist durch die molekulare Reibung definiert. In der vorliegenden Arbeit werden grundlegende dynamische Phänomene, die für wässrige biologische Systeme relevant sind, mit einer Kombination aus Molekulardynamik-Simulationen und stochastischen Modellen untersucht.
Zuerst zeigen wir mithilfe von Ab-initio-Simulationen, dass die Polarisation von Kontinuumsbanden in Infrarotspektren kleiner protonierter Wassercluster Rückschlüsse auf deren Form und Orientierung zulässt. Außerdem wird die molekulare Ursache von Kontinuumsbanden protonierter Wasserketten aufgedeckt. Als Anwendung wird aus experimentellen, polarisationsaufgelösten Infrarotspektren die Orientierung eines protonierten Wasserclusters im Transmembranprotein Bacteriorhodopsin bestimmt.
Im zweiten Teil der Arbeit extrahieren wir die molekulare Reibung eines künstlich festgehaltenen, in Wasser gelösten Methanmoleküls aus Molekulardynamik-Simulationen mittels einer neu entwickelten Methode zur Parametrisierung generalisierter Langevin-Gleichungen. Die Reibung nimmt mit der Stärke des externen Potentials um bis zu 60% zu, was mit einer Verlangsamung der Hydrationsdynamik einhergeht. Dieser bisher unbekannte Effekt ist sowohl für die Interpretation spektroskopischer Experimente relevant als auch für festgehaltene Teilchen in viskosen Lösungsmitteln.
Des Weiteren wird die Massenabhängigkeit der Reibung von Methan in Wasser mit ähnlichen Methoden analysiert. Im Vergleich zu leichten Soluten ist die Reibung schwerer Solute um bis zu 70% höher und die Hydrationsdynamik ist verlangsamt. Insbesondere wird das Skalenverhalten der massenabhängigen Reibung vollständig charakterisiert.
Im vierten Teil der Arbeit untersuchen wir den Torsionswinkel eines in Wasser gelösten Butanmoleküls mithilfe einer weiteren neu entwickelten Methode zur Parametrisierung generalisierter Langevin-Gleichungen in beliebigen Potentialen. Wir betrachten freies Butan und ein eingeschränktes Butanmolekül mit dem Torsionswinkel als einzigem Freiheitsgrad jeweils bei verschiedenen Viskositäten, um zu zeigen, dass die Isomerisationsreaktion von Torsionswinkeln durch interne Reibung dominiert wird.
Zum Schluss zeigen wir, dass die statistischen Eigenschaften sogenannter Übergangspfade, die eine Anfangsposition ohne Wiederkehr mit einer Zielposition verbinden, signifikant vom Gleichgewicht abweichen. Die Abweichung kann durch eine effektive Temperatur beschrieben werden, die für Systeme mit geringer Reibung ein Vielfaches der Umgebungstemperatur erreicht.
Diese Ergebnisse sind wesentliche Fortschritte in den jeweiligen Spezialgebieten, und in der Summe tragen sie zum Verständnis des komplexen Zusammenspiels zwischen Reibung, inertialen und nicht-Markovschen Effekten auf der molekularen Skala bei.

Erklärung

Hiermit erkläre ich, dass ich die vorliegende Dissertationsschrift mit dem Titel

Molecular Friction and Dynamics in Aqueous Solutions

selbstständig angefertigt und hierfür keine anderen als die angegebenen Hilfsmittel verwendet habe. Die Arbeit ist weder in einem früheren Promotionsverfahren angenommen noch als ungenügend beurteilt worden.

Berlin, den 24. Januar 2018

Danksagung

Ich möchte mich herzlich bei meinem Doktorvater Prof. Dr. Roland Netz für die erstklassige Betreuung und die zahlreichen interessanten Diskussionen bedanken, und dafür, dass er diese Arbeit ermöglicht hat. Für die Zweitbegutachtung dieser Arbeit möchte ich mich bei Prof. Dr. Holger Stark bedanken.
Des Weiteren bin ich meinen Koautoren und Kollegen für ihre Hilfe und Anregungen sehr dankbar, insbesondere Bartosz Kowalik, Mattia Saita, Julian Kappler, Prof. Dr. Joachim Heberle und Prof. Dr. Matthias Heyden, sowie Florian Brünig, Dr. Won Kyu Kim, Dr. Alexander Schlaich, Dr. Douwe Bonthuis, Richard Schwarzl, Philip Loche, Dr. Julius Schulz, Dr. Yann von Hansen und auch Dr. Markus Miettinen. Außerdem bedanke ich mich bei allen aktuellen und ehemaligen Mitgliedern der AG Netz und bei Annette Schumann-Welde für ihre Unterstützung und für die angenehme Arbeitsatmosphäre. Besonderer Dank gilt zudem unserem IT-Administrator Jens Dreger für sein Engagement bei der Bereitstellung der nötigen Ressourcen für die aufwändigen Rechnungen dieser Arbeit.
Bei meinen Freunden und besonders bei meiner Freundin Tini möchte ich mich herzlich für viele schöne Stunden, gutes Zureden und viel Verständnis bedanken.
Zum Schluss möchte ich mich ganz herzlich bei meinen Eltern und bei meiner Schwester bedanken, ohne deren wunderbare Unterstützung während meines gesamten Lebens diese Arbeit sicher nicht zustande gekommen wäre.